FACIES AND POROSITY DISTRIBUTION BY THE INTEGRATION OF ROCKPHYSICS ANALYSIS AND SEISMIC INVERSION IN SILICICLASTIC RESERVOIRS

A Thesis

by

DIEGO GABRIEL PALACIOS SERRANO

Submitted to the Office of Graduate and Professional Studies of
Texas A&M University
in partial fulfillment of the requirements for the degree of

MASTER OF SCIENCE

Chair of Committee,	Yuefeng Sun
Committee Members,	Zoya Heidari
	Juan Carlos Laya
Head of Department,	Rick Giardino

December 2014

Major Subject: Geophysics

ABSTRACT

Seismic inversion approach has been applied with a moderate success in some siliciclastic reservoirs in Oriente Basin characterized by their prominent lateral facies variations. Different types of facies with different geological and petrophysical characteristics can produce similar response in seismic velocities. Based on this fact, inversion results such as P-Impedance, S-Impedance, Vp/Vs., Poisson ratio and other derived elastic parameters can be misinterpreted leading to locating faked prolific zones in areas where facies do not have enough quality to be considered productive.

In order to achieve this objective, rock physics analysis is used to tie the seismic inversion results to the geological and petrophysical rock characteristics. The Sun model has proven to characterize successfully the seismic response of carbonate and siliciclastics rocks and infer geological, depositional, diagenetical and petro physical characteristics from sonic logs and seismic data. Using the compressional frame flexibility factor *(γ_k)* and the shear frame flexibility factor *(γ_u)* derived from this model, it is possible in this thesis to successfully correlate geological, depositional and diagenetical characteristics to the seismic response using well log and core data from two siliciclastic reservoirs in Oriente Basin. γ_k and γ_s factors characterize the pore structure influence to the variability of the compressibility and shear sonic velocities respectively in rocks. For these siliciclastic reservoirs, which present a prominent lateral variation in facies related to their depositional process, different ranges of γ_k factor values represent different kind of facies. Values of γ_k between 2 and 6 in "U" sandstone

reservoir and values of γ_k higher than 6 in "Hollin" sandstone reservoir are closely correlated to the best quality facies. According to the integrated rock physical, petrophysical and geological analysis in well locations, clean massive sandstones with fine to medium grain size and moderately sorting are represented by this γ_k value interval.

Using simultaneous inversion results and the assumption previously mentioned, volumes of porosity and γ_k are inverted from seismic data. Spatial distribution of the γ_k values in the inverted volume correlates well with a previous sedimentological interpretation study using core data descriptions. Finally, using porosity and values of γ_k, the discrimination of the best quality facies is performed. As a final result, new prospective zones are visualized taking into account the structural characteristics and facies distribution obtained by this integrated analysis.

DEDICATION

I dedicate this thesis to my Mother and Father whose effort has always been an inspiration in my life.

ACKNOWLEDGEMENTS

I would like to thank my committee chair, Dr. Yuefeng Sun whose guidance has been very valuable not only for the accomplishment of this research but also to improve my critical analysis in many technical aspects. I would also like to thank Dr. Zoya Heidari and Dr. Juan Carlos Laya for their support, as well.

I make a special recognition to Alejandra Mendoza whose support and trust were very important during the time that my studies lasted.

Thanks also go to my friends and colleagues and the department faculty and staff for making my time at Texas A&M University a great experience.

I also want to extend my gratitude to PETROAMAZONAS EP, which authorized the release of the data used in this research. An especial gratification to Manuel Rivera, Gustavo Cosios, Santiago Leon, Dimitri Flores who were always willing to help with my endeavors taking time out of their schedule.

Finally, I have an enormous gratitude to SENESCYT for financially supporting my education.

NOMENCLATURE

K	Effective bulk modulus
K_{dry}	Bulk modulus of dry rock (Gassmann, 1951)
K_0	Bulk modulus of the rock-forming minerals (Gassmann, 1951)
K_{sat}	Bulk modulus of fluid saturated rock (Gassmann, 1951)
K_f	Bulk modulus of pore-filling fluid
K_s	Bulk modulus of rock-forming minerals
α	Pore aspect ratio
ρ	Bulk density
ρ_s	Density of solid
ρ_f	Fluid density
ϕ	Total porosity
γ_k	Frame flexibility factor – related to bulk modulus
γ_μ	Frame flexibility factor – related to shear modulus
μ	Effective shear modulus
μ_{dry}	Shear modulus of dry rock (Gassmann, 1951)
μ_s	Shear modulus of the rock forming minerals
V_p	Compressional velocity
$Vs.$	Shear velocity
c	Ratio of γ_μ / γ_k
C	Constant of relationship between α and γ_k

Vcl	Content of clay
LNSH	Lower Napo Shale Top
MNSH	Main Napo Shale Top
λ	Lambda coefficient
σ	Poisson ratio
Ip	P-Impedance
Is	S-Impedance

TABLE OF CONTENTS

Page

Page

LIST OF FIGURES

Page

Page

Page

Page

Page

Page

LIST OF TABLES

Page

1.INTRODUCTION

The discontinuity of prolific facies and the rapid change of the petrophysical characteristics make it difficult to obtain optimum results from common seismic inversion approach. Different facies can produce the same seismic response in the target reservoirs for this research. Impedance and elastic parameter values enclose much information that not only comes from the influence of lithology per se and petro physical properties, but also come from other structural characteristics of the rock like pore structure and grain contact. Pore structure has a great influence on sonic wave velocities and on the quality of the rock, which can define its production feasibility. Rock physics analysis helps geologist to understand the causes of the seismic response of the reservoirs and permits them to obtain petro physical parameters from elastic parameters and vice versa. Different rock physics models have been created and applied to clastic reservoirs. According to Avseth et al., 2013, all models can be classified into three main groups: theoretical, empirical and heuristic. The most common theoretical model is the Biot-Gassmann model based on the work from Biot, 1956 and Gassmann, 1951. Other authors have established a relation between the elastic properties of rocks and their petrophysical properties; especially, the relationship between impedance or P-sonic velocity and porosity, Raymer, et al., 1980; Wyllie and Gregory, 1956. A simple linear relationship between these two parameters can be established in exceptional conditions that do not exist in the target reservoirs for this study.

Xu et al., 1995 established that the presence of clay in the sandstone produces scattering in the relationship between P-sonic velocities and porosities. They also stated that the clays form pores with smaller aspect ratios than those of sandstone pores. According to them, the essential feature of the model is the assumption that the geometry of pores associated with sand grains are significantly different from that associated with clays. Because of this, porosity in shales affects the elastic compliance differently from the porosity of sandstone. A unique dependence of the P-sonic velocity on porosity has been discussed by many authors who argue that porosity is only another characteristic that defines seismic wave propagation in rocks.

Sun, 2004 states that the behavior of seismic waves is derived from the pore structure, porosity, mineralogy, fluid content, pressure and temperature. Sun, 2000 established that the physical properties of complex porous medium is determined by knowing the intrinsic properties of the solid grains and pore fluid, the parameters characterizing the structural effects, and the coupling coefficients between the solid grains and between the solid matrix and fluids. In order to improve the porosity estimation from elastic parameters and to characterize the effect of pore structure on seismic waves, the Sun's model will be implemented. In 2000, Sun introduced a parameter called frame flexibility factor that characterized the effect of pore structure, grain contacts, grain coupling, cementation, and pore connectivity on the flexibility and elasticity of porous rocks. According to Sun, 2004, the higher the flexibility factor is, the fewer the grain contacts and grain coupling. In many, but not in all cases, this could mean that the higher the frame flexibility factor is, the higher the pore connectivity.

Since this factor is related to the pore structure, it could be expected also that some relationship between shale content and frame flexibility factor exists as shown in Adesokan et al., 2010.

Constrained sparse-spike inversion methodology will be used for this research. Constrained sparse-spike inversion is not a model-based inversion; it is a recursive trace–by-trace inversion that considers that the strongest reflections correspond to the largest impedance contrast and gets rid of short reflections. This inversion considers the criteria of sparseness. According to Oldenburg, 1983, after the deconvolution of the seismic trace, the results will have the same frequency band as the original seismic data. In other words, the inversion loses the low- and high-frequency content. In order to add the low frequency content, an impedance model derived from interpolation of well logs will be created and then band-passed to the limits of the low-frequency gap of the seismic data. This low-frequency model must be merged during the inversion as a trend constraint. From the simultaneous inversion, volumes of acoustic impedance, shear impedance, density, poisson ratio, lambda-rho and mu-rho will be obtained. From these parameters, bulk modulus and shear modulus must be obtained. Based on the results of the rock physics analysis and the correlation found by the frame flexibility factor and pore structure – rock quality, the inversion of frame flexibility factor and the porosity volumes from elastic parameters based on the Sun' s approach will be performed.

Objectives of the study

The main objective from this research is to transport the results related to classification and qualification of the facies that will be obtained using rock physics analysis based on core data, thin slides, well logs and other geological information to the seismic data frequency range and its three-dimensional coverage. This is very important since it will reduce the geological uncertainty between well information. This fact will allow optimization of the economic and logistical resources and the development strategy for the reservoir.

Since the rapid variation of facies within the studied reservoirs is linked to their fluvial-tidal depositional conditions, it is necessary to define the areal extension and connectivity of the most prolific sand bodies.

The expected results include

1. Three-dimensional distribution of porosity and facies through the link between the results from rock physics analysis and seismic inversion using an integration of petrophysical geological, geophysical data in two stratigraphic reservoirs in Oriente Basin
2. The areal definition of the reservoir facies will allow delineating the optimum locations for new prospective zones.

Background

Data collection and analysis

Three-dimensional (3D) seismic data will be used in this study. A post-stack volume and four partial stacks as angle gathers will be used for simultaneous inversion. The angle interval of the angle gather stacks are 4-14°, 12-22°, 20-30° and 28-40°. All volumes present the following characteristics: average maximum frequency is 50Hz; the average minimum frequency is 8 Hz; and the bin is equal to 30 m x 30 m. According to the processing report, no AGC (Amplitude Gain Compensation) were performed, and the most recommended steps for the seismic processing sequence directed to keep seismic data characteristic used in the inversion were applied.

P-sonic, S-sonic and density logs are the fundamental logs to be used in the seismic inversion and in the rock physics analysis. From a total of 60 wells, only four have an S-sonic log curves, and 34 have P-sonic log curves. All 60 wells have density, gamma-ray and resistivity logs. Unfortunately, only 2 wells have caliper log. Only one VS.P is part of the set of data. Data from two cores are available. One of them has values of porosity, permeability and water saturation and the other one has porosity values only. Both of them have sedimentological descriptions.

Many non-published geological reports were provided by PETROAMAZONAS EP such as mineralogical analysis, thin sections and mud logging reports.

Tectonism of the Oriente Basin

The Oriente Basin is a foreland basin located at the backarc of the Andes Mountains. The structural framework that defined the basin is complex and has changed during the time due to many tectonic events. This is one of the most prolific basins in South America (Figure1).

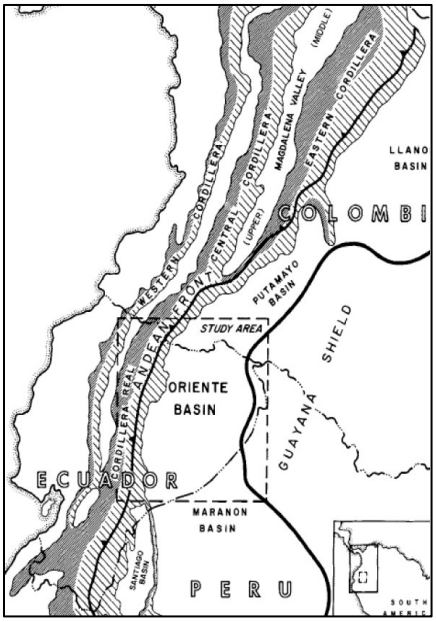

Figure 1. Location map of the Oriente Basin. (Dashwood and Abbotts ,1990)

There is no detailed description about the tectonism and paleogeography of the ages prior to the Triassic age due to lack of data. During the Late Triassic, a relaxing tectonism is recorded. As Baby, et al.,2004 states, the sedimentation of the Sacha-Shushufindi (Figure 2) corridor was controlled by high dip angle normal faults that affect the basement and shows a rift from the Triassic through the Late Jurassic periods.

This is related with the Tethyan aperture that influenced the Northern Andes evolution. (Jaillard., 1997).

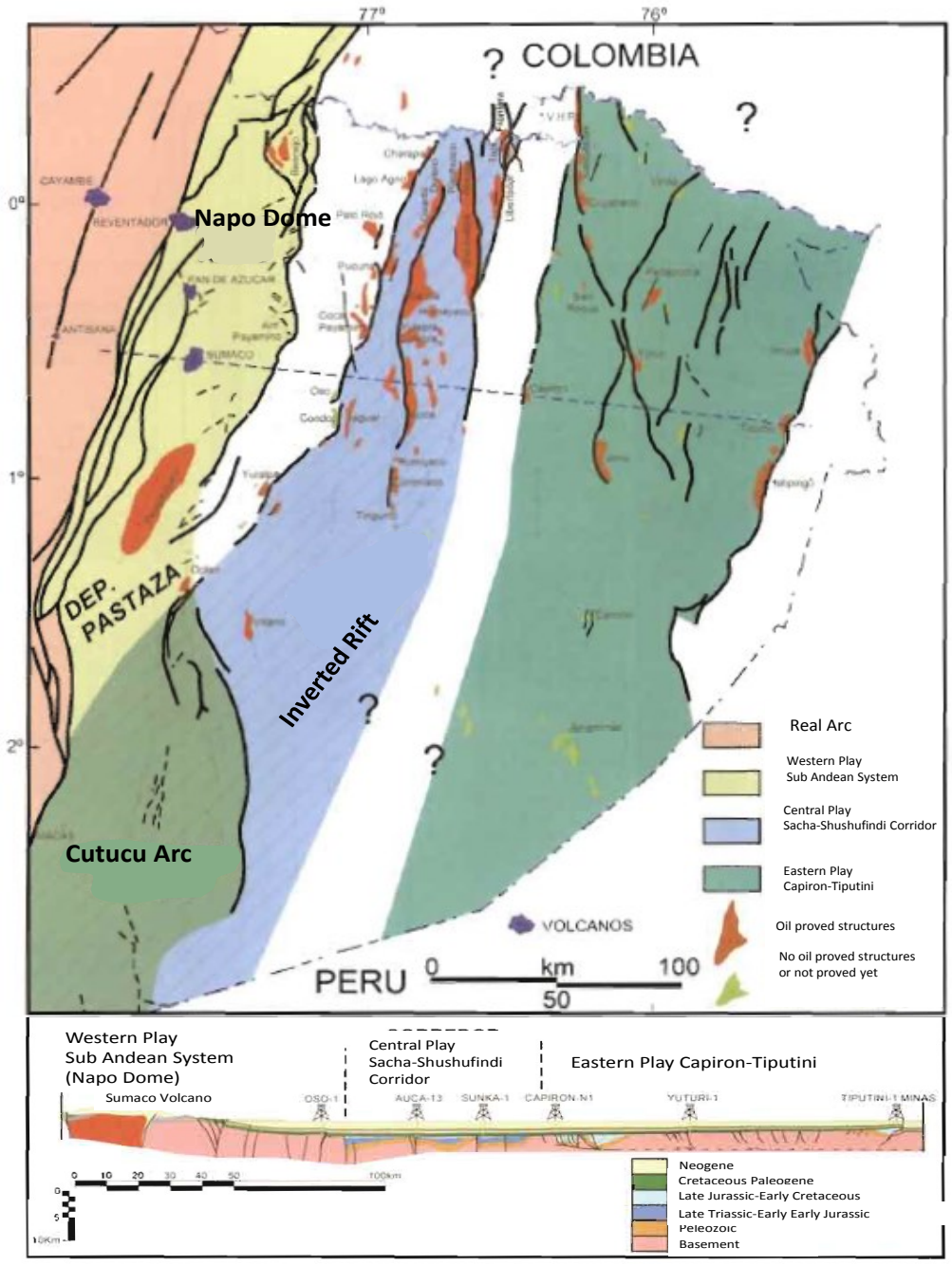

Figure 2. Tectonic map of Oriente Basin. (Modified from Baby, et al.,2004)

The deposition of Santiago Formation occurred in the Early Jurassic. (Figure 3). This formation presents a continental volcanism that proves the rift aperture. (Romeuf el al., 1997). During this period, the subduction process with south east direction originated a potent volcanic arc with NNE-SSW trend that is present from the north of Peru to the north of Colombia (Romeuf el al., 1995). In Ecuador, this is the Misahualli Formation (Figure 3).

With this event the Rift aperture finished and an erosional surface on the base of the Chapiza Formation occurred (Christophoul, F., 1999). (Figure 3). Chapiza Formation presents a continental depositional environment but at the east the presence of these continental sediments is not evident From the Kimmeridgian-Titonian, the subduction direction changed to the northwest. (Jaillard, 1997). Subduction process could produce transpressive dextral tectonic events that could be related with first inversion of the Sacha-Shushufindi faults and could create echelon anticlines. During this period Chapiza Formation had its strongest development.

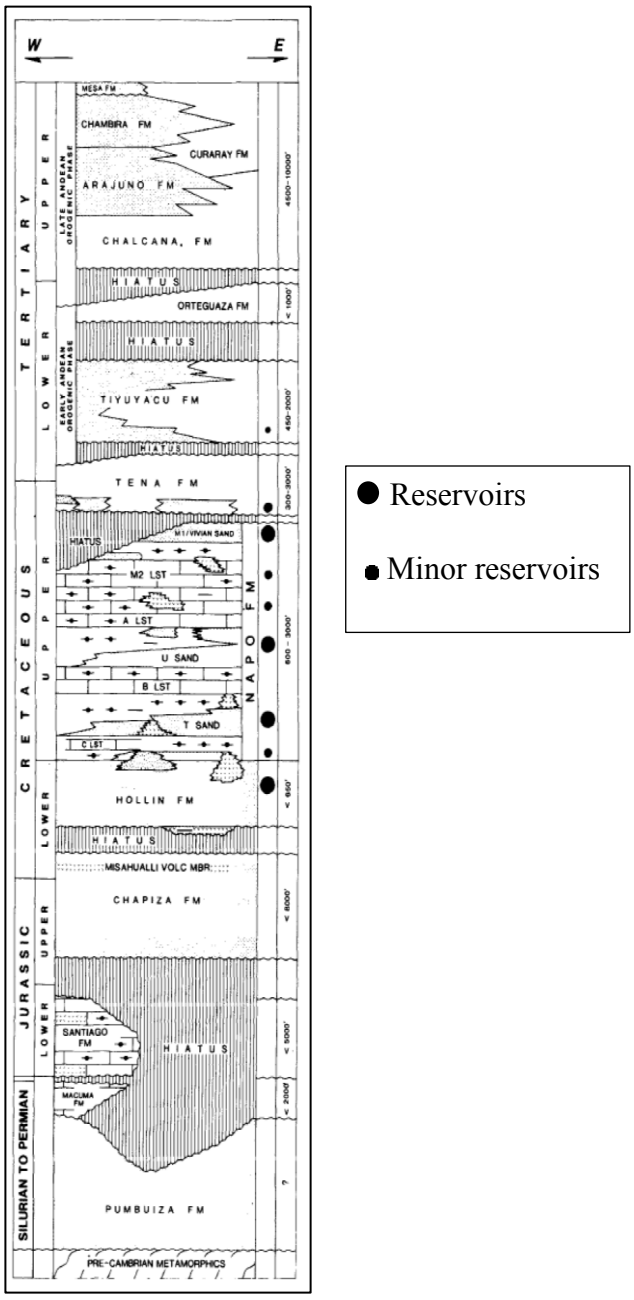

Figure 3. Stratigraphic column of the Oriente Basin (Dashwood and Abbots, 1990)

A schematic summary of the of the geodynamic evolution from the Late Triassic to the Early Cretaceous of Oriente Basin is presented in Figure 4

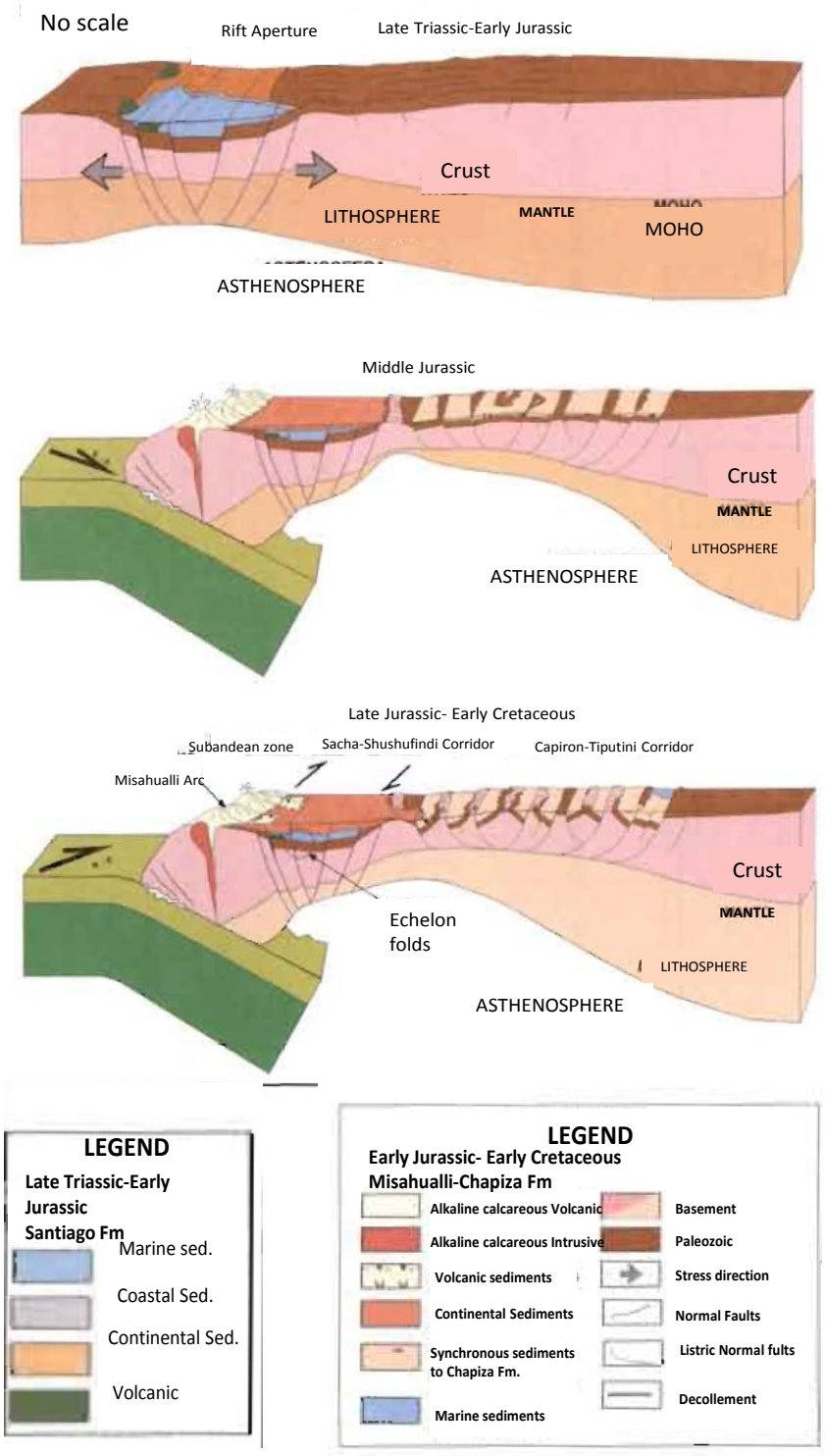

Figure 4. Schematic summary of the of the geodynamic evolution from the Late Triassic to the Early Cretaceous of Oriente Basin . (Modified from Baby, et al., 2004)

Subduction of the Nazca Plate behind the South American plate produced the formation of the Andes Mountains in the time between Paleocene and Oligocene. (Dashwotts, et al. 1990). This tectonism caused a series of transpressives events that inverted the previous normal faults created in the Triassic and Early Jurassic rifting. As a result, this compressional episode produced a series of high dip reverse faults oriented N-S and NNE-SSW. The current reverse faults limit three structural petroliferous corridors; the Sacha- Shuhsufindi corridor (Central Play), the Sub Andean system (Western Corridor) and the Capiron -Tiputini corridor (Eastern play) as shown in Figure 2.

The Oriente Basin is characterized by geological features that have contributed to the limitation in the areal extension of many formations deposited in earlier time than Maastrichtian when a common erosional surface affected the whole basin. The Napo Uplift, Cutucu Arc, and Pastaza depression are the most prominent features that affected the Oriente Basin and they were created in the Neogene, (Figure 2).

The Sacha-Shushufindi corridor encloses the most prolific oilfields in the Oriente Basin. Most of these oilfields are delimitated by thrust faults in anticlines with an axis trend NE-SW. In the Subandean zone, oilfields have medium to heavy oil while in Sacha Shushufindi corridor medium gravity oil is prominent in most of the oilfields. The stratigraphic column of the Oriente Basin is shown in Figure 3. The main prolific conventional Cretaceous reservoirs in the Oriente Basin from the oldest to the youngest are Hollin, Napo T, Napo U, Basal Tena, and M1 formations.

Sequence stratigraphy of the Cretaceous in Oriente Basin

A brief sequence stratigraphic description of the Cretaceous units based on the study of Barragan, R .et al., 2004 is presented below. The coast line of the shallow marine shelf in Cretaceous had many positions due to relative sea level changes. This fact had contributed to areal and vertical variations in the facies.

It is possible to define sequence boundaries, and subsequences for the Cretaceous formations. A mega sequence that encloses Hollin-Napo- Basal Tena can be defined. This mega sequence and parasequences defined by the change in the eustatic level that occurred at the Cretaceous time have continuous groups of sands, limestone and shale. (Xu et al.,1995). The mega sequence is divided in five cycles as is shown in Figure 5. Cycle I began with a deposition of fluvial sands that are erosive and channelized (Main Hollin). Base formations of the Cycle II and III were deposited in estuarine environment with tidal influence (Upper hollin, Main U and Main T). The source of sediments has been localized at the south east of the Basin coming from the Guyanes Shield.

Then, sedimentation of shallow marine facies indicates transgressions to the east of the Basin. These events are characterized by the presences of shaly tidal sands (Upper U, Upper T and Upper Hollin). Finally the maximum level of flooding is characterized by marine platform limestone and shallow dense shales (Napo Basal Shale, Midle Napo shale o U shale, A limestone, Upper and Napo Upper shales). The final part is characterized by platform sediments represented by dense limestone with detritic influence. (Barragan, R .et al., 2004)

The Cycle I is defined by the fluvial main Hollin sand, the Upper Hollin sand, the C limestone, the Napo Basal shale and the T limestone. Napo Basal shale marks the end of the cycle that last from Late Aptian to Late Albian. T limestone is restricted at the west boundary of the Basin only. Cycle II lasts from Late Albian to the Middle Cenomanian, and it comprises the Napo T sand that is divided in Upper and Main T sand, the Middle Napo shale or U limestone at the western part of the Basin, Figure 5. Cycle III which lasted from the Late Cenomian to the Late-Middle Turonian is defined by the Main U sandstone, Upper U sandstone and A limestone. The maximum level of flooding is represented by the A limestone that is almost continuous along the Basin.

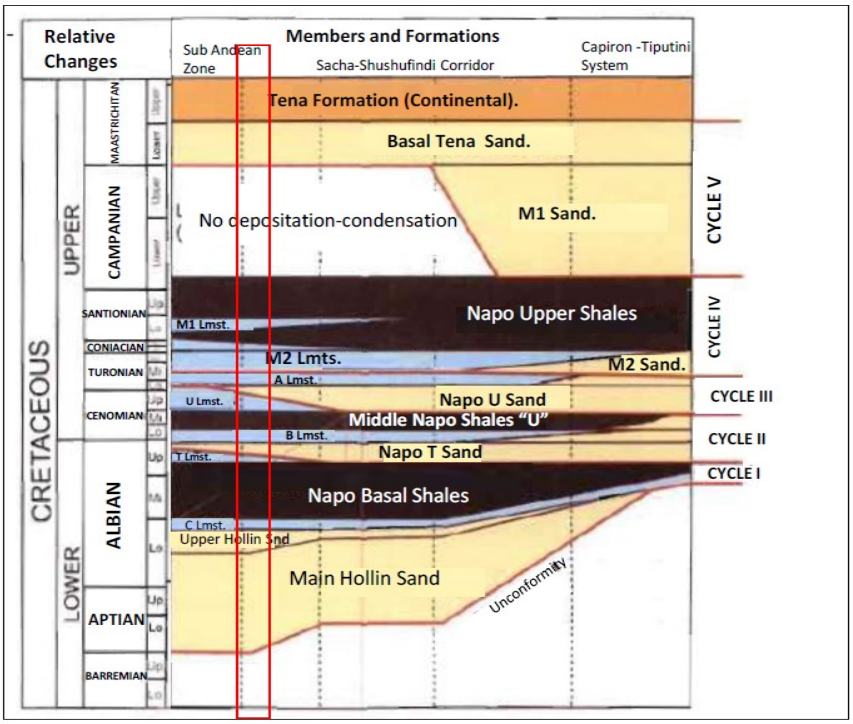

Figure 5. Stratigraphic column of Cretaceous in Oriente Basin (Barragan, R .et al., 2004)

Cycle IV goes from Turonian to Early Campanian and includes the M2 sand at the east of the Basin and the M2 limestone at the west of the Basin; as it is shown in the Figure. 5. Also, M1 Limestone and the M1 Shale o Napo Upper Shale are part of this sequence. At the west and central part of the Basin, the sequence presents marine properties where there is no influence of siliciclastic input. The depositional environment of this sequence at the west area is a marine carbonate platform. The M2 sand is limited at the east part of the basin and onlap over the A limestone, (Barragan, R .et al., 2004). The M2 sandstone is a fluvial-estuarine sand deposited during a sea level fall restricted to the west part of the basin. This cycle shows a difference from the other ones since the sequence is condensed at the west part of the basin. The units for this research are highlighted in Figure 5 with the red rectangle where the M2 and M1 sand has been condensed completely. The condensation of the sequence began from the Sacha-Shushufindi corridor to the Subandean Zone. Figure 5 shows that the thicknesses of the formations in the Cycle IV are comprised at the west part of the basin, so the most prolific oilfields for M2 sandstone are at the east of the Basin, far from the Subandean zone.

Cycle V is formed by the interval between M1 sandstone and Basal Tena sandstone from the Campanian to the Early Maastrichtian and the complete cycle is restricted at the east part of the basin. The M1 sandstone is limited at the east part of the basin, and it was deposited in incised fluvial valleys at the center of the basin during a eustatic level fall. (Barragan, R .et al., 2004). The Basal Tena sandstone is deposited over the M1 sandstone at the east part and over the Napo Upper shales at the west area

of the Basin. The depositional environment has been defined as a prograding delta. (Barragan, R .et al.,2004). Basal Tena formation was deposited only in the subsiding zones of the basin and it is the edge of the marine depositional environment that changes to a sub areal environment as the result of Andes Uplift. Finally, it constituted the foreland basin.

The Cycles IV and V are constrained by a compressive tectonism and the inversion of previous extensive structures. The tectonism restricted the extension of the formations from the Touronian to the Maastrichtian creating stratigraphic discontinued surfaces. Also, as evidence of geodynamic changes in the Basin, the presence of volcanism with intrusive and extrusive bodies affects this section in a structural, stratigraphic and geochemical way. The condensation of the Cycle IV and a part of the Cycle V are attributed by Baby, et al., 2004 to a consequence of the compressional tectonics that produced a lifting that reduced the sedimentation. On the other hand, Dashwotts et al., 1990 considers that the unconformity over the Napo Upper Shales is a product of the uplift and erosion of the basin. These events removed completely the upper section of the Napo in the west part of the basin before the Basal Tena deposition. Also, a regional unconformity was created from the Campanian to Maastrichtian.

The productive reservoirs of the area of study are the Main Hollin and some limited extended areas of the Upper Hollin sandstone. Also, the Main U sandstone and some areal zones of the Upper U sandstone are the second target for oil production. As it was stated before, the depositional environment of Main Hollin was a fluvial environment, specifically formed by massive braided rivers. The depositional

environment of Main U, Main T and some zones of Upper Hollin are characterized by bars influenced by tides. According to Vallejo et al., 2013, the upper part of the Upper Hollin is deposited by shoreface sand bars with variable percentages of glauconite and with an East –West orientation. In the same way the Upper U and Upper T are deposited in a shoreface zone. The sedimentological characteristics of Main U, Upper Hollin and Upper U make them present a discontinuity in reservoir facies that affects the profitability of the oil exploitation. The outcome for this research is to use seismic data to map the different facies using rock physics analysis through the link of geology to seismic data.

The nature of the sand bars makes them difficult to map or predict due to their areal extension being restricted to some specific zones as it is shown in Figure 6. Influence of tides, waves and marine currents affect the spatial distribution of the facies in the Hollin sandstone and U sandstone that are the target reservoirs for this study.

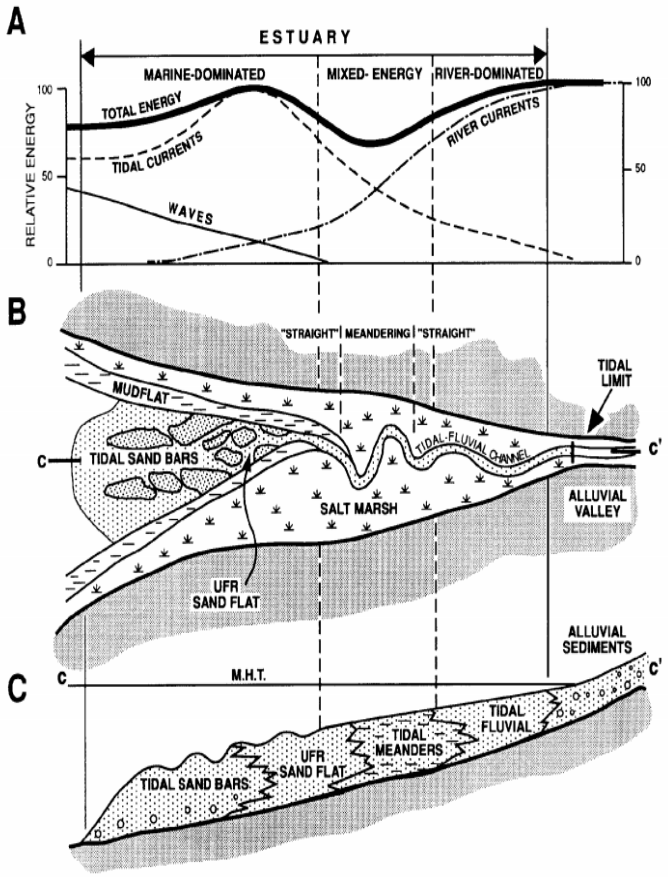

Figure 6. Distribution of A) energy types, B) morphological dements in plain view, and C) sedimentary fades in longitudinal section within an idealized tide-dominated estuary. URF = upper flow regime; M.H.T. = mean high tide. The section in C is taken along the axis of the channel and does not show the marginal mudflat and salt marsh facies; it illustrates the onset of progradation following transgression, the full extent of which is not shown. (Dalrymple et al., 1992).

2. METHODS

Rock physics model

In the recent years more interest has been set to improve the relationship between seismic velocities and the critical characteristic that define the reservoir rocks quality. Parameter such as porosity, lithofacies, pore fluid, pore pressure, saturation have a higher impact in the reservoir quality. In order to reduce the geological uncertainty in an oilfield, transformation from seismic signatures to these parameters is widely use in the industry. In facies in which the sedimentation and digenesis have affected some parameters like mineralogy or pore structure, a simplified stiff conversion from P-velocity or impedance to porosity is not suitable since the scatter presented in the correlation. Application of empirical relations such as Willie et al., 1956, Raymer et al., 1980, and others produce a strong inaccuracy in the porosity derived values. Rock physics analysis using well log data, core data, mineralogical analysis and all the geological data that can serve as a tool to characterize the reservoirs is essential to link seismic data to petro physical properties in a successful way. A simple relation between porosity and seismic velocities is not common due to presence of clay, variations of pore shape, and different fluid types in the reservoirs.

Many rock physics models have been created in order to represent the seismic velocity behavior taking into account many of the factors mentioned before. Voight, 1910 and Reuss, 1929 established a very simple weighted relation to determine the elastic modulus in a mixture of materials based on the volume fraction of its

constituents. Voigt, 1910 and Reuss, 1929 equations are described below in equations 1 and 2 respectively.

$$Mv = \sum_{i=1}^{N} f_i M_i \quad (1)$$

$$\frac{1}{\mathrm{Mr}} = \sum_{\mathrm{i=1}}^{\mathrm{N}} \frac{\mathrm{f_i}}{\mathrm{M_i}} \quad (2)$$

with

f_i as the volume fraction of the *i*th constituent and the M_i as the elastic modulus of the *i*th constituent.

The Voigt and Reuss's approaches can represent any elastic modulus such as bulk modulus, shear modulus μ, Young's modulus *E*, etc. (Avseth et al., 2013).

These expressions could be considered as the upper and lower bounds of the elastic modulus in a rock that is formed by different kind of materials. Figure 7 shows a schematic representation of these bounds in a porosity- velocity relation.

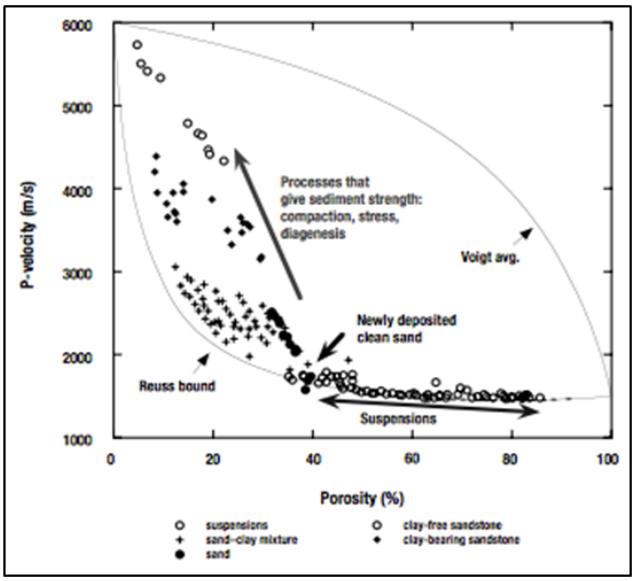

Figure 7. Results of multiple experimental studies indicate patterns of lithology in the compressional velocity-porosity relationship. (Mavko et al., 2003)

This figure shows that the Voigt, 1910 and and Reuss, 1929 can be taken as the limits for a series of rock samples that presents different compaction, diagenesis, water fraction, and clay fraction. The Voigt bound is sometimes called the iso-strain average because it gives the ratio of the average stress to the average strain when all constituents are assumed to have the same strain. (Mavko et al., 2003). The Reuss average describes exactly the effective moduli of a suspension of solid grains in a fluid. (Avseth et al., 2013) and also it is sometimes called the iso-stress average because it gives the ratio of the average stress to the average strain when all constituents are assumed to have the same stress. (Mavko et al., 2003). There are other approaches to calculate the elastic modulus of a mixture of mineral components; one of the most widely use is the Hashin et al., 1963's approach. It considers an isotropic elastic mixture in which the geometric

arrangement of constituents is not taken into account. However, these bounds only give an approximation of the range of elastic modulus values. Gassmann, 1951' model has been widely used to understand the influence of pore fluids in the seismic response. The change of pore fluids will affect the rock bulk density and the rock compressibility which is the reciprocal of the bulk modulus. According to Gassmann, 1951, seismic response is affected by the porosity and by the stiffness of the pore space as well as pore fluid. Besides, a softer rock will have higher seismic sensitivity to the change in fluids than a stiffer rock of the same porosity. This is called the fluid substitution problem. Gassmann, 1951and Biot, 1956, states that the bulk modulus of saturated rock will be higher than the bulk modulus of a dry rock. The following is the most familiar equation for fluid substitution analysis:

$$\frac{\boldsymbol{K_{sat}}}{\boldsymbol{K_s - K_{sat}}} = \frac{\boldsymbol{K_{dry}}}{\boldsymbol{K_s - K_{dry}}} + \frac{\boldsymbol{K_f}}{\phi(\boldsymbol{K_s - K_f})} \quad (3)$$

$$\boldsymbol{\mu_{sat} = \mu_{dry}} \quad (4)$$

Where K_{dry} is the effective bulk modulus of dry rock, K_{sat} saturated bulk modulus, K_0 mineral material bulk modulus, K_{f} is the fluid bulk modulus, ϕ is the porosity, μ_{dry} shear modulus of the dry rock and μ_{sat} is the shear modulus saturated rock.

Gassman's equation does not take into account any assumption about pore geometry; it assumes a homogenous mineral modulus, and statistical isotropy of the pore space and it is only valid for low frequencies. Gassman's equations work well for

frequencies less than 100 Hz. Also, this equation can be used to predict the bulk modulus change when some fluid replaces another as shown in equation 5:

$$\frac{K_{sat1}}{K_s - K_{sat\,1}} + \frac{K_{f\,1}}{\phi(K_s - K_{sat\,1})} = \frac{K_{sat2}}{K_s - K_{sat\,2}} + \frac{K_{f\,2}}{\phi(K_s - K_{sat\,2})} \quad (5)$$

Gassmann's theory does not take into account the effect of the pore structure and this produces a limited success in obtaining an accurate velocity-porosity relationship. In order to improve the correlation of the rock properties and seismic velocities, incorporation of factors such as pore shape is needed.

Sun's Model

Pore shape and structure and its connectivity strongly influence the elastic modulus and seismic velocities in rocks. Based on this fact, Sun, 1994 introduced a topological characterization of the structural media that provides a representation of the internal structure of a fractured porous medium at a finer scale and investigated the general mechanics and thermodynamics of fractured porous media. This theory was intended to provide a unified theoretical model for the full porosity range of materials from low-porosity igneous rocks to highly unconsolidated sediments. (Sun, 2000). In the case of sedimentary rocks or high porosity sediments, velocity changes are caused by the interaction of grains (mechanical grain coupling) and the coupling between the pore fluid and grains. (Geertsma and Smit, 1961; Sun, 1994; Sun and Goldberg, 1997). Sandy sediments and mud hemiplegic sediments gain in stiffness with depth. As depth

increases the space between grains is reduced and the coefficient of sliding friction is increased. Furthermore, the analysis of grain coupling effects can allow obtaining better results in the estimation of rock properties from conventional well log data and seismic data.

In the target reservoirs for this study one of the most important factors to delineate the quality of the reservoir is the clay volume. Clay presence in reservoirs affects the pore structure and the mechanical grain coupling in sandstones. Sun's model has been used in successful ways to characterize carbonate reservoirs and has been applied to improve the estimation of porosity, (Sun et al., 2002; Massaferro et al., 2004). A simplified version of Sun's model is presented below (Sun, 2000)

$$V_p = \sqrt{\frac{K+\frac{4}{3}\mu}{\rho}} \tag{6}$$

$$V_s = \sqrt{\frac{\mu}{\rho}} \tag{7}$$

where

$$\rho = (1-\phi)\rho_s + \phi\rho_f \tag{8}$$

$$K = (1-\phi_k)K_s + \phi_k K_f \tag{9}$$

$$\phi_k = F_k\phi \tag{10}$$

$$F_k = \frac{1-(1-\phi)^{\gamma_k}}{\left[1-(1-\phi)^{\gamma^k}\right]\frac{K_f}{K_s}+\left(1-\frac{K_f}{K_s}\right)\phi} \tag{11}$$

$$\mu = \mu_s(1-\phi)^{\gamma_\mu} \tag{12}$$

$$c = \frac{\gamma_\mu}{\gamma_k} \tag{13}$$

where

V_p = compressional wave velocity

Vs. = shear wave velocity

ρ_s = solid matrix density

K_s=solid matrix bulk modulus

μ_s= solid matrix shear modulus

ρ_f = fluid density

K_f = fluid bulk modulus

ϕ =porosity

γ_k, γ_μ = frame flexibility factors.

c= gamma ratio

As Sun, 2000 mentions, the equations 6 to 13 define the compressional and shear wave velocities in terms of intrinsic solid and fluid properties and geometrical factors which are valid in principle for the entire porosity range from pure solid (ϕ=0) to pure fluid (ϕ=1). However, since there are some simplifications caution should be taken when the studied rocks present characteristics that have been simplified in the development of the equations; for instance, effects of solid suspensions in pore fluids and isolated fluid inclusion in solids. (Sun, 2000). The γ_k and γ_μ are the coupling coefficients and are named frame flexibility factors. Generally the higher γ_k, the less the grain contacts and grain coupling; in many cases this could mean that the higher γ_k is, higher pore connectivity. However, to establish an accurate relationship, diagenetic history of the reservoir must be taken into account and a feasibility analysis using well logs must be

performed. Inverting γ_k and γ_u factors from well logs and comparing with petrophysical - geological analysis and production data give good relationships between γ_k and γ_μ and reservoir quality, facies and some petrophysical properties. Sun, 2004 states that *c* ratio is a physical parameter that quantifies the ease of the rock frame to undergo shear motion relative to its compressibility. For two different rock frames that have the same frame compressibility they may have different resistance to shear motion owing their different pore shapes. (Sun, 2004).

Adesokan et al., 2010 establishes a correlation between the γ_k and the aspect ratio α as it is shown in equation 14

$$\alpha = C\left(\frac{1}{\gamma}\right) \tag{14}$$

where aspect ratio is defined as the ratio of the minimum to the maximum axis of pore and it defines the pore shape. *C* is a constant which has upper bound of 1 for pure clay and 0.5 for pure quartz. (Adesokan et al., 2010). Figure 8 shows different pore shapes and their aspect ratio values

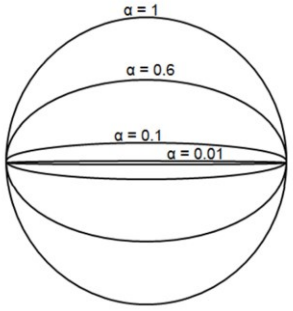

Figure 8. Cross-sections of elliptical pores of different aspect ratios from Minear, 1982.

Xu, et al., 1995 states that clay particles as well as microfractures create pores with very small aspect ratios. Hence, the value of γ_k is closely determined by the pore shape and by other factors that were explained before.

Using conventional well log data, the γ_k and γ_μ will be inverted applying Sun's model. Then, a series of cross plots that correlates the elastic parameters, petro physical properties and flexibility factors can be performed, supported with the knowledge obtained from geological data such as thin sections, core analysis and descriptions. These cross plots will determine the sensitivity of the geological data to elastic parameters obtained from well logs and rock physics analysis.

Simultaneous inversion

The outcomes obtained from rock physics analysis need to be migrated to the seismic data coverage. To perform the second part of this research, commercial inversion software from CGG-Jason Company was used. The software used the Constrained Sparse Spike Inversion (CSSI) methodology. The CSSI is a methodology that assumes that reflection coefficients are sparse. It means that seismic data can be modeled only with a few large reflections coefficients over imposed to random background of the small events that represent the noise as shown in Figure 9.

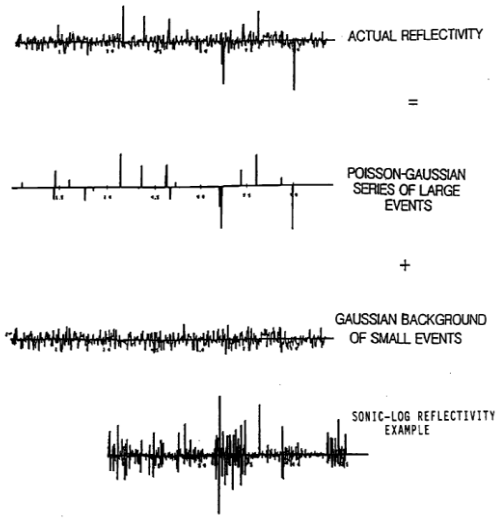

Figure 9. The fundamental assumption of the Sparse Spike Inversion (Russel, 1988).

The convolutional model uses a predefined wavelet that comes from the well seismic-tie. The inversion algorithm sets a group of reflection coefficients that are convolved with the predefined wavelet and they are changed in each iteration until the objective function is minimized. A set of constraints are added to the objective function. Lateral variations in the low frequencies are incorporated via the use of a model that comes from the well log interpolation. Low frequencies are missed since the wavelet obtained in the well tie correlation must coincide with frequency range of seismic data. Therefore, the results from CSSI misses the low frequency range and the missed frequency must be added using a low cut filtered model from the well log interpolation. Applying soft spatial constraints improves the signal-to-noise ratios of the inversion results. In the case of the post stack acoustic impedance inversion the objective function is expressed as:

$$(Ip) = F_{Contrast} + F_{Seismic} + F_{Trend} + F_{spatial} \quad (15)$$

where

$F_{contrast}$ is used to keep a sparse solution

$F_{seismic}$ is used to match the seismic

F_{trend} and F spatial are used to constrain the solution to geology

Each constraint is evaluated trace by trace over the time gate and each of them depends on the others. This means that when one constraint becomes smaller the others become bigger. The contrast misfit constraint controls the change in vertical direction of P impedance normalized to low pass frequency trend that comes from the well log interpolation model. The seismic misfit corresponds to S/N ratio and the correlation between synthetics and real seismic data. The trend constraint is influenced by merge cutoff frequency which is a user defined frequency value at which the addition of the low band pass information is performed. The spatial misfit constraints the change of the P-impedance in the direction relative to low pass filtered trend.

For the Simultaneous Inversion that is a CSSI inversion, different angle gather stacks will be used. For each angle gather stack, one wavelet was estimated through well- seismic-tie. The reflection coefficients are calculated by the Zoeppritz, 1919 or Aki and Richards, 1980 approximation. P-impedance, S-impedance and density volumes are the results of the inversion; therefore, in order to fill their low frequency gap in the results a well log interpolation model for P-impedance, S-impedance and density volumes must be created and then filtered to the low frequency values needed to merged

with the frequency interval of the seismic data. The objective function of the simultaneous inversion is:

$$(Ip) = F_{Contrast} + F_{Seismic} + F_{Trend} + F_{spatial} + F_{Gardner} + F_{Mudrock} + F_{SVD} \quad (16)$$

where the first four terms have been already described above but in this case the P impedance, S impedance and density vertical misfit is used. Also the synthetic –seismic correlation for each angle gather stack is used. Besides, the trend and spatial constraints are applicable for the three elastic parameters obtained from the inversion

$F_{Gardner}$ function constraints the density based on the change of P-impedance.

$F_{Mudrock}$ function constraints the S-impedance based on the change of P-impedance.

F_{SVD} function is used to stabilize the inversion applying a constraint to the S-impedance and the density increasing small eigenvalues. It uses a defined threshold for the eigenvalues. Eigenvalues bigger than the threshold causes the weight impose to this misfit function to be zero. So, when the eigenvalues are smaller that the threshold the weight of the misfit function works. This can replace the Gardner and Mudrock functions.

The inversion results allows obtaining many elastic parameters such as P sonic velocity, S sonic velocity, Poisson ratio, Lamda-rho (λ-ρ), Mu-rho (μ-ρ) and also bulk modulus (K), shear modulus (μ). Bulk modulus, shear modulus and density will be used to invert the porosity and frame flexibility factor from the rock physics analysis using Sun's model.

3. ROCK PHYSICS MODEL FOR U AND HOLLIN RESERVOIR

Hollin sandstone

It is divided in two main units. The lower one was deposited in a fluvial environment and presents better petrophysical characteristic than the upper unit. The upper unit named Upper Hollin was deposited in shoreface zone in a shallow marine platform and also some tidal bars in other areas. (Vallejo et al., 2013) According to unpublished mud logging reports of wells C-21, C-20,C-31, C-30, C33, C-27, C-32 and C-24 property of Petroamazonas EP, most of the lower sandstone named Main Hollin is described with fine to medium grain size, sub rounded to rounded grain shape, and no visible cement except in specific zones. Kaolinite matrix is also present in restricted zones. Near the contact with Upper Hollin, the characteristics of the Main Hollin moderately change, grain size become finer upwards and in some wells some kaolinite intercalations appeared. Besides, it has a very sharp water oil contact (WOC) and the success of production of this sandstone is determined by the location of the WOC in new prospective zones. As it is massive sandstone with good petro physical characteristics and with an active aquifer, the main strategy to produce is to avoid setting the perforated intervals near the WOC. This strategy is due to the threat provoked by conning since gravity forces are bigger than viscous forces. As the oil gravity is around 32 º API, it is expected that the difference in pore fluid could cause some velocity response difference.

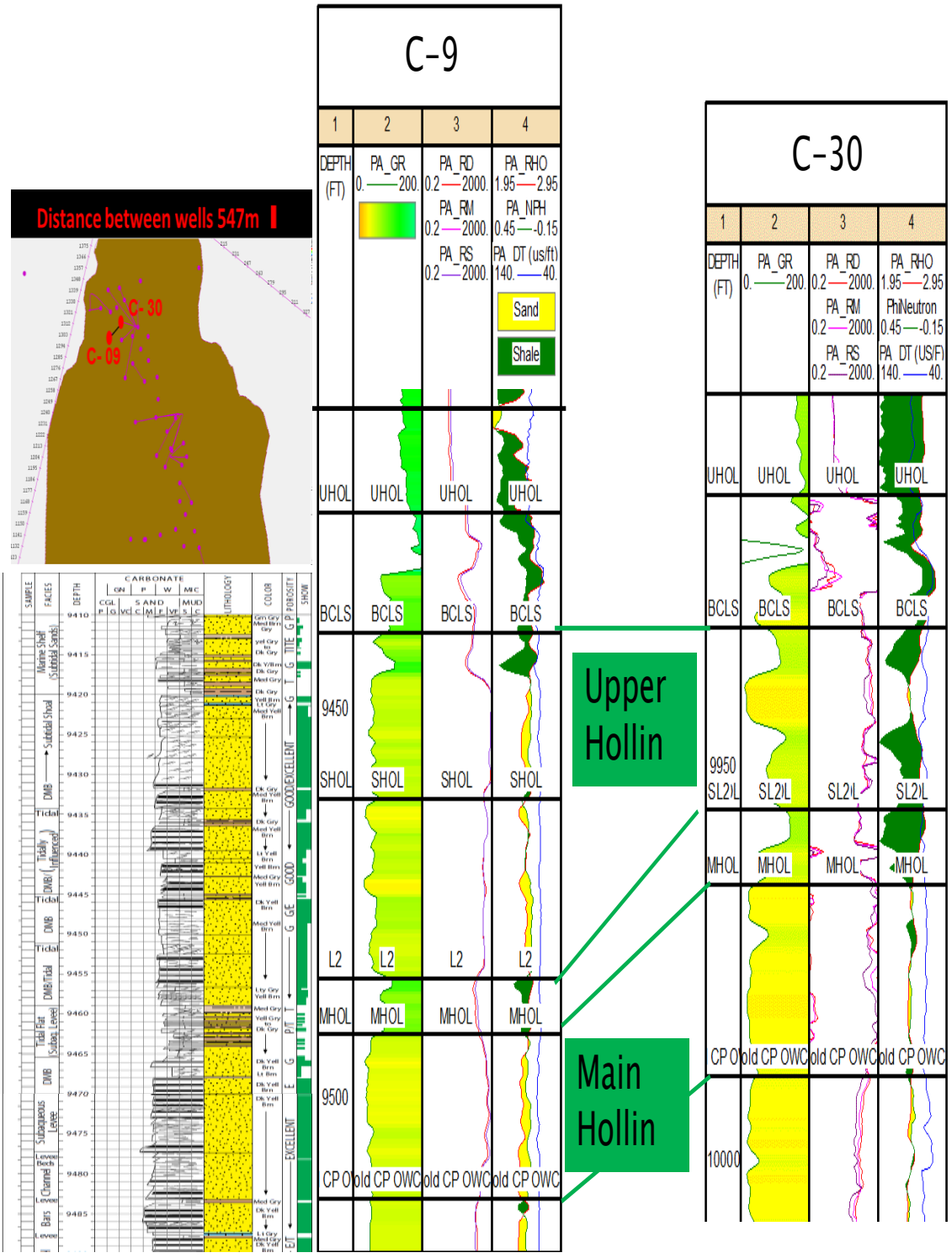

Figure 10. Well tie of C-9 and C-30 wells and core description of C-9 well

However, since the upper part of the Main Hollin presents kaolinite intercalations and calcareous cement, this fact could affect the seismic response and mask the pore fluid substitution effect. Figure 10, shows a well correlation of C-9 and C-30 wells, also a core description image of the C-9 (White, 1993) is attached

Upper Hollin sandstone characteristics are different from Main Hollin sandstone ones. Upper Hollin presents more glauconite inclusions, pyrite incision and some carbonate drapes. As stated before, Upper Hollin reservoirs were deposited in shore face zone in shallow platform so the influence of tides and storms are evident. This sandstone was deposited in restricted zones where the quality of the rock allows being a prolific reservoir. The areal extension of this reservoir unit in Upper Hollin is restricted to zones that according to Vallejo et al. 2013 were deposited as tidal bars. These bars have elongated shapes parallel to the tidal currents. As we can see in Figure 10, in C-9 well, Upper Hollin presents as a good quality reservoir. Gamma ray is low, neutron and density logs show a crossover and the resistivity is high. On the other hand, the Upper Hollin segment in C-30 well indicates poor petro physical characteristics; most of the segment is influenced by shale and in the upper part carbonate sandstone are common. The distance between these two wells is around 547 m. Main Hollin and Upper Hollin are divided by a shale that seems to be constant along the whole area.

Mineralogical composition of Hollin sandstone

Mineralogical composition was extracted from unpublished reports from Petroamazonas EP (Alvarado et al., 1989) and they were correlated with the cuttings

description and some microscopic images. For the Main Hollin sandstone, 93% is quartz the remaining 7% is formed of potassium feldspar, muscovite, pyrite, kaolinite, tiny fragments of igneous rocks and zircon. Pyrite is present sometimes in 1%. The igneous rocks are present in less than 1%. Silica matrix is present in the majority of the interval; however, some parts show slightly carbonate cementation. Most of the non-quartz fraction is feldspar and kaolinite. Figure 11 shows microscopic images of the well C-4 for Main Hollin sandstone. Average pore throat size for Main Hollin is about 20 to 30 µm.

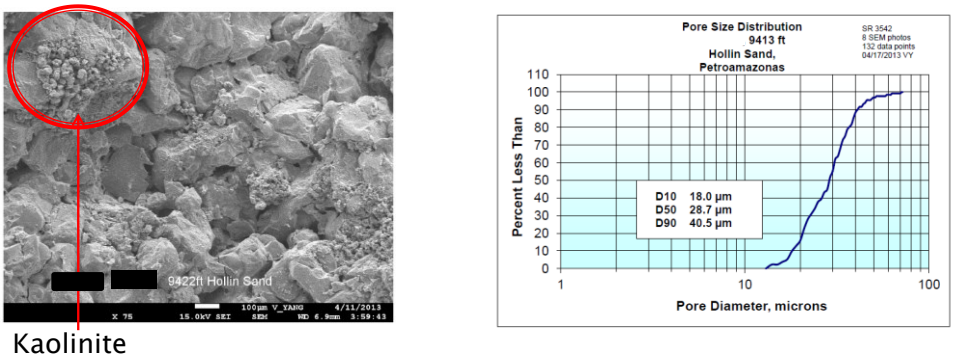

Figure 11. Microscopic images and pore throat size distribution from well C- 4 in Main Hollin. (Halliburton, 2013)

The mineralogical composition for Upper Hollin is very variable and in some specific parts of the field good quality sandstones appear. The rest of the facies are compounded by shale and carbonate sandstones. For pay zones the average mineralogical composition is formed by quartz grains with glauconite and some kaolinite, pyrite inclusions, and some carbonate laminations. In sandstones intervals in

Upper Hollin, quartz is present in a percentage 76-85%, glauconite as an structural grain is around 2-5%, kaolinite is around 7-15%, pyrite with 1-3% and in some areas calcite cement is 1-4%. Upper Hollin presents a very fine to fine grain size, with few laminations of clay, not only dispersed clay. It has slighly carbonated cement in some zones. (Jones, M., 1993)

Petro physical interpretation of Hollin sandstone

Conventional petrophysical analysis was performed for the Hollin and U sandstones. First of all, well log normalization was checked for all logs based on the consistency in log measurements of the Lower Napo Shale, Middle Napo Shale and A Limestone that are constant in the whole basin. Figure 12 shows a P-sonic histogram values results of well logs for Lower Napo Shale, Middle Napo Shale and A limestone

After checking the normalization for all the available wells, a few shift were performed for Well P-10, P-3, C-31 and P-13 in P- sonic and density curves. To make correcion the U reservoir, the Middle Napo Shale and A Limestone were used. To normalize Hollin sandstone, the Lower Napo Shale was used.

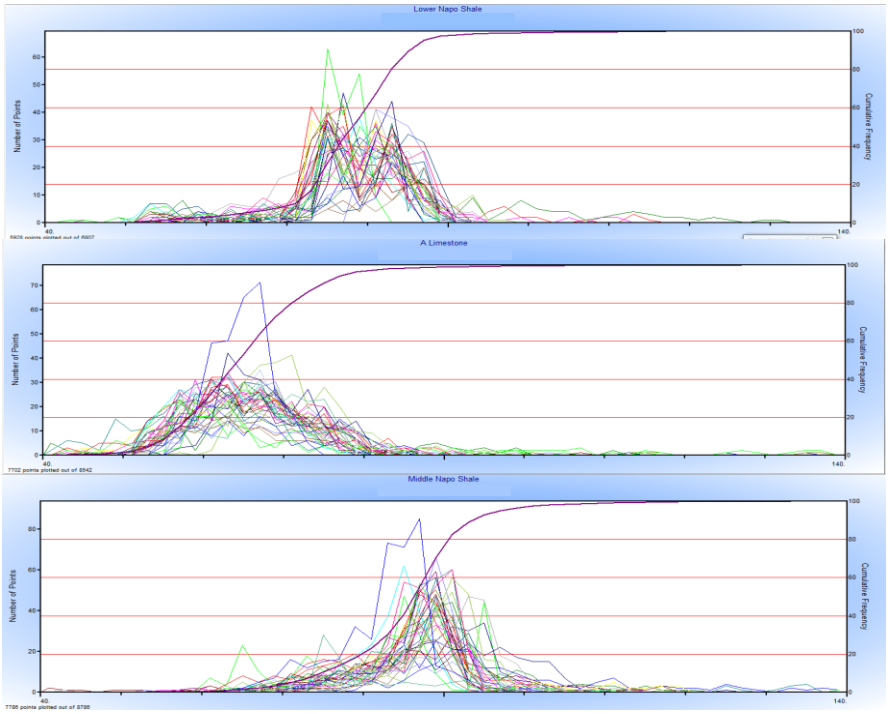

Figure 12. Well log normalization results. P-Sonic curves

In order to establish the best approach to calculate the Volume of clay (Vcl) a consideration must be done; according to mineralogical analysis of Main Hollin, presence of potassium feldspar is in low concentrations around 7% and it could raise the Volume of clay calculation from gamma ray (Vcl_{Gr}). Potassium in the feldspar could affect the gamma ray values in spite of the low concentration of K-feldspar present in these rocks. But, it is not possible to determine the level of influence in gamma ray values since no spectral gamma ray log is available. Therefore, neutron and density must also be used to calculate the volume of clay ($Vcl_{N\text{-}D}$) in order to compare with the Vcl_{Gr}. On the other hand, most of the wells do not have caliper curve so it is not possible to determine what the well condition was at the moment of the logging run. Also, gamma ray is less affected than density and neutron tool due to washouts and mud cake. Since

Vcl_{Gr} presents lower values than $Vcl_{N\text{-}D}$ values, it can de suggested to take this value as the most accurate volume of clay; however, the unquantified influence of k-feldspar in gamma ray do not allow to do this. Equation 17 and 18 are the formulas used to calculate Vcl_{Gr} and $Vcl_{N\text{-}D}$ respectively, and equation 19 is their average value.

$$Vcl_{Gr=} \frac{Gr-Gr_{min}}{Gr_{max}-Gr_{min}} \quad (17)$$

$$Vcl_{N-D} = \frac{\phi_N-\phi_D}{\phi_{N,sh}-\phi_{D,sh}} \quad (18)$$

$$Vcl = \frac{Vcl_{Gr}+Vcl_{N-D}}{2} \quad (19)$$

$$\phi_D = \frac{\rho_b-\rho_m}{\rho_f-\rho_m} \quad (20)$$

where

Gr is the direct tool measurement

Gr_{min} is the measurement value in clean sand

Gr_{max} is the measurement value in pure shale

ϕ_N is the direct neutron tool measurement (Neutron in sandstone matrix)

ϕ_D is the porosity from density tool corrected by matrix (sandstone= 2.65 g/cm^3)

$\phi_{N,sh}$ is the direct neutron tool measurement in pure shale zone

$\phi_{D,sh}$ is the porosity from density tool corrected by sandstone matrix (2.65 g/cm^3) in pure shale zone

ρ_b is the direct tool measurement

ρ_m is the matrix density 2.65 g/cm^3

ρ_f is the density of the fluid. Since the reservoir produces a 26.4 º API, the density of fluid is assumed to be 1 g/ $cm^{3.}$

Accuracy of the three calculations methods for the volume of clay will be tested using each of them in the determination of porosity and the latter comparison with core porosity values. The porosity calculation was done assuming that kaolinite is around the quartz grains; it means that presence of clay is represented by a dispersed clay model as shown in figures 11 and 13.total porosity is calculated using the following equations;

Figure 13. Schematic representation of the dispersed clay model

$$\phi_D^{sh} = \phi_D - Vcl\phi_{D,sh} \quad (21)$$

$$\phi_N^{sh} = \phi_N - Vcl\phi_{N,sh} \quad (22)$$

$$\phi_s = \frac{\phi_D^{sh} + \phi_N^{sh}}{2} \quad (23)$$

$$\phi_t = \phi_s + Vcl\phi_{sh} \quad (24)$$

where ϕ_D^{sh} and ϕ_N^{sh} are the non-shale porosity from density and neutron tool. ϕ_s is the average non-shale porosity, and ϕ_t is the total porosity. Total porosity can be defined as the sum of non-shale porosity and clay bound water. ϕ_{sh} is the porosity of shale calculated with the equation

$$\phi_{sh} = \frac{\rho_b - \rho_m}{\rho_f - \rho_m} \quad (25)$$

where:

ρ_b is the direct tool measurement in pure shale zone

ρ_m is the matrix density is the density of kaolinite-glauconite average in g/cm^3

ρ_f is the density of the fluid. (assumed 1 g/ cm^3)

In order to validate the results from petrophysical interpretation, a comparison with data from a conventional core analysis of Hollin sandstone from well C-9 is performed. From core analysis experiences, it is inferred that most of the reservoir rocks have a few isolated pores. Hence, there is very little or no measurable difference between effective and total porosity. So, the porosity from core analysis can be compared with the total porosity of well logs, (American Petroleum Institute, 1988). Figure 14 is the representation of the different porosities defined for core analysis and well log analysis.

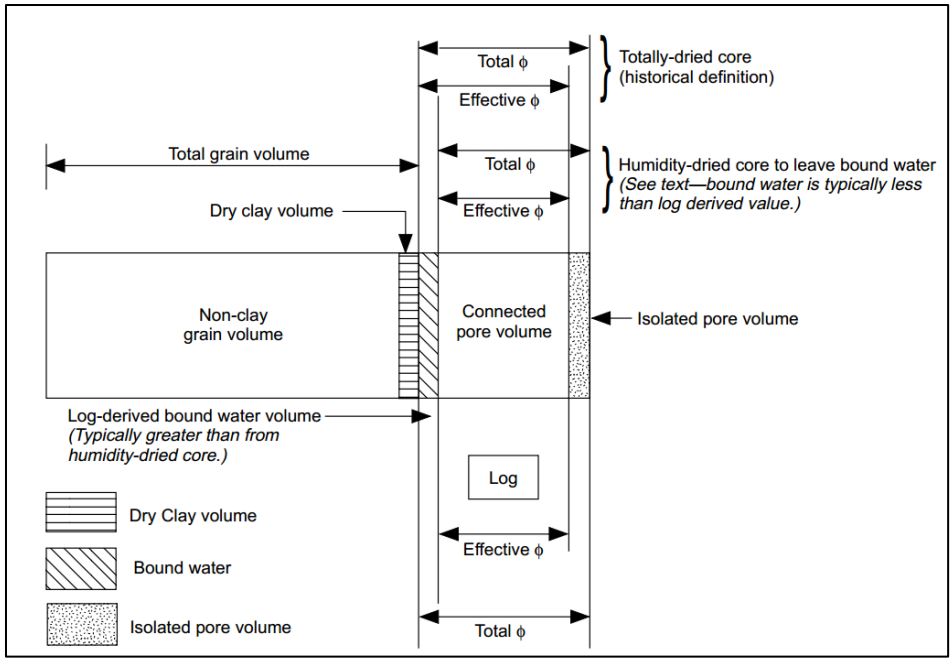

Figure 14. Total and effective pore volumes as defined by core and log analysts (American Petroleum Institute, 1998)

The correlation coefficient between the core porosity and Φ_t from well logs presents the highest value using the equations 21 to 25 with Vcl (obtained by the average of Vcl_{Gr} and $Vcl_{N\text{-}D}$ values). The correlation coefficient of the comparison between Φ_t and core porosity exceeds in 5 and 6 points in percentage to the correlation coefficient from the comparison between core porosity and Φ_t calculated using Vcl_{Gr} and $Vcl_{N\text{-}D}$ separately.

Also, in order to test if the Φ_t calculation approach is accurate; the comparison of density porosity vs. core porosity and neutron density corrected by Vcl with core porosity is performed.

Figure 15 shows the correlation for log–core porosity values for the Upper Hollin and Main Hollin,

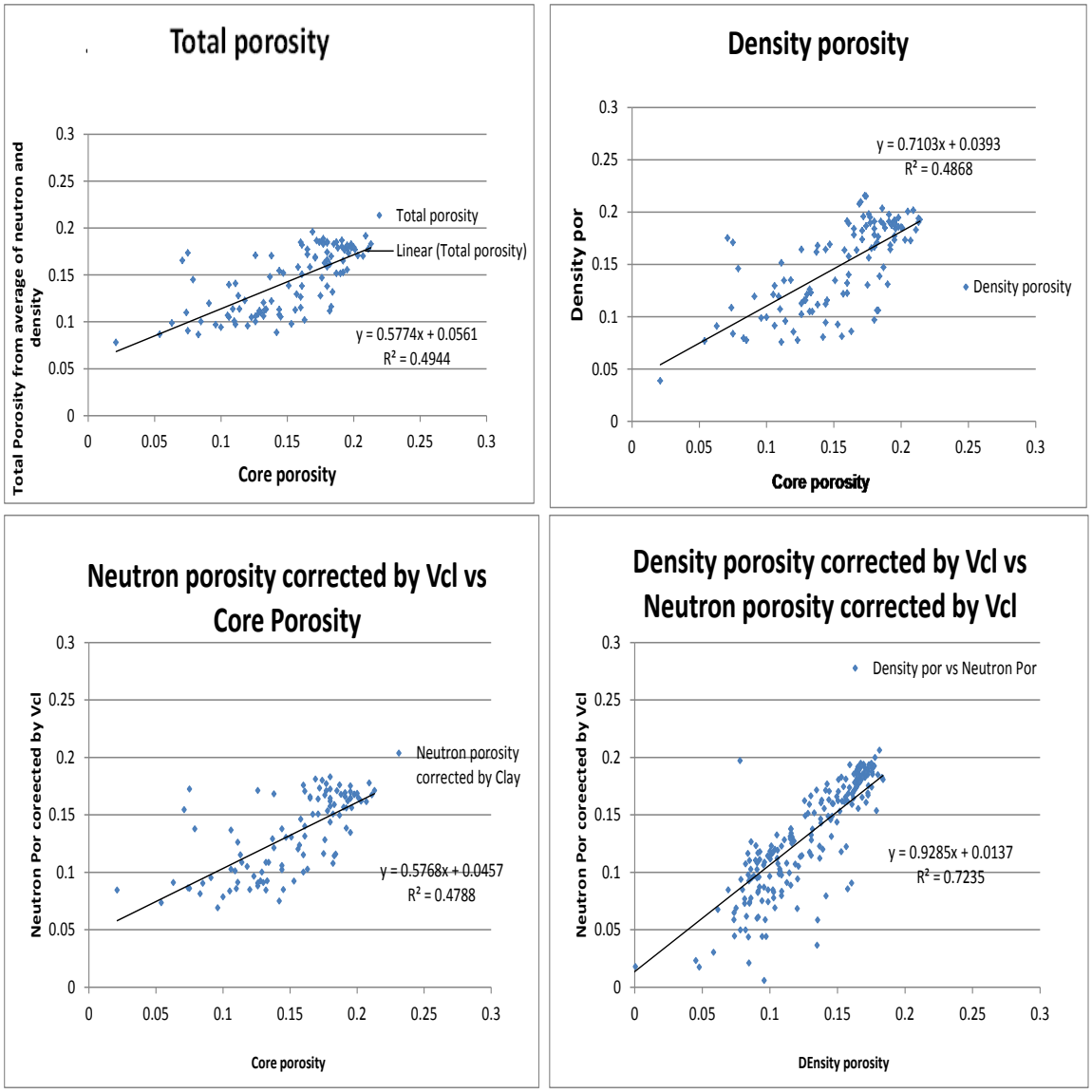

Figure 15. Correlation of the well logs density and the core density by the average N-D porosity (upper left), density porosity (upper right), neutron Porosity (down). Well C-9

The correlation coefficient from the total porosity (ϕ_t) vs. the core porosity is higher than the correlation coefficient from density porosity vs. core porosity. Neutron porosity corrected by Vcl vs. core porosity cross plot shows the lowest correlation coefficient. Also, the ϕ_t vs. core porosity plot shows less scattering than the density porosity plot. In relation to the fact that neutron porosity shows the lowest correlation, it must be taken into account that neutron is affected by the hydrogen nuclei contained in clays. The correlation coefficient value between density porosity corrected by Vcl and neutron porosity corrected by Vcl shows that measurement are consistent in both logs since this is sandstone with oil that has similar density to water. Figure 16 shows the plot of the Core porosity and ϕ_t from well logs.

Three approaches were used to calculate the water saturation through well logs. Indonesian (Poupon, A, et al., 1971), Modified Simandoux (Bardon, C., et al., 1969), and Dual Water (Clavier, C., et al. 1977) methods were applied.

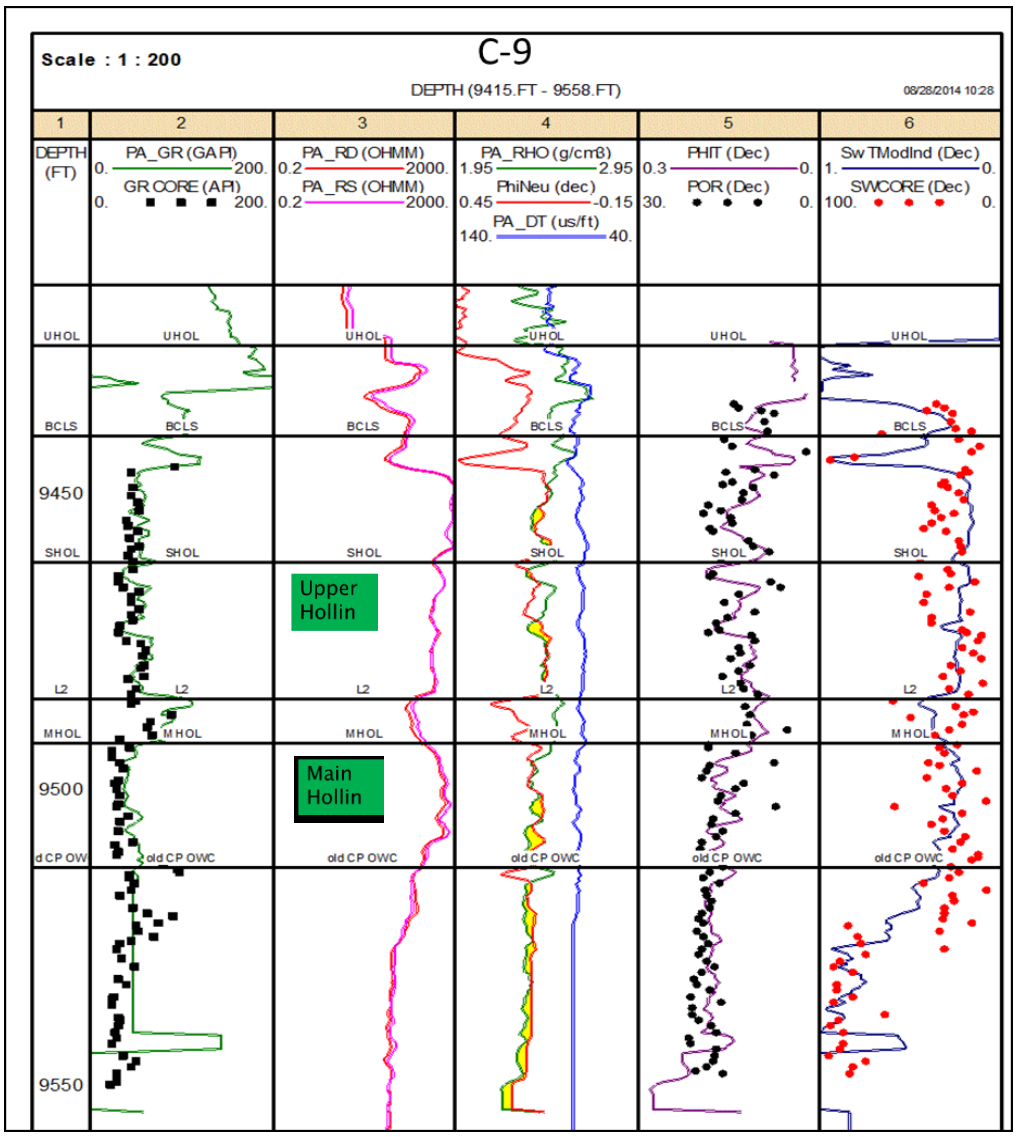

Figure 16. Plot of the core porosity, average N-D porosity and density porosity. (Main Hollin and Upper Hollin). Well C-9

The best correlation with core measurements was obtained by the Indonesian method since it was originally deducted from fresh water bearing sandstones and Main Hollin has a salinity of 100 ppm NaCl and Upper Hollin has a salinity of 500 ppm NaCl.

$$\frac{1}{\sqrt{R_t}} = \left(\sqrt{\frac{\phi_s^m}{a * R_w}} + \frac{Vcl^{\left(1-\frac{Vcl}{2}\right)}}{\sqrt{R_{sh}}} \right) * S_{ws}^{\frac{n}{2}} \quad (26)$$

$$S_{wt} = \frac{\phi_s * S_{ws}}{\phi_t} + S_{wb} \quad (27)$$

$$S_{wb} = Vcl \frac{\phi_{sh}}{\phi_t} \quad (28)$$

where

R_t is the deep resistivity measurement

m is the cementation factor =1.8 and

Rw is the water resistivity. For Main Hollin formation salinity is 100 ppm NaCl and for Upper Hollin it is 500 ppm NaCl

n is the saturation exponent =1

a is the tortuosity factor = 1

R_{sh} is the deep resistivity in a zone of pure shale

S_{ws} is the effective water saturation

S_{wb} is the clay bound water saturation and

With the application of the Indonesian equation, a correlation coefficient of 0.62 is obtained as shown in Figure 17.

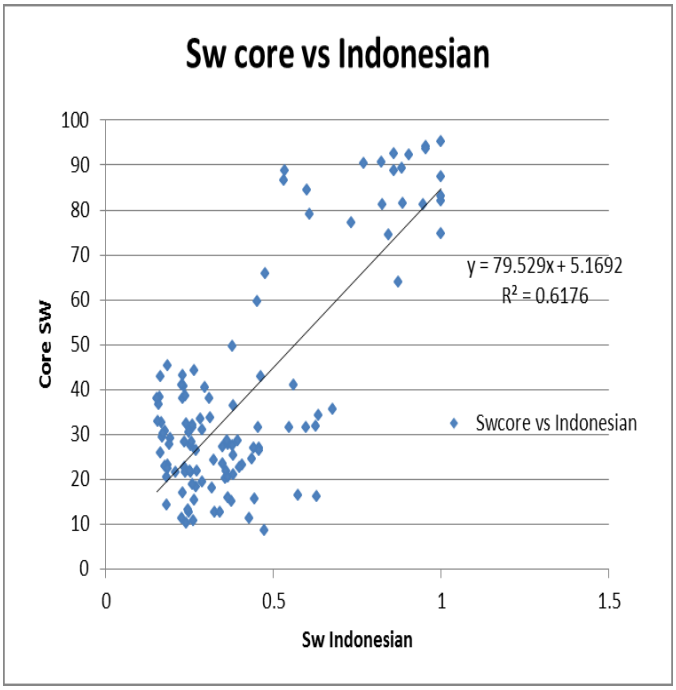

Figure 17. Correlation of Water saturation from well log analysis and from core data Upper Hollin and Main Hollin. Well C-9

After this analysis, the same approaches used to calculate the Vcl, porosity and water saturation will be used for all wells in Upper and Main Hollin sandstones.

Rock Physics model for Hollin sandstone

One of the objectives of the rock physics analysis is to tie the elastic properties to petrophysical properties of the rock such as porosity, saturation, permeability. Using the well logs to create elastic properties curves assuming isotropic characteristics, we can then analyze the correlation of each of the elastic properties to characteristics that define the quality of the reservoir and its productivity.

In Main Hollin, the majority of the mineral concentration is quartz as it was stated before; low concentration of kaolinite and potassium feldspar are also present in the rock. Due to low concentration of other radioactive elements in the rock, they were not taken into account in the calculus of the elastic properties. They present a negligible effect on the elastic modulus of the rock. In Upper Hollin, the presence of glauconite affects the values of gamma ray as well as kaolinite. Pyrite is present as some traces especially in the zones of more marine influence that are correlated with intervals with high clay content.

In order to test the quality of the well logs, synthetic density log will be calculated using the equation 29

$$\rho = (1 - \phi)\rho_s + \phi\rho_f \quad (29)$$

where

ρ is the bulk density

ϕ is the porosity

ρ_s is the density of the solid matrix

ρ_f is the density of the fluid

ρ_s is calculated assuming that Vcl is affected by the presence of K-feldspar and Kaolinite in Main Hollin. The density values of these two components are similar as it is presented in Table 1

Mineral	Compresibility Factor (Gpa)	Shear modulus (Gpa)	Density (g/cm3)
Quartz (Mavko,2009)	39	45	2.65
Calcite (Mavko,2009)	65	30	2.71
Kaolinite (Avseth and et al., 2013)	37.9	14.8	2.69
Glauconite (Diaz et al.,2002)	15	10	2.96
K feldspar (Mavko,2009)	37.5	15	2.62
Pyrite (Mavko,2009)	147.32	132.5	4.93

Table 1 Elastic modulus and density of the main minerals present in Hollin and U reservoir.

To calculate ρ_s two considerations will be set; first, solid matrix is composed of a fraction of quartz and a fraction of non-quartz constituents. As it was stated before, it is assumed that Vcl is composed by kaolinite in Main Hollin. Density of the non-quartz fraction (ρ_{clay}) is assume to be the density of kaolinite for Main Hollin sandstone.

Equation 30 represents the approach used for the calculation of ρ_s in Main Hollin sandstone

$$\rho_s = (1 - \phi - (Vcl - Vcl * \phi_{sh})) * \rho_{quartz} + (Vcl - Vcl * \phi_{sh}) * \rho_{clay} \quad (30)$$

For the Upper Hollin, if Vcl is less than 0.4, the ρ_s is calculated by the formula,

$$\rho_s = (1 - \phi - (Vcl - Vcl * \phi_{sh})) * \rho_{quartz} + (Vcl - Vcl * \phi_{sh}) * \rho_{clay} \quad (31)$$

ρ_{clay} is the average of glauconite and kaolinite from Table 1

When the Vcl is higher than 0.4, the calculus of the ρ_s will be

$$\rho_s = (1 - \phi - (Vcl - Vcl * \phi_{sh}) * 0.98) * \rho_{quartz} + (1 - \phi - (Vcl - Vcl * \phi_{sh}) * 0.02) * \rho_{pyrite} + (Vcl - Vcl * \phi_{sh}) * \rho_{clay} \quad (32)$$

In Hollin the oil is 26.4º API that is equal to 0.893 @103.3 º C and the reservoir pressure is 4000 psi. The density of the brine in Main Hollin and Upper Hollin that have a salinity of 100 and 500 ppm NaCl respectively were calculated using the following equations, (Batzle et al, 1992):

$$\rho w = 1 + 1x10^{-6}(-80\mathrm{T} - 3.3T^2 + 0.00175T^3 + 489P - 2TP + 0.016T^2P - 1.3x10^{-5}T^3P - 0.333P^2 - 0.002TP^2) \quad (33)$$

$$\rho B = \rho w + S\{0.668 + 0.44S + 1x10^{-6}[300\mathrm{P} - 2400\mathrm{PS} + \mathrm{T}(80 - 3\mathrm{T} - 3300S - 13P + 47PS)]\} \quad (34)$$

where ρw is the density of the water at reservoir conditions and ρB is the density of brine at reservoir conditions. *T* and *P* are the temperature and pressure at reservoir conditions and *S* is the salinity of the brine

The density of the fluid is calculated using the following equation:

$$\rho f = Sw * (\rho B) + (1 - Sw) * \rho oil \quad (35)$$

Water saturation is represented by Sw and saturation of oil is equal to 1-Sw.

This approach was performed for each of the 4 wells that has S wave sonic curves (C-30, C-31, C-33 and C-21)

Figure 18 and 19 show the comparison between the real density logs and the synthetic ones from wells C-30 and C-31in Hollin sandstone.

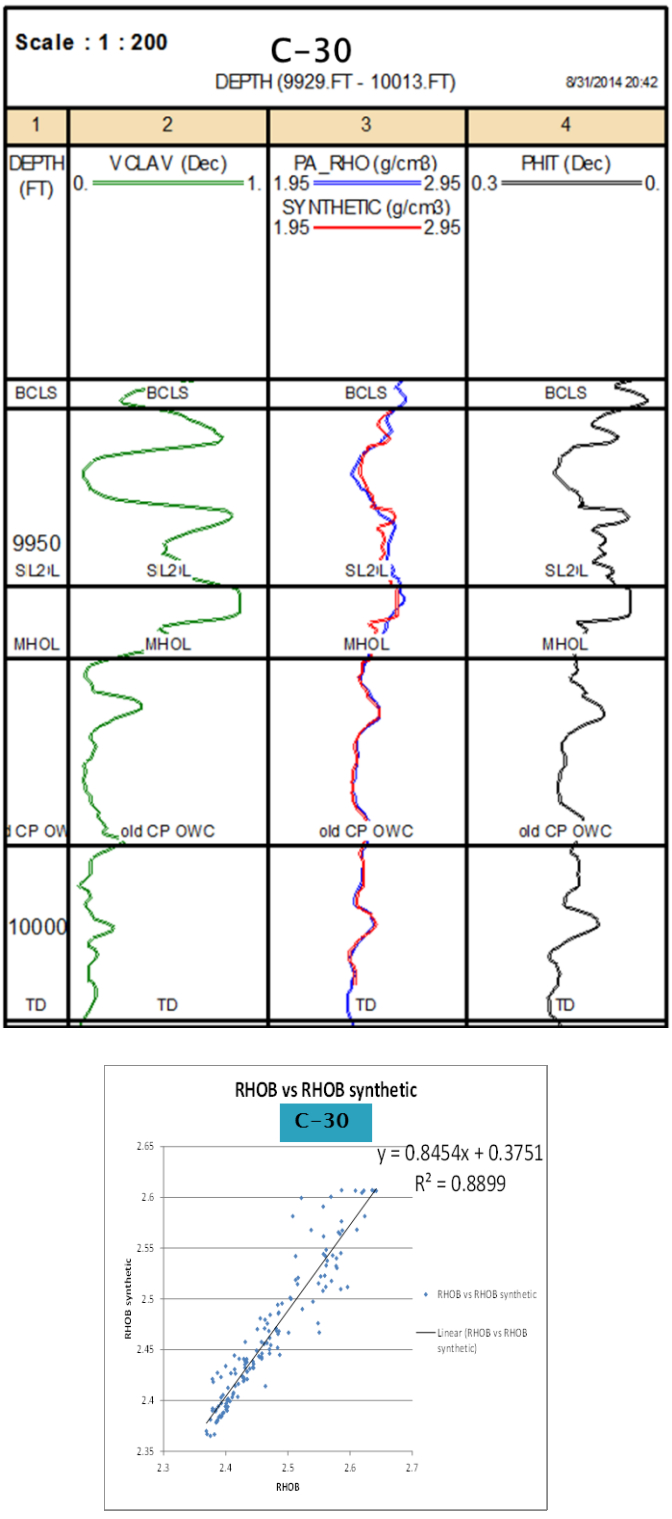

Figure 18. Comparison between real density log and synthetic log in Hollin reservoir for well C-30

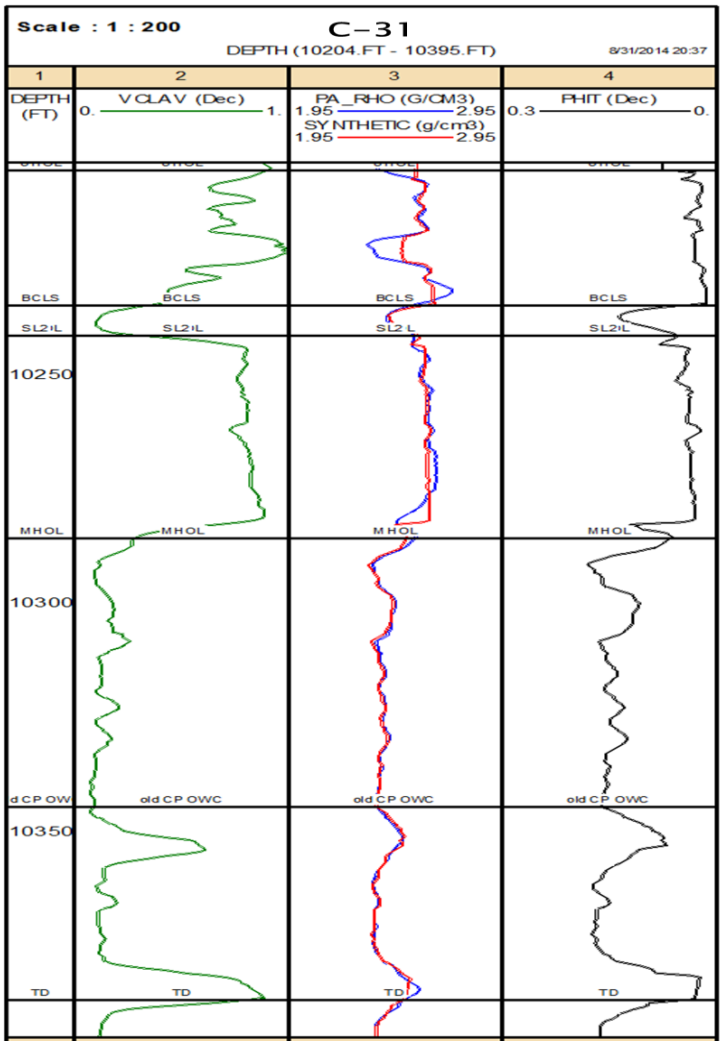

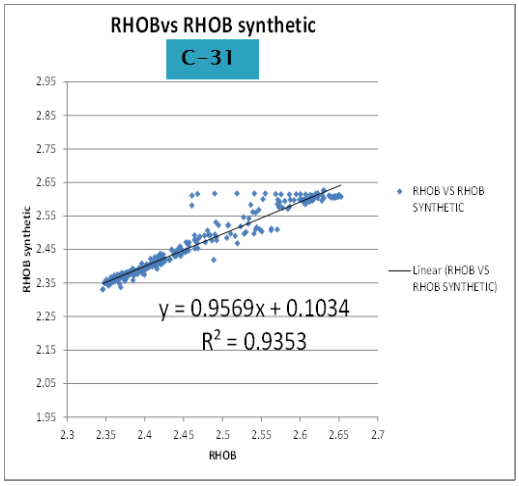

Figure 19. Comparison between real density and synthetic log in Hollin reservoir for well C-31

The correlation between real and synthetic density is high; hence, the assumed approach seems to be effective in spite of the fact that some scattering is present in the cross plots. These points that are out of trend belongs to the more shaly zones of the formations; therefore, it is difficult to exactly represent the density log in shale zones due to their heterogeneous composition and because of the assumption of homogeneous composition from sands that is applied to the whole section.

First of all, the calculus of the bulk modulus and shear modulus assuming an isotropic media is performed using the equations 36 and 37

$$K = V_p^2\rho - \frac{4}{3}V_s^2\rho \quad (36)$$

$$\mu = V_s^2\rho \quad (37)$$

Using the density log, the porosity log (ϕ), Vcl log, water saturation log (Sw), P sonic log and S-sonic log from the four wells, the bulk modulus of the solid matrix (K_s) and shear modulus of the solid matrix (μ_s) are calculated. The average of Voigt, 1910 and Reuss,1929' bounds equations is used for the calculus of the K_s and μ_s.

For Main Hollin, equation 37 is used for the calculus of K_s which includes the average of the Voigt and Reus bounds and the fraction estimation of non-quartz and quartz materials.

$$K_s = \frac{1}{2} * \left\{ \left(\left(1 - \phi - (Vcl - Vcl * \phi_{sh})\right) * K_{quartz} + (Vcl - Vcl * \phi_{sh}) * K_{clay} \right) + \left(\frac{1}{\frac{1-\phi-(Vcl-Vcl*\phi_{sh})}{K_{quartz}} + \frac{Vcl-Vcl*\phi_{sh}}{K_{clay}}} \right) \right\} \quad (39)$$

where K_{clay} is the bulk modulus of Kaolinite. The possible influence of K-feldspar in gama ray will not produce error in the K_s calculations due to the similar value the bulk modulus of Kaolinite and K-feldspar in the case of Vcl has been affected by k-feldspar presence in some zones.

In Upper Hollin, if the Vcl is lower than 0.4, then equation 37 will be used to calculate K_s. K_{clay} values come from the measurement of bulk modulus logs in 90% clay content zones since in Upper Hollin the Vcl is affected by glauconite and kaolinite and little quantitities of other heavy minerals. This fact does not allow averaging the bulk modulus of all the constituents.

When the Vcl is higher than 0.4 then equation 40 is applied

$$K_s = \frac{1}{2} * \left\{ \left(\left(1 - \phi - (Vcl - Vcl * \phi_{sh})\right) * K_{quartz} * 0.98 + (1 - \phi - (Vcl - Vcl * \phi_{sh}) * K_{pyrite} * 0.02 + (Vcl - Vcl * \phi_{sh}) * K_{clay} \right) + \left(\frac{1}{\frac{1-\phi-(Vcl-Vcl*\phi_{sh})}{K_{quartz}} + 0.98 + \frac{1-\phi-(Vcl-Vcl*\phi_{sh})}{K_{pyrite}} * 0.02 + \frac{Vcl-Vcl*\phi_{sh}}{K_{clay}}} \right) \right\} \quad (40)$$

The μ_s is calculated with the same equations used for K_s and with the same assumptions. K_f is calculated using the equation 41 that comes from the average of Voigt, 1910, and Reuss, 1929' bounds also.

$$K_f = \frac{1}{2} * \left\{ [K_{0il} * (1 - S_w) + K_w(S_w)] + \frac{1}{\left[\frac{(1-S_w)}{K_{0il}} + \frac{S_w}{K_w}\right]} \right\} \quad (41)$$

where K_{oil} and K_w are calculated with correlations from Baztle et al., 1992 with constant values of 1.49 GPa and 2.489 GPa respectively.

Sun 2000' model is used in order to obtain the compressional frame flexibility factor and the shear flexibility factor using a rearrangement of equations 9, 10, 11, 12 and 13 and the addition of the variable *f* that is defined by Sun, 2000 as the frame stiffness factor which describes the stiffness and rigidity of the rock frame under deformation due to both pore structures and porosity, (Sun, 2004).

$$f = (1 - \phi)^{\gamma_k - 1} \quad (42)$$

$$f = \frac{1 - \left(\frac{K_f}{K_s} + \left(1 - \frac{K_f}{K_s}\right)\phi\right) F_k}{(1-\phi)\left(1 - \frac{K_f}{K_s} F_k\right)} \quad (43)$$

where

$$F_k = \frac{K_s - K}{\phi\left(K_s - K_f\right)} \quad (44)$$

Rearranging the equations 42 and 12 gives respectively

$$\gamma_k = 1 + \frac{Ln(f)}{Ln(1-\phi)} \quad (45)$$

$$\gamma_u = \frac{ln\left(\frac{\mu}{\mu_s}\right)}{\ln(1-\phi)} \quad (46)$$

c ratio is calculated with equation 13,($c = \frac{\gamma_\mu}{\gamma_k}$) in the wells C-30, C-31, C-21 and C-33. Figure 7 shows the frequency distribution of *c* ratio and the cross plot of *c* ratio vs. porosity with Vcl in z axis for the Upper Hollin. Figure 8 shows the same plots for the Main Hollin. It can be determined from the cross plots that the shaly zones present different average values of *c* ratio from sandstones. Also, *c* ratio from these shaly zones produce scattering in the trend that is interpreted as the heterogeneity of shaly zones due to variability in their mineral content and in their pore structure. This fact shows that close intervals have different seismic velocities responses. Upper Hollin presents specific zones with tidal bars that are the prolific part of the reservoir, but the rest of the zones in Upper Hollin are shaly carbonate sandstones with interbedded shales (well C-30 in Figure 10) with non-productive petro physical characteristics. Based on these considerations the average *c* ratio for Upper Hollin is 1.18.

Based on Sun, 2000' model, Adesokan et al., 2010 established that for shaly sandstones, the critical clay volume (Vcl cut off) that determines the limit in which the elastic properties of rock change is around 0.32. From Figure 20, that is the cross plot of P-velocity vs. Vcl, a change in the trend from shaly sandstones to sandy shales can be found. The limit for change in P-velocity behavior is around 0.4 and it agrees with the value of Vcl cut off established by Petroamazonas EP to define reservoir based on production experience. This critical clay volume can be understood assuming that clay is inside the grain pores. In clean sandstone the grains are connected, then; the space between the grains is filled by the clay and results in isolated grains. Therefore, the zone

in which we can visualize a change in the trend of the velocity is the zone in which the rock changed from grain supported to clay supported.

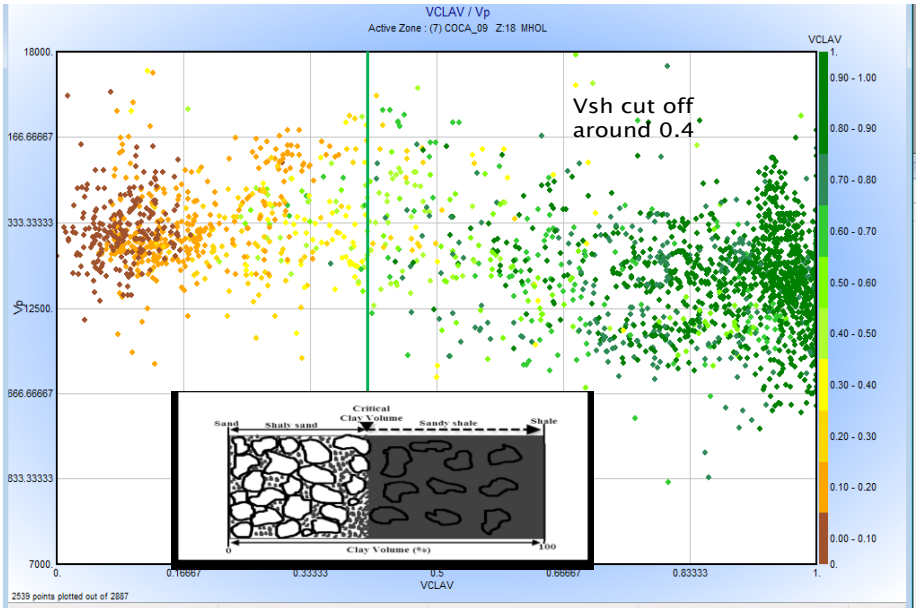

Figure 20. Determination of the critical volume of shale (Vcl cut off)

The cut off value of Vcl is applied in order to discriminate the shaly zones from tidal bars in Upper Hollin as shown in Figure 7. The value of average *c* ratio for shaly zones, with a Vcl higher than 0.4, is 1.26. The *c* ratio for tidal bars, with Vcl lower than 0.4, is 0.89. These *c* ratio values will be used then in the creation of synthetic S wave curve for other wells using the equation 46 which is a rearrangement of the previous equations from Sun, 2000.

$$V_s = \sqrt{\frac{\mu_s(1-\phi)^{c*\gamma_k}}{\rho_s(1-\phi)+\phi\rho_f}} \tag{45}$$

where $\phi, \rho_s, \rho_f, \mu_s$ and γ_k come from rock physics analysis

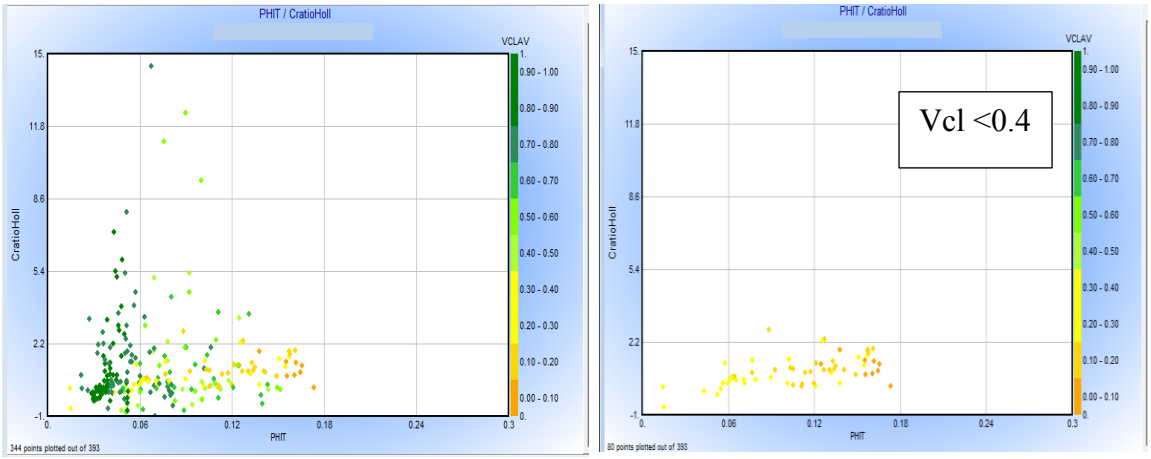

Curve	Well	Zone	Top	Bottom	Min	Max	Std Dev	Mean	Mode	P10	P50	P90
CratioHoll	_21	BCLS	9798 FT	9844 FT	-0.65998	2.7446	0.7529	0.7029	0.44	0.24524	0.40755	1.3902
CratioHoll	_21	SHOL	9798 FT	9844 FT	-0.65998	2.7446	0.7529	0.7029	0.44	0.24524	0.40755	1.3902
CratioHoll	_21	L2	9844 FT	9860.5 FT	0.39614	2.7446	0.80855	1.3776	0.44	0.54264	1.2558	1.9065
CratioHoll	_30	BCLS	9932.5 FT	9955.5 FT	-0.1095	2.3287	0.65194	1.2749		0.77974	1.2171	2.2515
CratioHoll	_30	SHOL	9955.5 FT	9955.5 FT								
CratioHoll	_30	L2	9955.5 FT	9965 FT	0.39792	0.84598	0.31682	0.62195		0.39792	0.39792	0.84598
CratioHoll	_31	BCLS	10235 FT	10241.5 FT	0.049187	1.4585	0.37489	0.9372	1.08	0.40634	0.96357	1.4023
CratioHoll	_31	SHOL	10241.5 FT	10241.5 FT								
CratioHoll	_31	L2	10241.5 FT	10286 FT	0.15191	0.63137	0.17008	0.46548	0.44	0.15191	0.5164	0.56021
Overall						2.7446	0.68918	0.88551	0.44	0.24524	0.81205	1.8473

Figure 21. Cross plot of the *c* ratio vs. ϕ with Vcl in the z axis for the Upper Hollin sandstone (Upper). The frequency distribution of *c* ratio for Upper Hollin sandstone, Vcl<0.4 (Lower)

The Main Hollin interval is clean sandstone that presents a constant *c* ratio value of 1.17, (Figure 21). This fact can be interpreted as a homogenization of the pore structure in the majority of the sandstone. Main Hollin shows a similar compressibility response to the shear motion. A few thin shaly intervals caused the scattering of some points as it is seen in the cross plot of the *c* ratio vs. ϕ. To obtain more accurate S wave curve for the Main Hollin sandstone, the cut off of Vcl< 0.4 is applied to calculate the average c ratio. This cut off value is applied since the shale intervals are thin and not representative of the whole section. This value is 1.18.

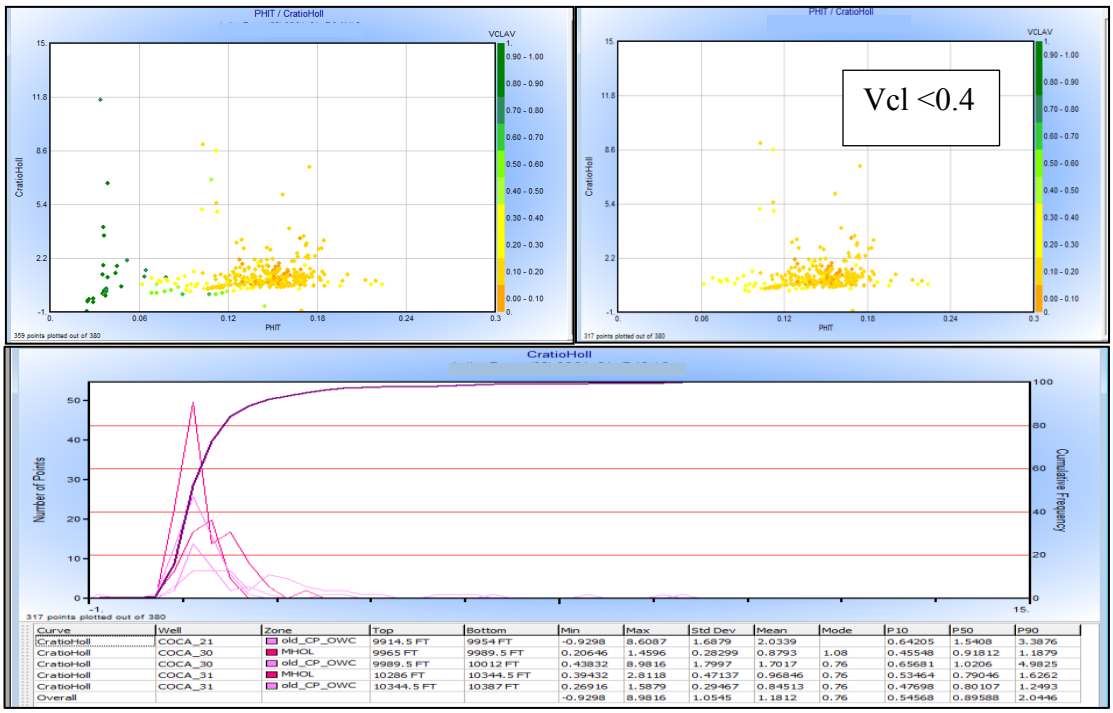

Curve	Well	Zone	Top	Bottom	Min	Max	Std Dev	Mean	Mode	P10	P50	P90
CratioHoll	COCA_21	old_CP_OWC	9914.5 FT	9954 FT	-0.9298	8.6087	1.6879	2.0339		0.64205	1.5408	3.3876
CratioHoll	COCA_30	MHOL	9965 FT	9989.5 FT	0.20646	1.4596	0.28299	0.8793	1.08	0.45548	0.91812	1.1879
CratioHoll	COCA_30	old_CP_OWC	9989.5 FT	10012 FT	0.43832	8.9816	1.7997	1.7017	0.76	0.65681	1.0206	4.9825
CratioHoll	COCA_31	MHOL	10286 FT	10344.5 FT	0.39432	2.8118	0.47137	0.96846	0.76	0.53464	0.79046	1.6262
CratioHoll	COCA_31	old_CP_OWC	10344.5 FT	10387 FT	0.26916	1.5879	0.29467	0.84513	0.76	0.47698	0.80107	1.2493
Overall					-0.9298	8.9816	1.0545	1.1812	0.76	0.54568	0.89588	2.0446

Figure 22. Cross plot of the c ratio vs. ϕ with Vcl in the z axis for the Main Hollin reservoir (Upper). The frequency distribution of c ratio for Main Hollin sandstone, Vcl<0.4 (Lower)

It is concluded that Sun, 2000' model will be more accurate for the creation of S wave curves in clean sandstones since the *c* ratio is constant and does not present scattering as in shaly zones because in shaly zones and shales (Vcl> 0.4) the pore structure is very complex and the anisotropic characteristics produce a non-uniform relationship of the compressibility to the shear motion. This anisotropy has an intimate relation with the mineralogical heterogeneous composition of shales and shaly sands.

Feasibility of the project for Hollin sandstone

The same assumption that states a constant value of *c* ratio will be used to invert porosity and frame flexibility factor from inversion results using a rearrangement of the Sun, 2000' model equations and the bulk modulus, shear modulus which results from the inversion. First, it is needed to establish an elastic parameter that allows to discriminate clean sandstone from shale and sandy shale since Sun's model is more reliable when Vcl <0.4 under the assumption of constant *c* ratio. From the inversion, the main outcomes will be the P-Impedance volume, S-Impedance volume and density volume. Using these elastic parameters and other ones derived such as, Poisson ratio, lambda-rho, mu-rho and trying with a combination of different cross plots, the best cross plot option for the discrimination of sand and shale was chosen.

Application of P- impedance Inversion will not be useful to discriminate sandstone from shale since both of them present similar P- impedance values as shown in the cross plot of P-Impedance vs. Vcl. (Figure 23).

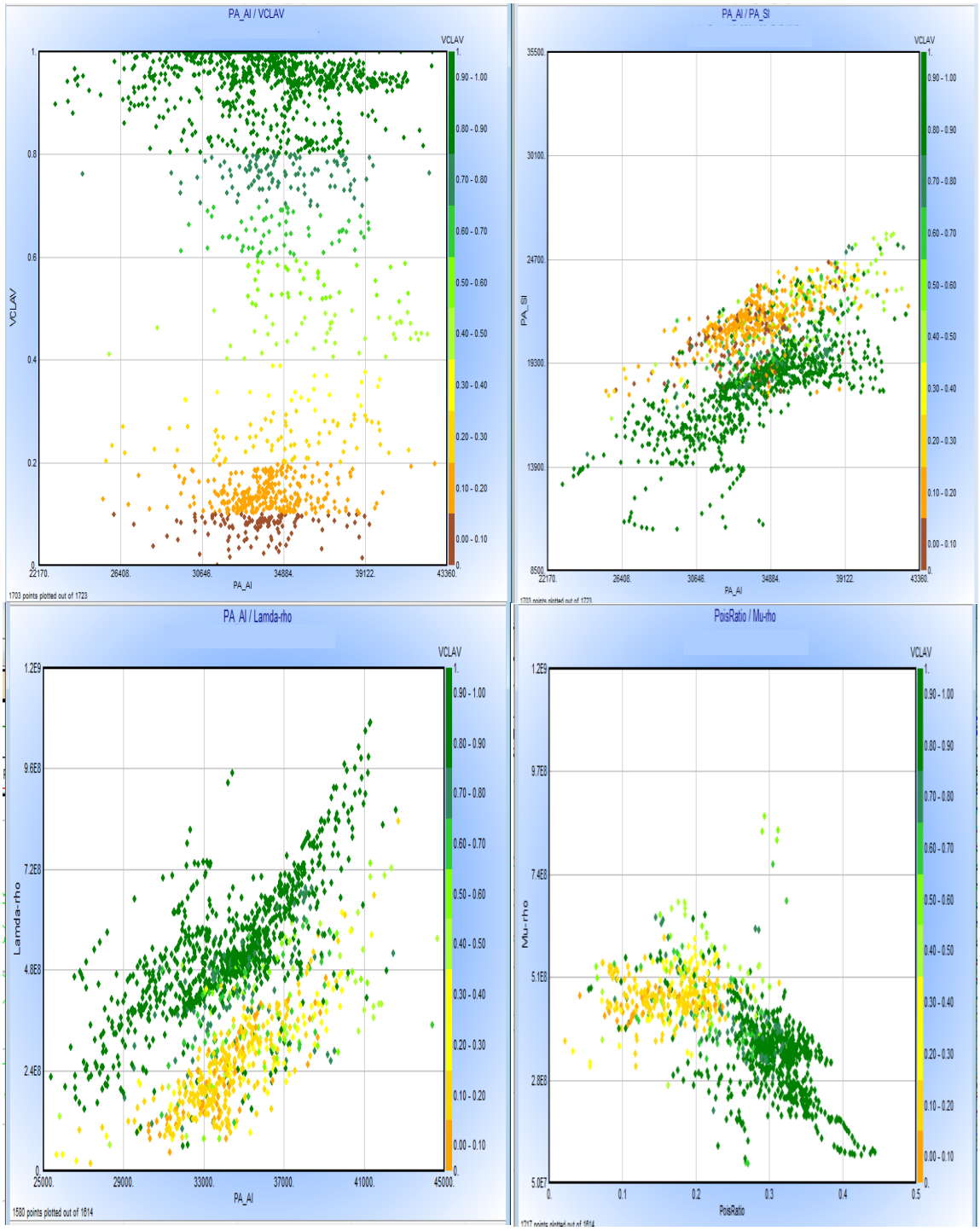

Figure 23.Different cross plots of elastic parameters to discriminate Hollin from the overlaying shale (LNSH). Wells C-21, C-30, C-31.

The results from Simultaneous inversion shows that Hollin sandstone can be separated from Lower Napo shale (LNSH) in a reasonable way using the cross plots of P-Impedance vs. S-Impedance, P-impedance vs. Lambda-rho and Poisson vs. Mu-rho, Figure 23.

Hollin sandstone is characterized by an active aquifer that produces conning in most of the wells leaving big quantities of reserves behind the cones. Between drilled wells oil gets trapped since the high water cut production compel to close wells and extensive upswept zones keep remaining. Figure 24 shows that there is no possibility to discriminate water bearing zones from oil bearing zones in Hollin sandstone, because of the similarity in density between water and oil.

In order to use the core data from the well C-9 and analyze any tie between the descriptions of the core with the result of the rock physics analysis, the synthetic S-wave curve of well C-9 was created. For the zones with Vcl less than 0.4 equation 45 was used but for zones with a Vcl higher than 0.4, the empirical relations form Greenberg and Castagna, 1992 were used.

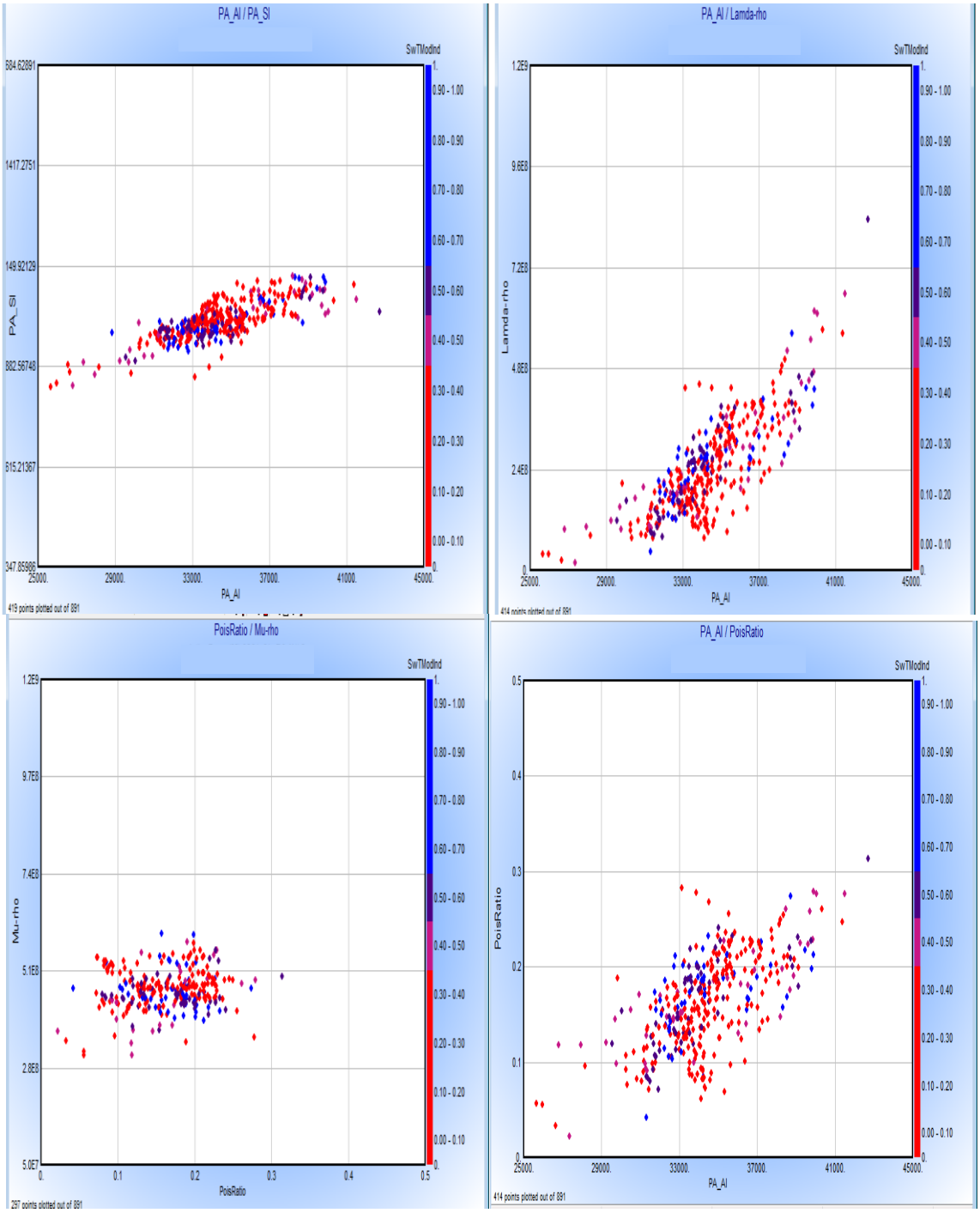

Figure 24. Different cross plots of elastic parameters to discriminate water bearing zones from oil bearing zones in Hollin .Cut off of Vcl>0.4. Wells C-21, C-30 and C-31.

Figure 25 is a cross plot of P impedance vs. ϕ with the frame flexibility factor (γ_k) in z axis. First, from this graph it is obvious that the relationship of porosity and P-Impedance is not as simple as a straight line. Then, because different zones with similar γ_k values have different P-Impedance vs. porosity relationships, Sun, 2000'model must be applied to the reservoirs in order to obtain a reliable porosity from seismic attributes.

The shale zones produce a strong scattering in the relationship of P-impedance with Porosity. In the upper part of Figure 25, the Vcl is used in the z axis demonstrating that shale zones have erratic values of γ_k when a comparison is made with the same plot with *Vcl* in z axis.

Comparing the value of γ_k with the description of core data reveals that the best facies has a γ_k value higher than 6 and porosity higher than 0.12. These are represented by clean sandstone with a medium to coarse grain size and well sorted. This facies can be classified as fluvial and tidal bars (Vallejo et al., 2013). Figure 25 shows some zones that in spite of the fact that belongs to some γ_k value, they are out of the trend. These zones belong to the well C-21 in which the measurement of P-sonic shows having some problems probably associated to wrong picking and interpretation process. Also in Figure 25, the bulk modulus is use in the z axis. Good reservoir quality, associated to medium to coarse grain size and clean sandstone without laminations or traces is related with lower values of bulk modulus. Laminations and traces have a direct impact in the reduction of porosity; however, the reduction of porosity is not intrinsically related with the reduction of γ_k and K. The same effects happen with the sorting and grain size. At the end, it can be concluded that these three factors influences the value of γ_k and K. Also,

shear modulus is plotted in z axis; from this plot, it is obvious the inverse relationship between shear modules μ and porosity. Lower values of μ are related to higher porosity. From the core description it can be inferred that sorting and presence of inclusions are affecting the values of μ. Besides, in rocks with different size of grains, the porosity is reduced because more contact exits between the grains. Therefore, the resistance to shear, motion is stronger. It leads to think that strong relationship exists between μ and porosity. This hypothesis is confirmed with the cross plot of Figure 26 where S-Impedance vs. porosity is plotted. A fair relationship between these two parameters is found for facies with a Vcl less than 0.4. It is possible to use S-Impedance to derived porosity after inversion with certain degree of accuracy in clean sandstones. However, use of S-Impedance–porosity relationship will not allow discriminating facies from the inversion results as it could be possible with the inversion of γ_k. In conclusion, both porosity and frame flexibility factor must be used to depict the best quality facies.

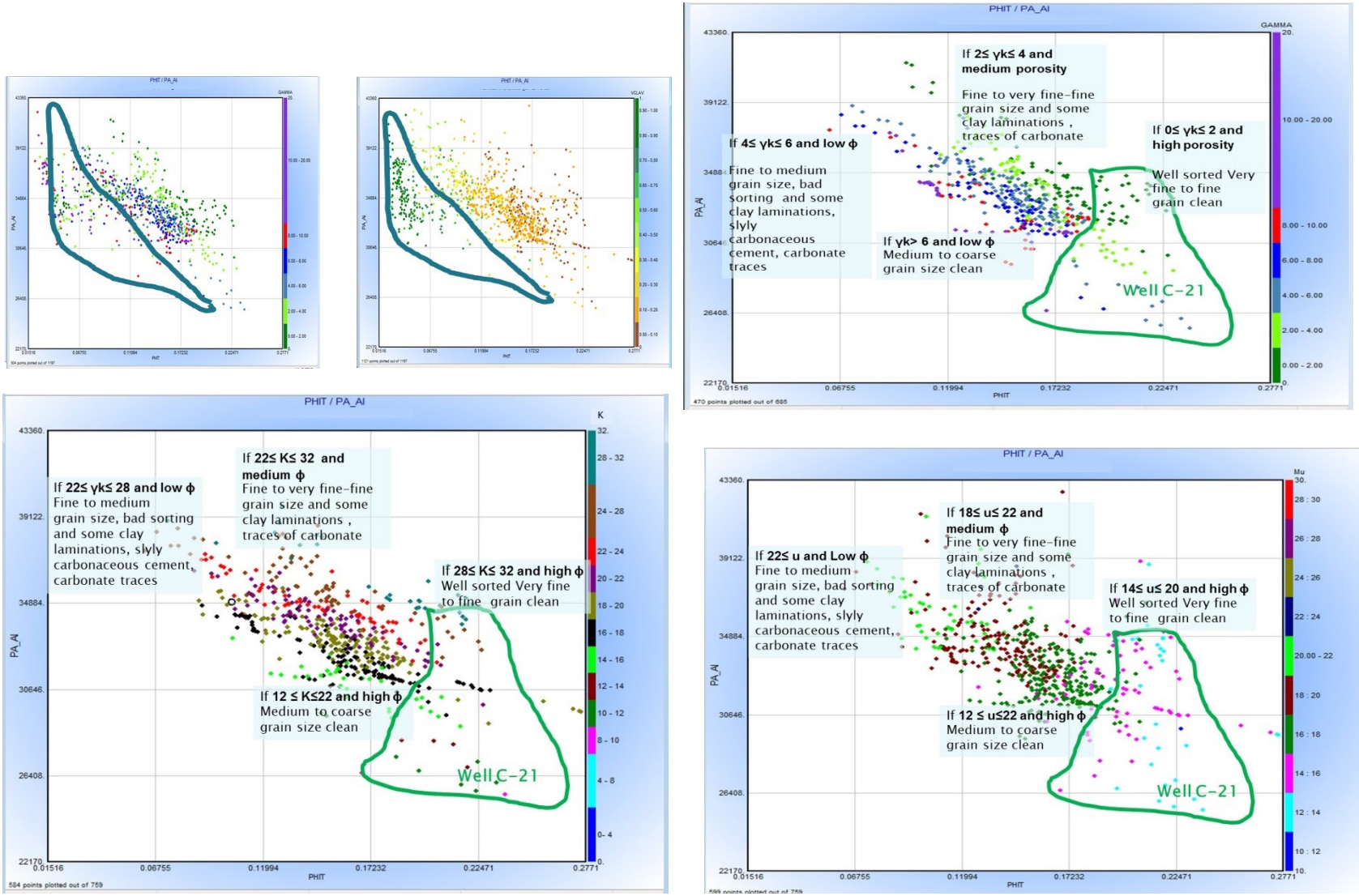

Figure 25. Cross plots of P-Impedance vs. porosity with γk in the z axis (a) ,Vcl in the z axis (b). The same cross plot with facies description using γk in the z axis (c), using K in z axis (d) and using u in z axis (e)

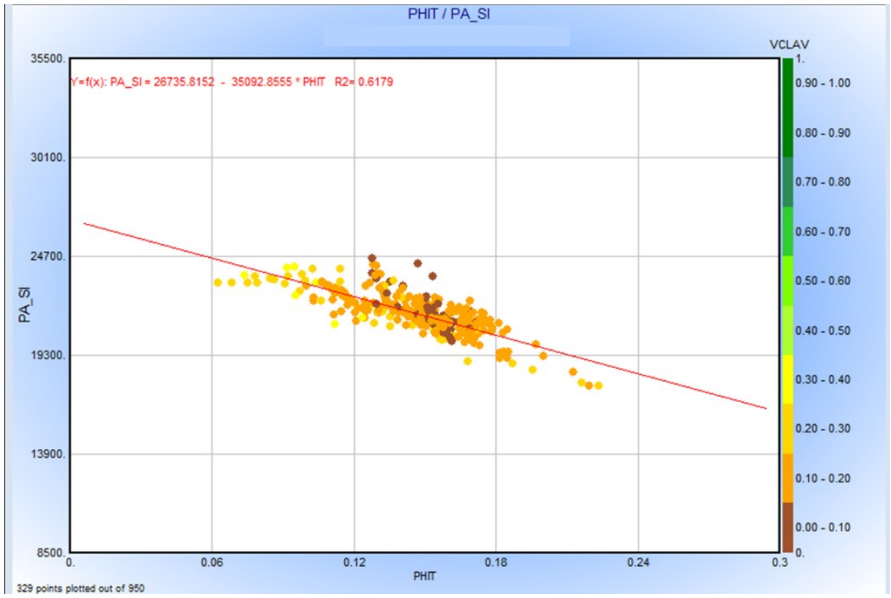

Figure 26. S- Impedance vs. porosity with Vcl

Main Hollin and tidal bars from Upper Hollin are in general good quality reservoirs that can comprise all the facies distinguished above in Figure 25. Hollin reservoir produces from all of these facies in a quantitative dependence of their quality according to production experience states. The main problem for exploration and development in Hollin reservoir is to depict water zones from oil zones. Based on this consideration an optimal outcome from inversion must be the depict WOC and unswept reserves between wells. For this specific case, rock physics model presents a limitation that is related of the non-influence in elastic parameters from fluid change in rocks. Neither the change in pressure depletion will be useful in this case since the Hollin active aquifer is recharged continuously from the foothills and maintained the pore pressure around 4000 psi continually in time. But, the power of rock physics model is

very important in the way of depicting the tidal bars facies extension in Upper Hollin from the glauconitic shaly sandtones. Upper Hollin presents a great cumulative production that it is only suppressed by the cumulative production of Main Hollin.

U sandstone

According to Vallejo et al., 2013, the Upper U sandstone depositional environment belongs to external platform and these shaly sandstones are productive in restrictive zones at the south west of the oilfield. The productive zones belong to shoreface bars but the rest of the sequences are glauconitic sandstones with very low porosity and very low permeability. (Vallejo et al., 2013). Unfortunately, there is not mineralogical analysis of the Upper U sandstone in productive zones; therefore, the drilling cuttings descriptions will be used instead. Upper U is very fine to fine grain size sandstone, with rounded to sub rounded grains shape, poorly sorted with kaolinite around grains, glauconite inclusions, some pyrite inclusions, calcite cement in some intervals and carbonate laminations.

Main U is more productive than Upper U and this is the main target for this research. Vallejo et al., 2013 states that there are tidal channels and bars that represent the most prolific part of the reservoir with a depositional trend with SE-NW direction. At the north of the studied zone these bars and channels pinch out reducing in quality from sand flats to mud flats the NW of the oilfield, Figure 27. Well C-21 and P-14 are separated by a distance of 1000 m; however, the abrupt change in facies in the whole U unit in evident.

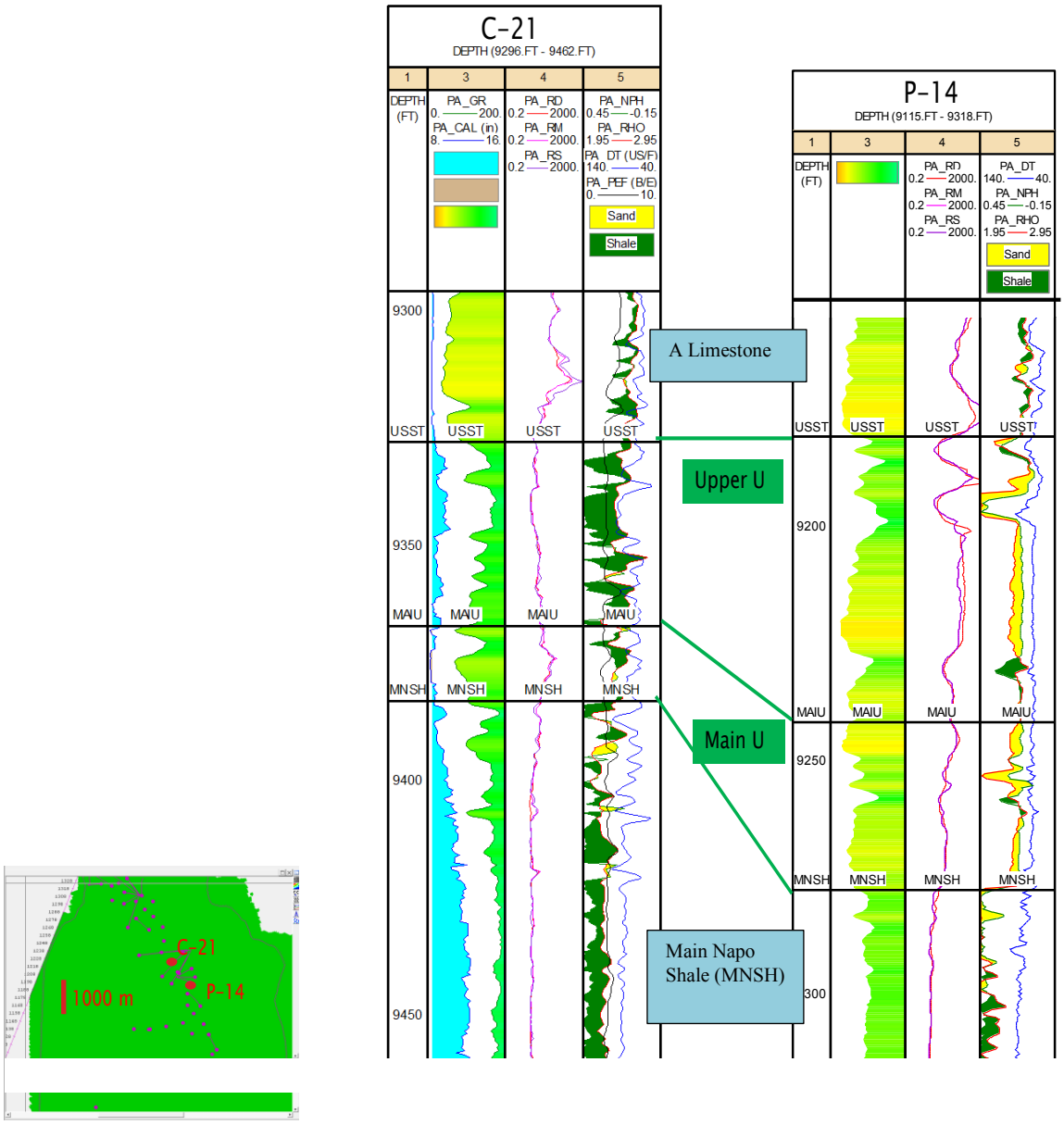

Figure 27. Well tie correlations showing the variation in quality of the Upper and Main U sandstone

Mineralogical composition of U Sandstone

Based on the non-published report Petroproduccion, 1994, the mineralogical composition of the Main U sandstone is composed of 85% of quartz, 14 % of K feldspar, muscovite, 1% of pyrite, kaolinite traces and less than 1% of zircon. Silica matrix is present in the majority of the interval. Some parts show slighly carbonate traces. Most of the non-quartz portion is kaolinite and k feldspar (Figure 28). Diagenesis in some zones produced the replacement of feldspar by carbonates. Presence of kaolinite could be interpreted as product of k-feldspar alterations. Grain size fluctuates from fine to medium. Some parts are well sorted and others are moderately sorted. Sub rounded to sub angular grains are present in most of the analyzed sections. Average grain size 0.3 mm – 0.125 mm and average pore throat size is 20 um (Figure 28).

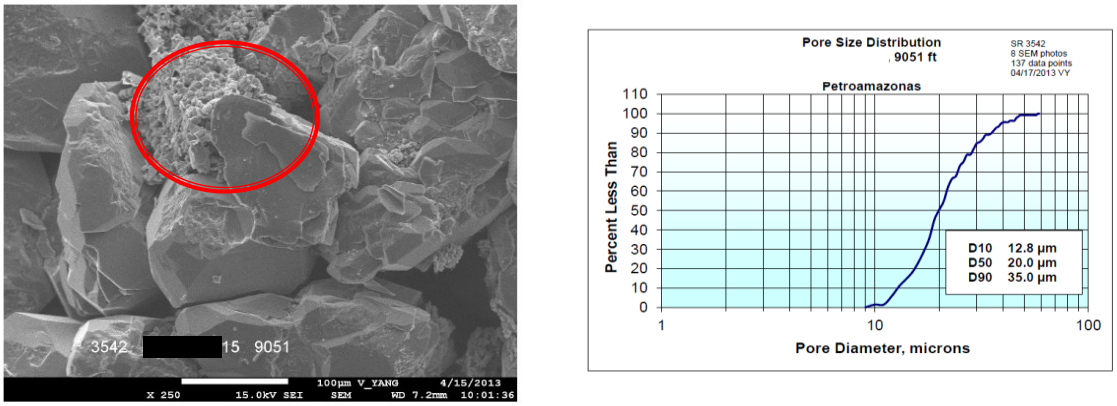

Figure 28. Microscopic images and pore throat size distribution from well P-15 Main U. Inside the red circle it is possible to see dispersed kaolnite. Halliburton, 2013

Upper U is a low quality reservoir; however as it was stated before, there are some specific zones that presents good quality. For these zones the average mineralogical composition is 76-85% quartz, and glauconite as structural grain in 2-5 %. Kaolinite is present in 7-15%, pyrite in 1-3%. Zones affected by diagenesis present calcite cement in a percentage of 1-2 %. Grain size fluctuates from very fine to fine and grain shape is between sub rounded to sub angular. Few laminations of clay and also some slighly carbonate laminations are proper in the zones of more marine influence.

Petro physical interpretation of U sandstone

U sandstone is evaluated following the same work flow as Hollin Formation. Porosity from core evaluation analysis in well P-15 was used to compare with porosity obtained by well logs. Figure 29 shows the cross plot of the porosity from core evaluation and porosity from well logs. At the top of the cored interval mud drapes intercalations affect the measurement of the logging tools causing a low correlation with core data. Conventional core analysis data is measured from plugs that are specifically chosen at intervals that present good characteristics to be tested but logging tools are affected by the shoulder bed effect. The resolution of this two methods is different. Mud drapes are located in the zone between 9050 and 9054 ft (Figure 30). Another zone that is located at 9071-9072 ft causes scattering in the correlation. In this zone the influence of the underlying mud clasts affects the tools measurements.

In figure 29, it can be seen the correlation between ϕ_D^{sh} and ϕ_N^{sh}. This correlation assures the quality of the logging measurements.

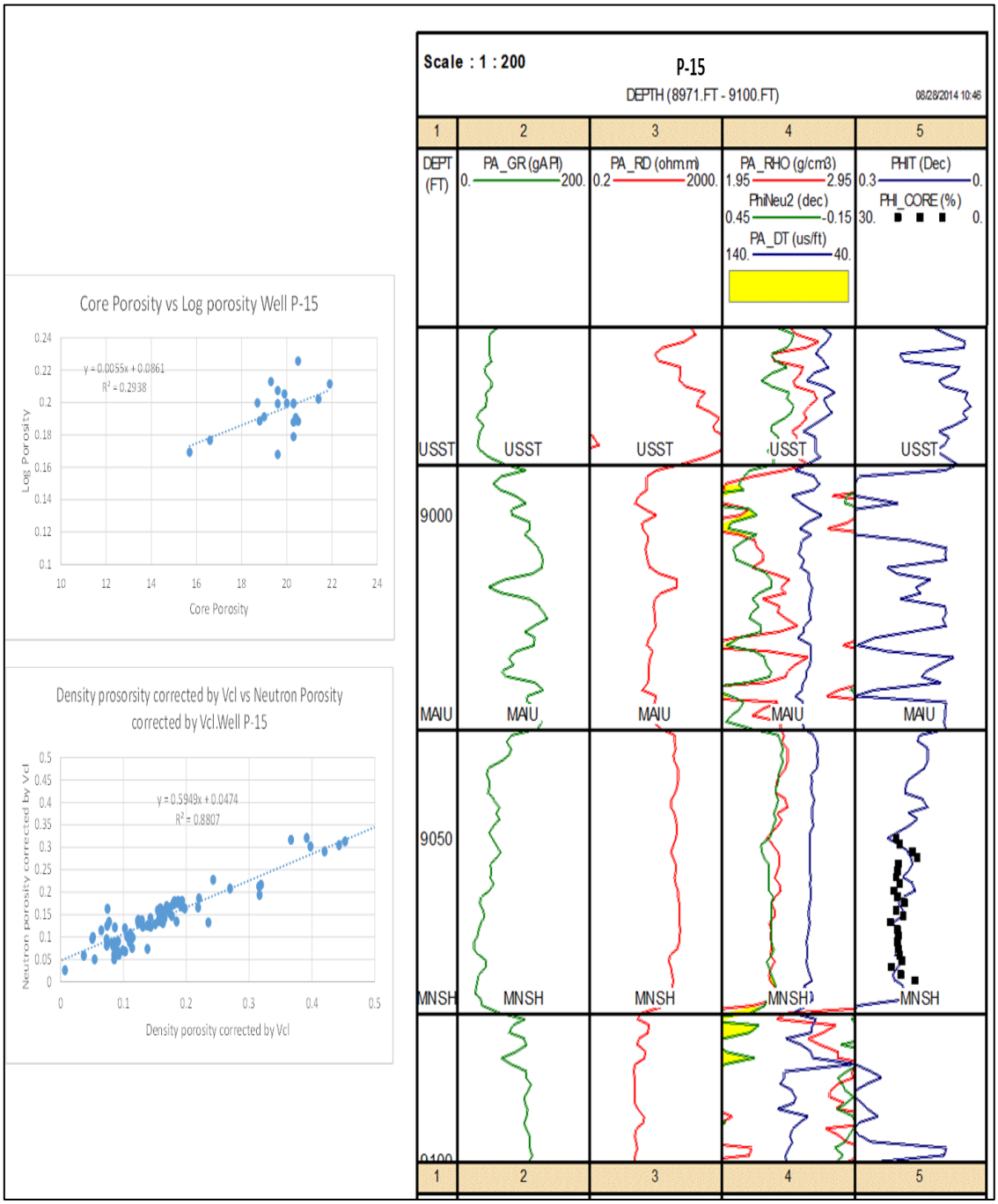

Figure 29. Core porosity vs. log porosity (upper Left). ϕ_D^sh vs. ϕ_D^sh (lower left) and core porosity vs. log porosity in depth (right).

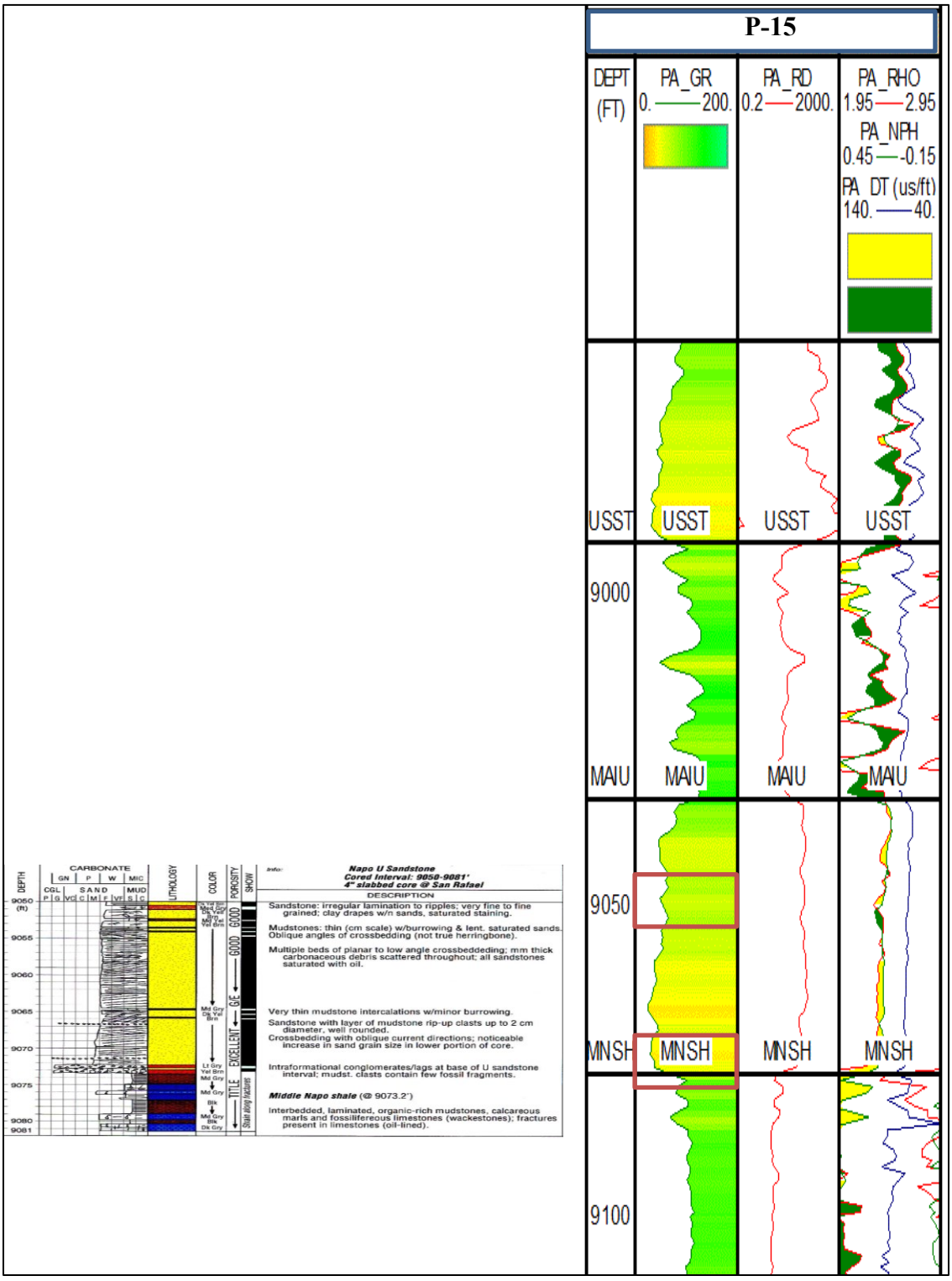

Figure 30. Core data comparison with log data for well P-15. The zones inside the red square are the zones influenced by mud drapes and clast that affect logging tool measurements

The calculation of the water saturation for all the wells in U reservoir was performed using the Dual water equation. The salinity of the reservoir is around 55000 ppm NaCl.

$$\frac{1}{R_t} = \frac{\phi_s^m S_{wt}^n}{a}\left(\frac{1}{R_w} + \frac{S_{wb}}{S_{wt}}\left(\frac{1}{R_{wb}} - \frac{1}{R_w}\right)\right) \quad (46)$$

Where the m, n ,a, Swb are calculated using the same values and equations as Hollin

The term R_{wb} is calculated using a rearrangement of the Archie equation:

$$R_{wb} = \frac{\phi_{sh}^m}{a * R_{sh}} \quad (47)$$

where

R_{wb} is the resistivity of the Clay bound water

R_{sh} is the measurement of deep resistivity in a pure shale zone

ϕ_{sh} is the porosity of clay

Assuming that “m”, “n” and “a” are the same as in sandstone.

There is no water saturation data form core measurements so it is not possible to correlate with the obtained results from well logs.

Rock Physics analysis of U sandstone

Since the mineralogical composition of the Upper U and Main U are very similar to the Hollin composition, the same considerations, assumptions and approaches were used for U reservoir.

Synthetic density logs were created using the equations from 28 to 34 in order to test if the volumetric fraction assumption is corrected. Equation 29 is used in Main U, and equations 30 and 31 are used in Upper U for the calculus of K_s and μ_s. The rest of equations were applied under the same considerations as Hollin using the values from Table 1. The oil gravity from U reservoir is 35.5 API and the reservoir pressure is around 1600 psi.

Figure 31 and 32 are the correlation between real and synthetic density logs from wells C-30 and C-31 in the U reservoir.

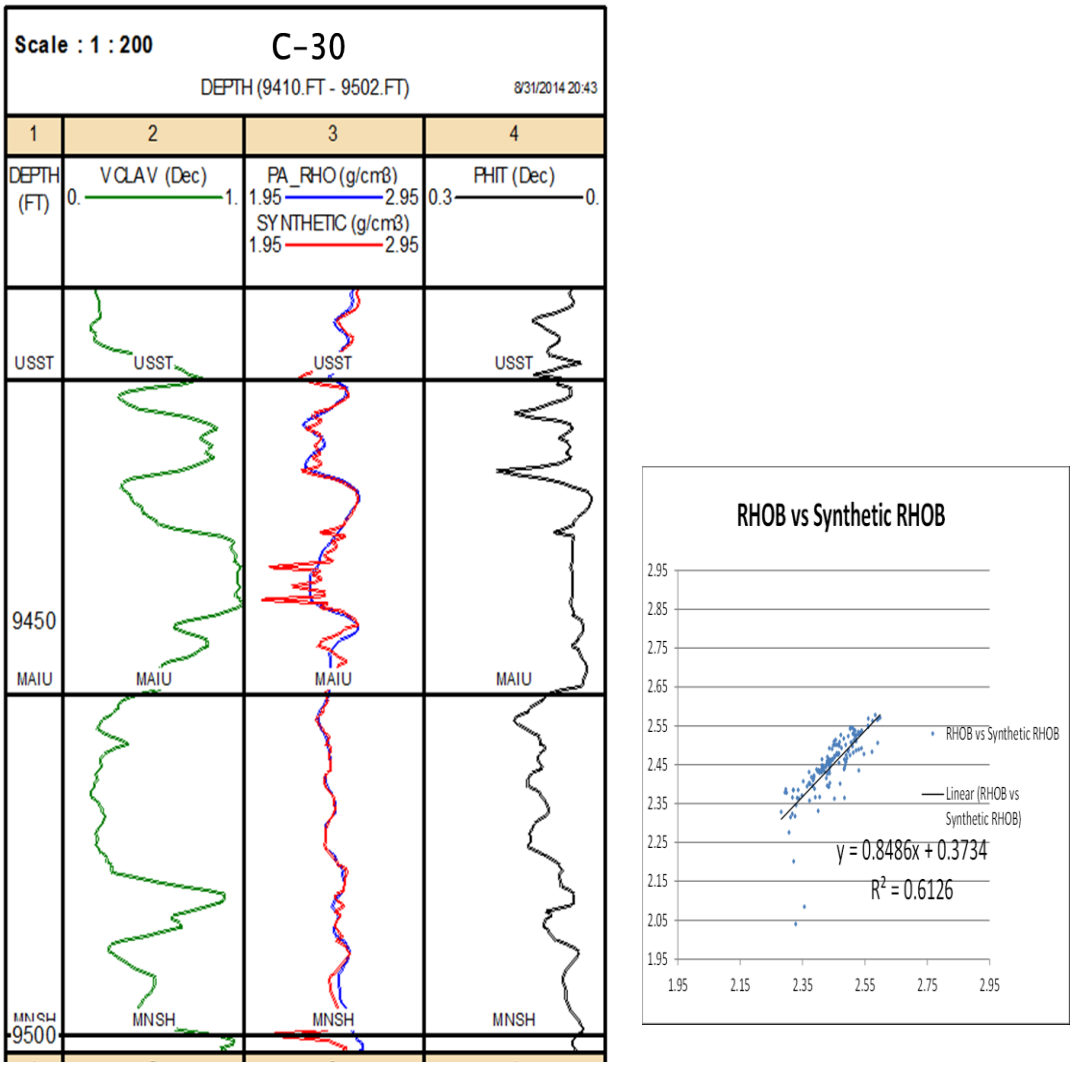

Figure 31.Synthetic density vs. real density log from well C-30.

The Upper U sandstone has high content of clay and shale intercalations. As shale is very heterogeneous, it causes scattering in the cross plot.

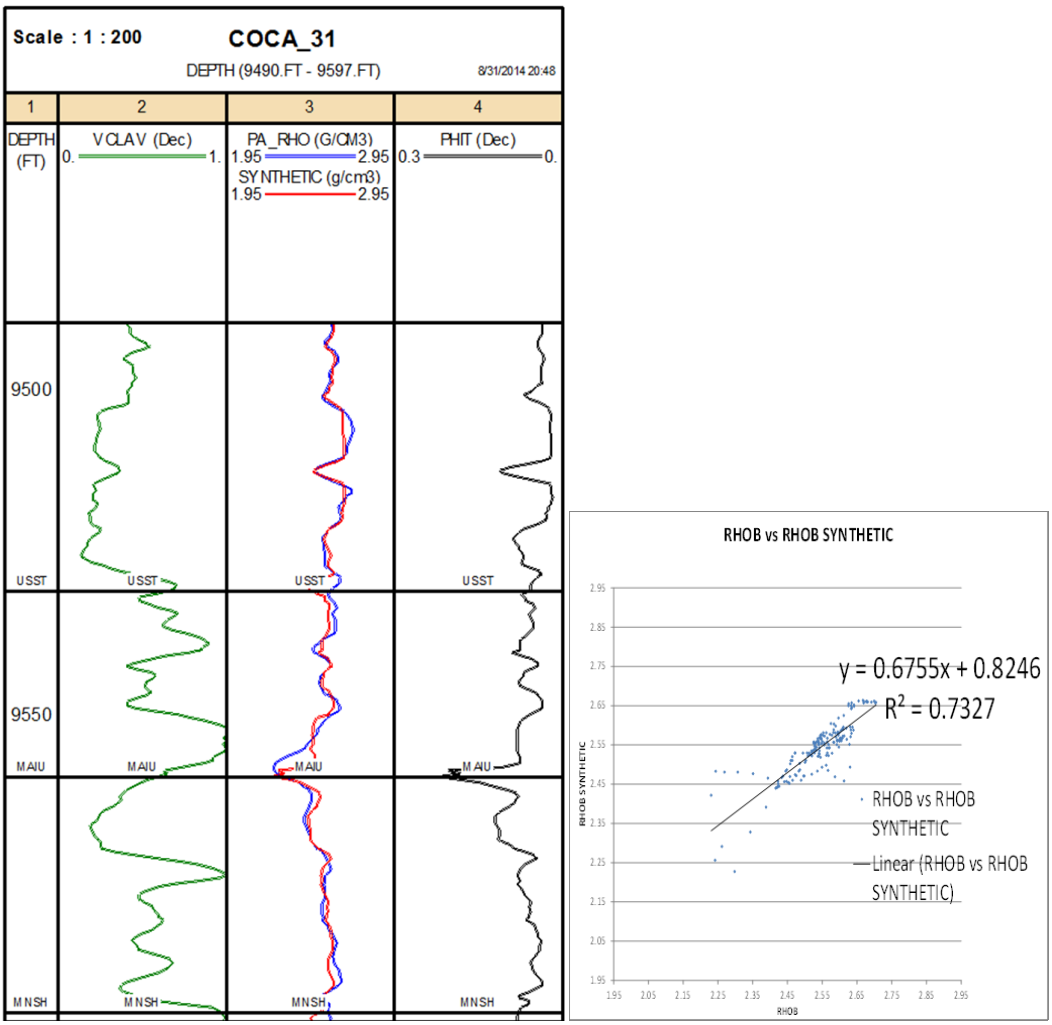

Figure 32. Synthetic density vs. real density log from well C-30

The frame flexibility factor γ_k from Sun, 2000' model is obtained by the application of the previously presented equations from 35 to 44. Equation 37 is used to calculate K_s and μ_s for Main U and for Upper U when the Vcl is lower than 0.4. Equation 38 is used for when Vcl is higher than 0.4. The critical volume of clay of 0.4 was confirmed for U reservoir using the cross plot of *c* ratio vs. Vcl. Figure 33 shows that

scattering of the *c* ratio increases with the increment of the Vcl. The cutt off of 0.4 can be established as a reference point from which the increment of Vcl produces a non-constant relation in the response of the rock compressibility with respect to the shear motion.

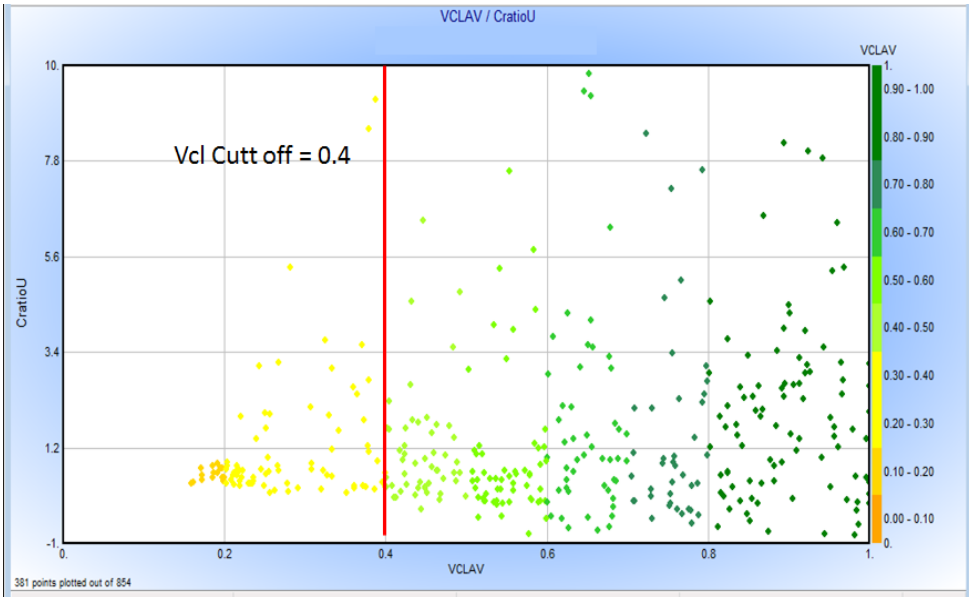

Figure 33. *c* ratio vs.. Vcl from U reservoir. Wells C-30, C-31, C-21 and C-33

The presence of clay produces scattering in the *c* ratio values as it happened in Hollin formation. Again, for the purpose of obtain a S wave synthetic curve, Sun, 2000' model will be more accurate in clean sandstone due to the necessary assumption of a constant *c* ratio. The value of *c* ratio from Upper U is 0.98 as it can be seen in Figure 34. The average *c* ratio for Main U in the clean zones is 0.53 when the Vcl is below 0.4.

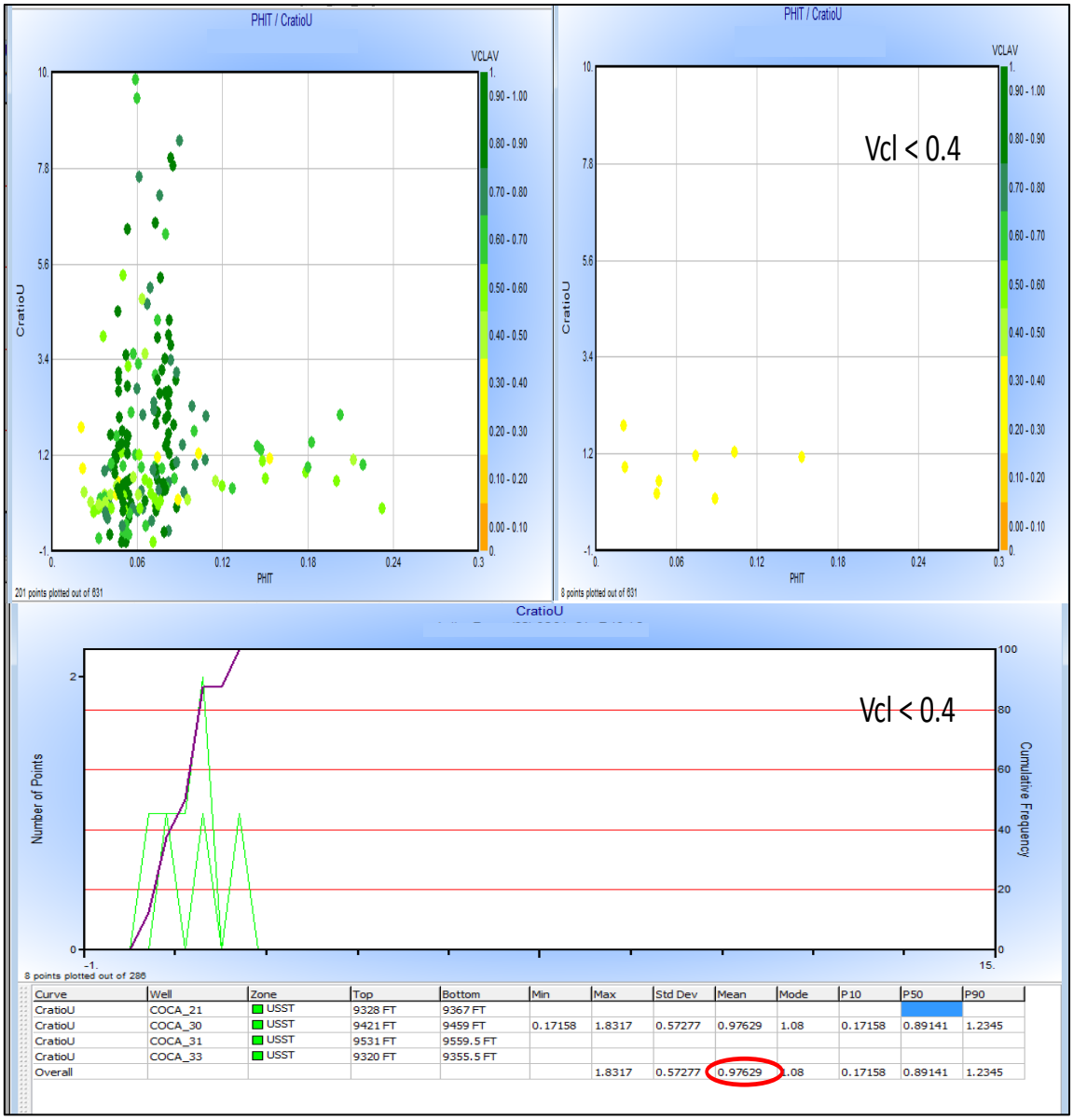

Curve	Well	Zone	Top	Bottom	Min	Max	Std Dev	Mean	Mode	P10	P50	P90
CratioU	COCA_21	USST	9328 FT	9367 FT								
CratioU	COCA_30	USST	9421 FT	9459 FT	0.17158	1.8317	0.57277	0.97629	1.08	0.17158	0.89141	1.2345
CratioU	COCA_31	USST	9531 FT	9559.5 FT								
CratioU	COCA_33	USST	9320 FT	9355.5 FT								
Overall						1.8317	0.57277	0.97629	1.08	0.17158	0.89141	1.2345

Figure 34. *c* ratio calculation for Upper U in zones with Vcl less than 0.4. z axis is Vcl. Wells C-30, C-31, C-21 and C-33

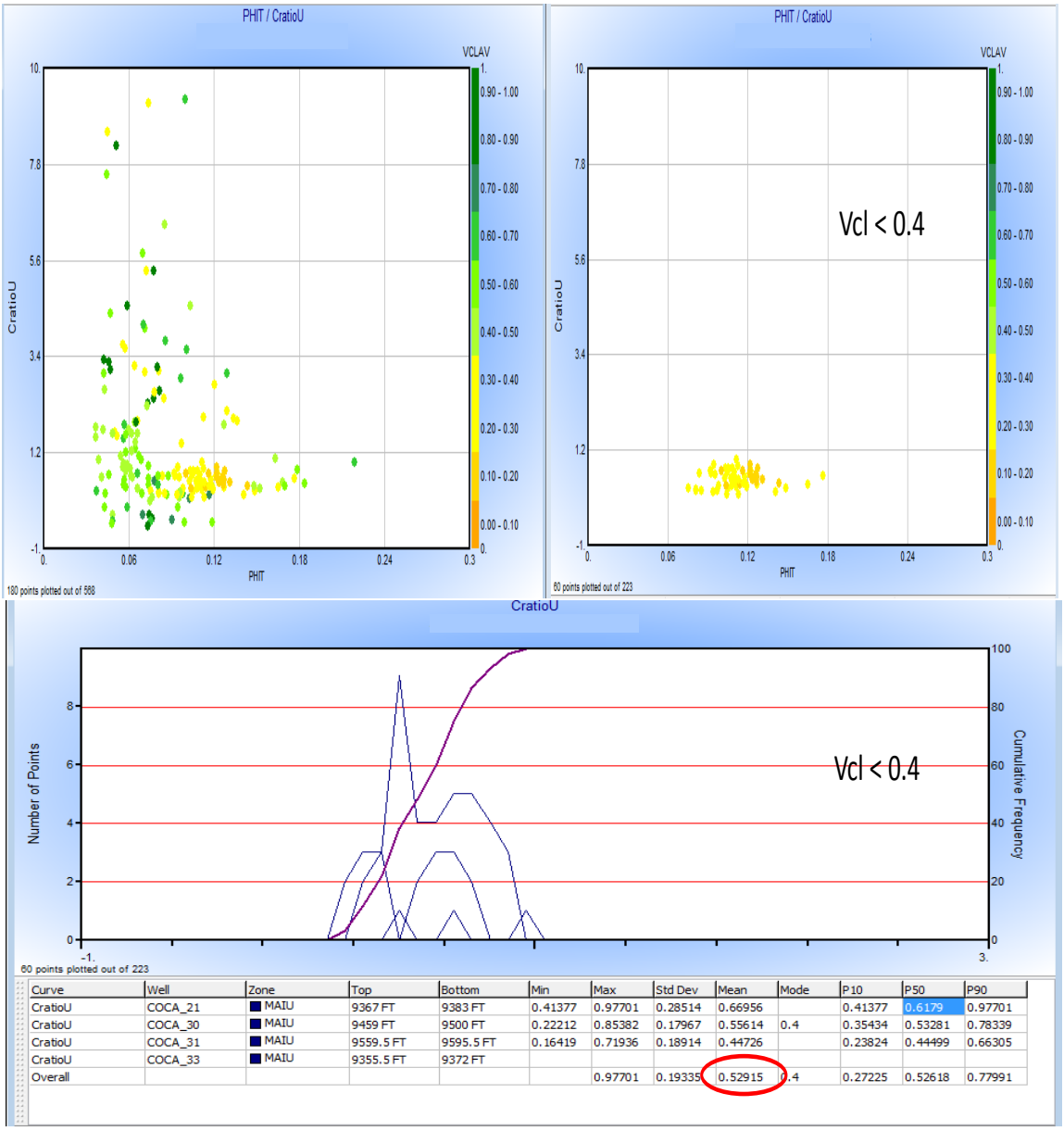

Curve	Well	Zone	Top	Bottom	Min	Max	Std Dev	Mean	Mode	P10	P50	P90
CratioU	COCA_21	MAIU	9367 FT	9383 FT	0.41377	0.97701	0.28514	0.66956		0.41377	0.6179	0.97701
CratioU	COCA_30	MAIU	9459 FT	9500 FT	0.22212	0.85382	0.17967	0.55614	0.4	0.35434	0.53281	0.78339
CratioU	COCA_31	MAIU	9559.5 FT	9595.5 FT	0.16419	0.71936	0.18914	0.44726		0.23824	0.44499	0.66305
CratioU	COCA_33	MAIU	9355.5 FT	9372 FT								
Overall						0.97701	0.19335	0.52915	0.4	0.27225	0.52618	0.77991

Figure 35. *c* ratio calculation for Main U in zones with Vcl less than 0.4. Z axis is Vcl. Wells C-30, C-31, C-21 and C-33

It can be concluded that under the assumption of a constant *c* ratio is mandatory to invert porosity and frame flexibility factor from inversion results, porosity will be

more accurate in the clean zones. Besides, the clean zones represent the shoreface bars in Upper U and the tidal bars in Main U; both of them are restricted to some areas of the oilfield. There are no wells with S -wave sonic log in the south part of the oilfield. Therefore, synthetic curves was created for the U sandstone in wells P-14 and P-15 using equation 45 and the *c* ratio values found before for clean zones . For the zones with a Vcl higher than 0.4 in U sandstone as well as for the rest of the complete sequences, empirical relations from Greenberg and Castagna, 1992 were used to create the S wave synthetic curves.

The wells P-14 and P-15 were used in the well-seismic tie and wavelet estimation for the seismic inversion. Figure 36 is the cross plot of the real S wave curve vs. Synthetic S wave curve for the whole section for wells C-30, C-31 and C-21. Some scattering is present in Well C-21 because washouts that are present in M1 and M2 Limestone. The high correlation coefficient will give a confidence of the quality of the synthetic S wave log.

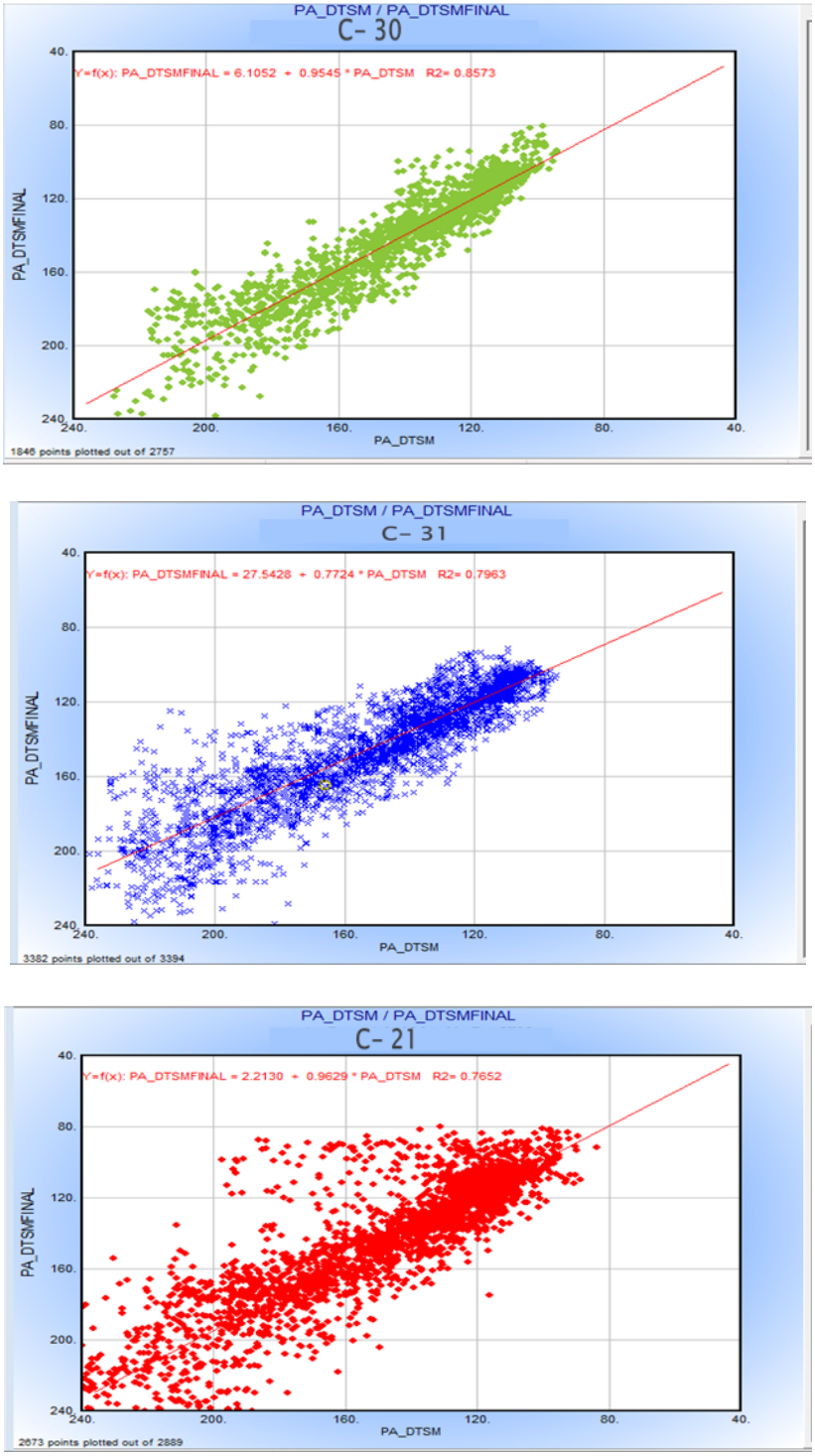

Figure 36. Real S wave log vs.. Synthetic S wave log

Feasibility of the project for U sandstone

U sandstone is located between the A Limestone and the Main Napo Shale (MNSH), (Figure 27). A limestone is overlying U sandstone, and U sandstone is overlying MNSH. The rock physics analysis was performed only for the U sandstone since the mineralogical composition and petro physical properties was known for this zone and not for A Limestone neither for MNSH. The discrimination of U sandstone from A limestone and MNSH using any elastic parameter is a prior mandatory step before the inversion of porosity and frame flexibility factor using Sun, 2000's model.

Upper U is shaly sandstone that in most of the oilfield presents low quality reservoir characteristics. Because of the high content of clay in this sandstone, the elastic response of Upper U is confused with the underlying MNSH in zones where the Main U pinches out. Try to discriminate the whole U sandstone from the underlying and overlying beds is not possible using only the Vcl discrimnator. Therefore, a reservoir quality parameter will be used to discriminate reservoir from non-reservoir. Reservoir facies will be considered in zones where the Vcl is less than 40%, the ϕ is higher than 8 %. Figure 37 shows the cross plot of S-Impedance vs. poisson ratio and the z axis is the reservoir discriminator in which red is reservoir and blue is non-reservoir. Also, the same plot from well logs filtered to seismic frequency (7-50 Hz) is shown. This plot shows that it will be possible to discriminate reservoir zones at seismic frequency (0-50Hz) but this must be confirmed after inversion when pseudo logs will be extracted from inversion results.

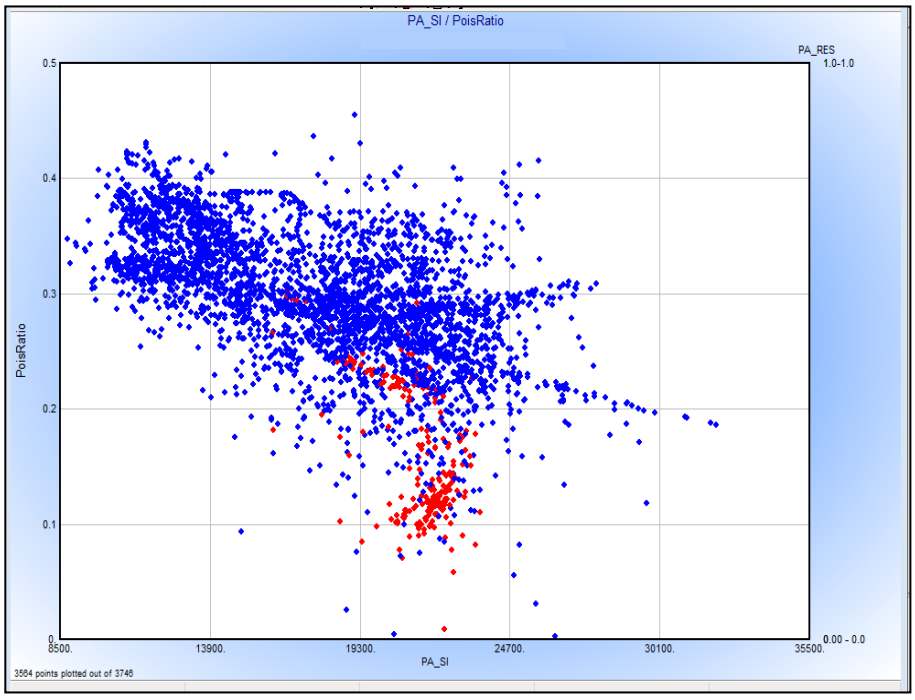

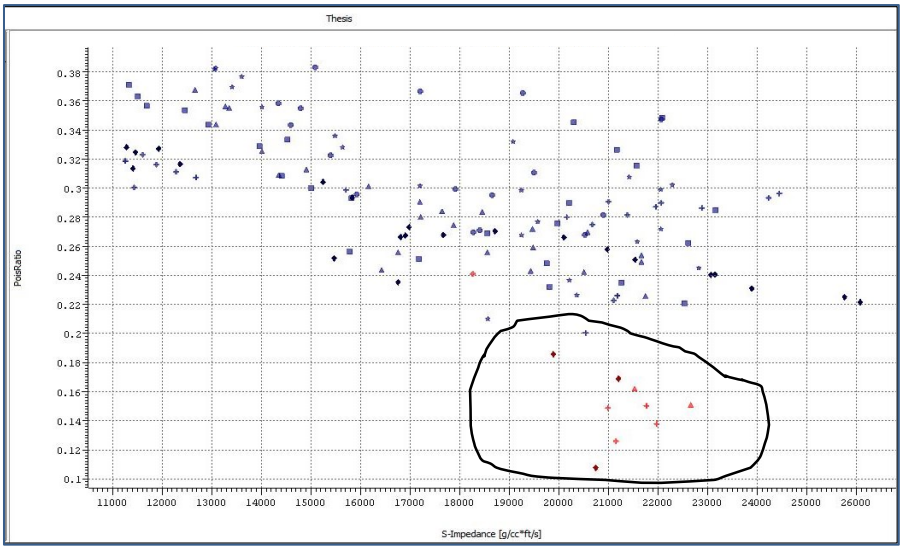

Figure 37. Cross plot of poisson ratio vs.. S –Impedance at well log frequency (upper) and at seismic frequency (lower) Wells C-21, C-30, C-31, C-33, P-14 and P-15

Applying Sun, 2000's model, the frame flexibility factor γ_k is obtained. From Figure 38, that is the cross plot of P-Impedance vs. Vcl and γ_k in z axis can be inferred that values of γ_k lower than 2 approximately represent shale (Vcl > 0.6). This facies will be named as Type I. On the other hand, values higher than 2 represent shaly and clean sandstone. It is needed to refine this classification based on the γ_k values. To accomplish this objective the crossplot of P-Impedance vs. porosity is used, (Figure 39). The upper plot has the γ_k in the z axis. And the lower one has the Vcl in z axis. From these two plots, it is determined that facies with the highest porosity have γ_k values between 2 and 6. These facies will be named as Type II facies. Also, Type III facies with low Vcl and low porosity are located in the interval from 6 to 8. Finally, shaly sandstones with Vcl values between 0.4 and 0.6 presents a γ_k values higher than 8. These facies will be classified as Type IV.

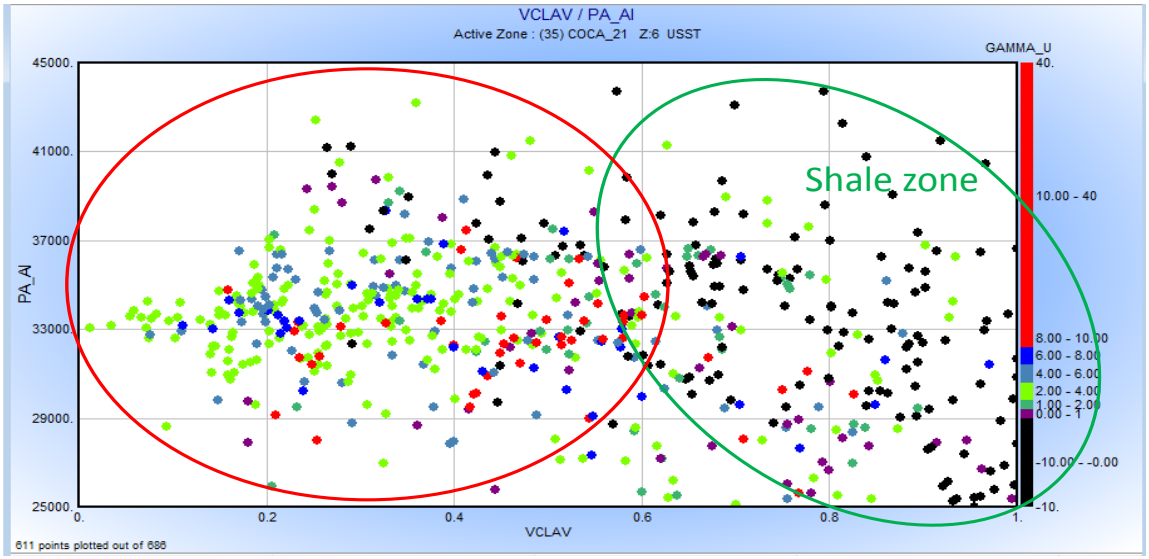

Figure 38. Cross plot of P-Impedance vs.. Vcl with γk in the z axis Upper U and Main U

The relationship between porosity and γ_k and relationship between Vcl and γ_k are not direct. There is a complexity in the nature of the γ_k since this factor responds not only to one parameter. Grain size, sorting, inclusions, Vcl and porosity are factors that influence the value of γ_k.

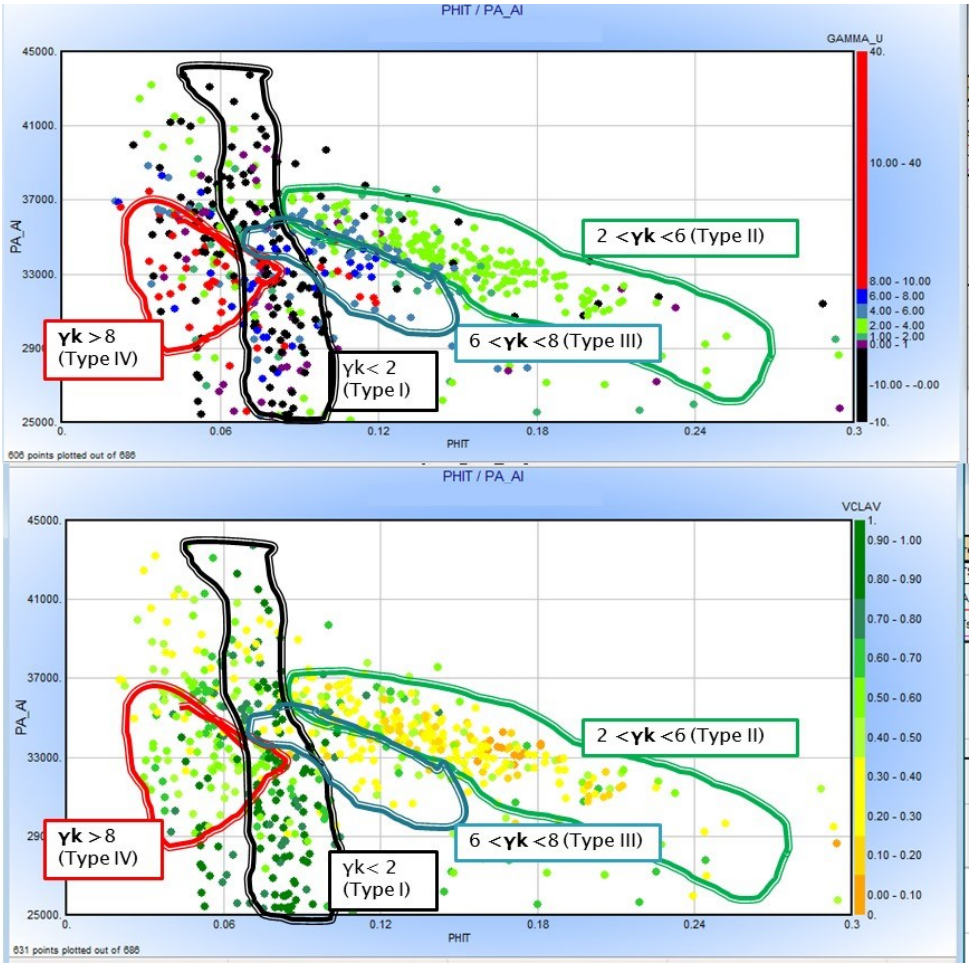

Figure 39. Cross plot of P-Impedance vs.. Vcl with γk in the z axis Upper U and Main U

Based on the descriptions of core from well P-15, a qualitative analysis of the γ_k is performed. The core from P-15 was taken from the clean zone in main U (Figure 30),

so in order to refine the analysis, the cut off of Vcl less than 0.4 was applied. The figure 40 is the core facies description related to grain size and sorting associated to the distribution of the *K,* and μ. γ_k values from 2 to 6 and high porosity values represent the most prolific facies, (Type II). Tidal bars and shoreface bars with a grain size from fine to medium and fair to well sorting are characterized in this interval. Values of γ_k from 6 to 8 represent very fine to fine clean sandstone with well sorting, (Type III). Very fine to fine grain size with mud drapes and in some cases slighly carbonate cement are the facies represented by values of γ_k higher than 8, (Type IV). And according to *K* values and μ values, there is a zone that represents very fine grain sandstones with bad sorting. It shows very low porosity and higher impedance values with a similar behavior as shale.

Grain size is intrinsically relate to the compressibility of the rock since big grains produced big pores and big pore throats in sandstones. Consequently, the rock is less compacted. On the other hand, the irregularity in grains size produces more contact between grains and more resistance to shear motion; hence, μ value is higher.

Additional to porosity volume inversion, the rock physics analysis results will allow to stablish facies distribution based on the γ_k values. Also, from porosity and γ_k values, it will be possible to discriminate reservoir zones in a more reliable way.

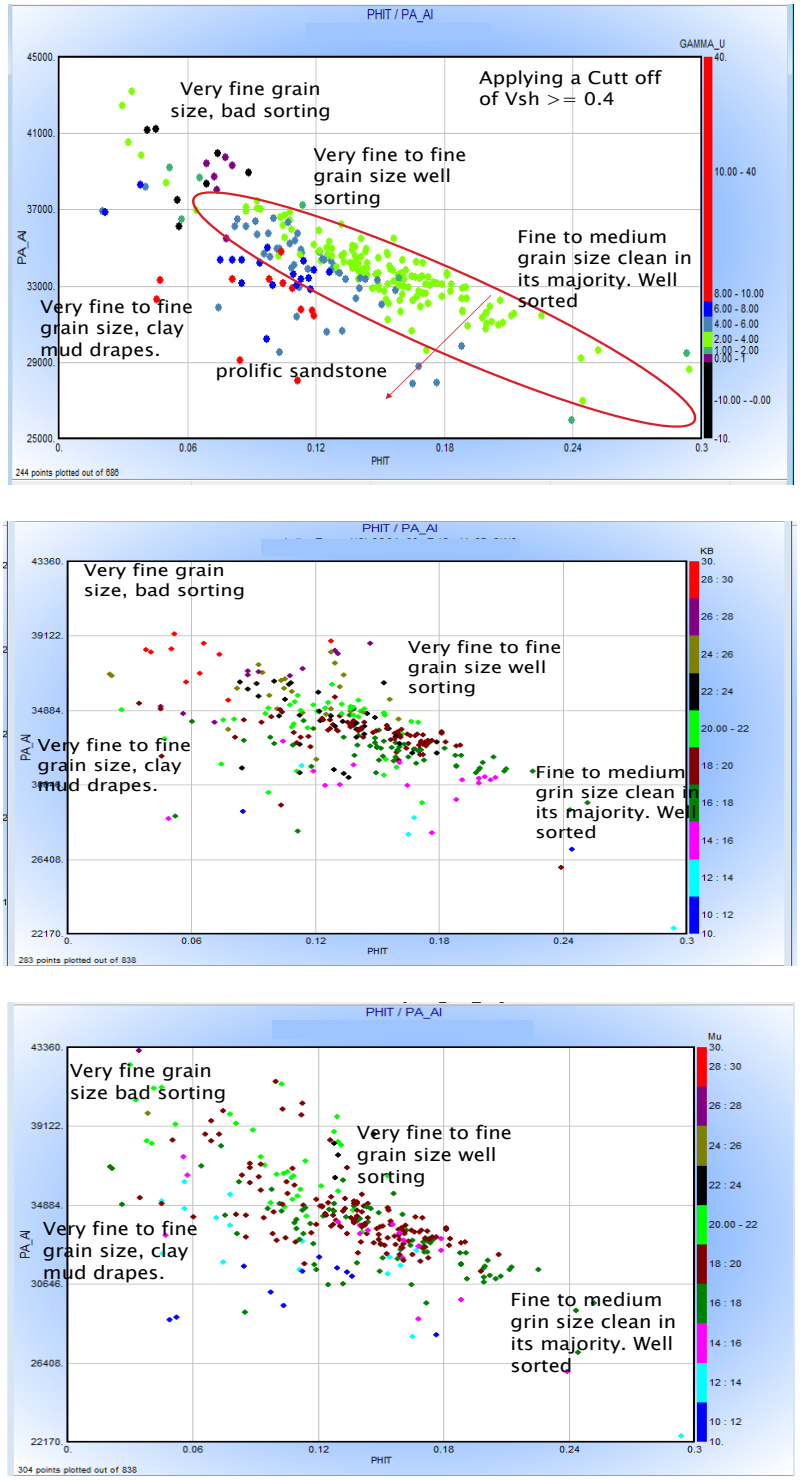

Figure 40. Cross plot of P-Impedance vs.. Porosity with γk, K and μ values in z axis. Comparison of values of γk, K and μ with core descriptions.

4. SEISMIC INVERSION FOR U RESERVOIR

Analysis of seismic data

Frequency and phase

For any inversion process it is needed to analyze the quality of the seismic data; if its frequency content and phase are constant along the whole survey or not. Change in frequency content or phase will produce a problem in the well-seismic tie, in the estimation of the wavelet and consequently in the horizon interpretation.

Four partial angle-gather stacks that have ranges from 4º-14º, 12º -22º, 20º-30º and 28º-40 º was used in the inversion process. Analysis of the frequency content and amplitude spectrum of the seismic data showed that there is a difference in some zones of the seismic survey. Especially at the north of the seismic volume, the frequency content is reduced for the four angle gather stacks as shown in Figure 26. This reduction is more severe in the 4-14º and in the 12-20º angle gather stacks. The reduction of the frequency content could be endorsed to some acquisition problem since it is a localized problem that increases with depth. Near angle gather stack is more affected at the northern area probably because of the presence of noise.

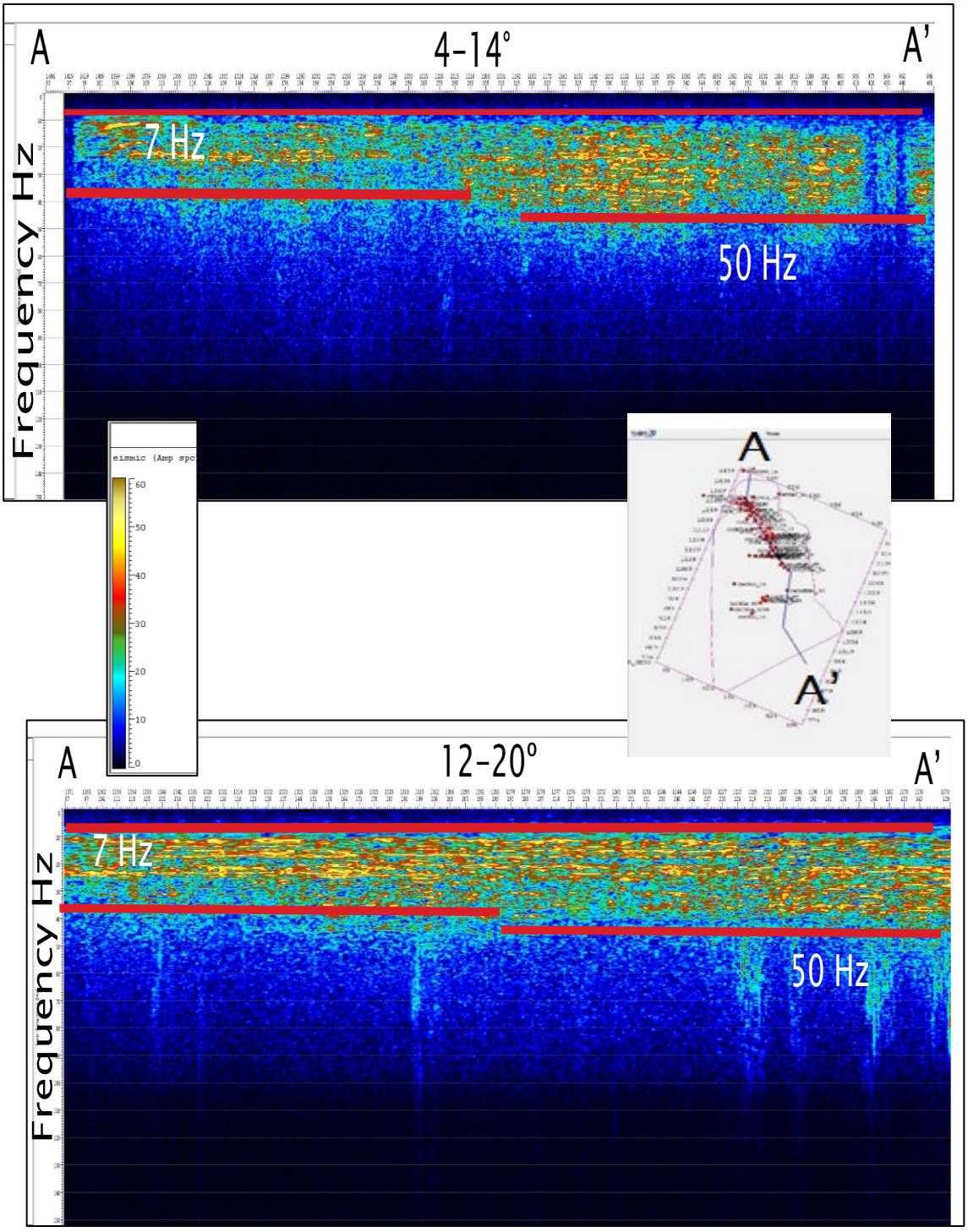

Figure 41. Frequency content of the four angle gathers stacks

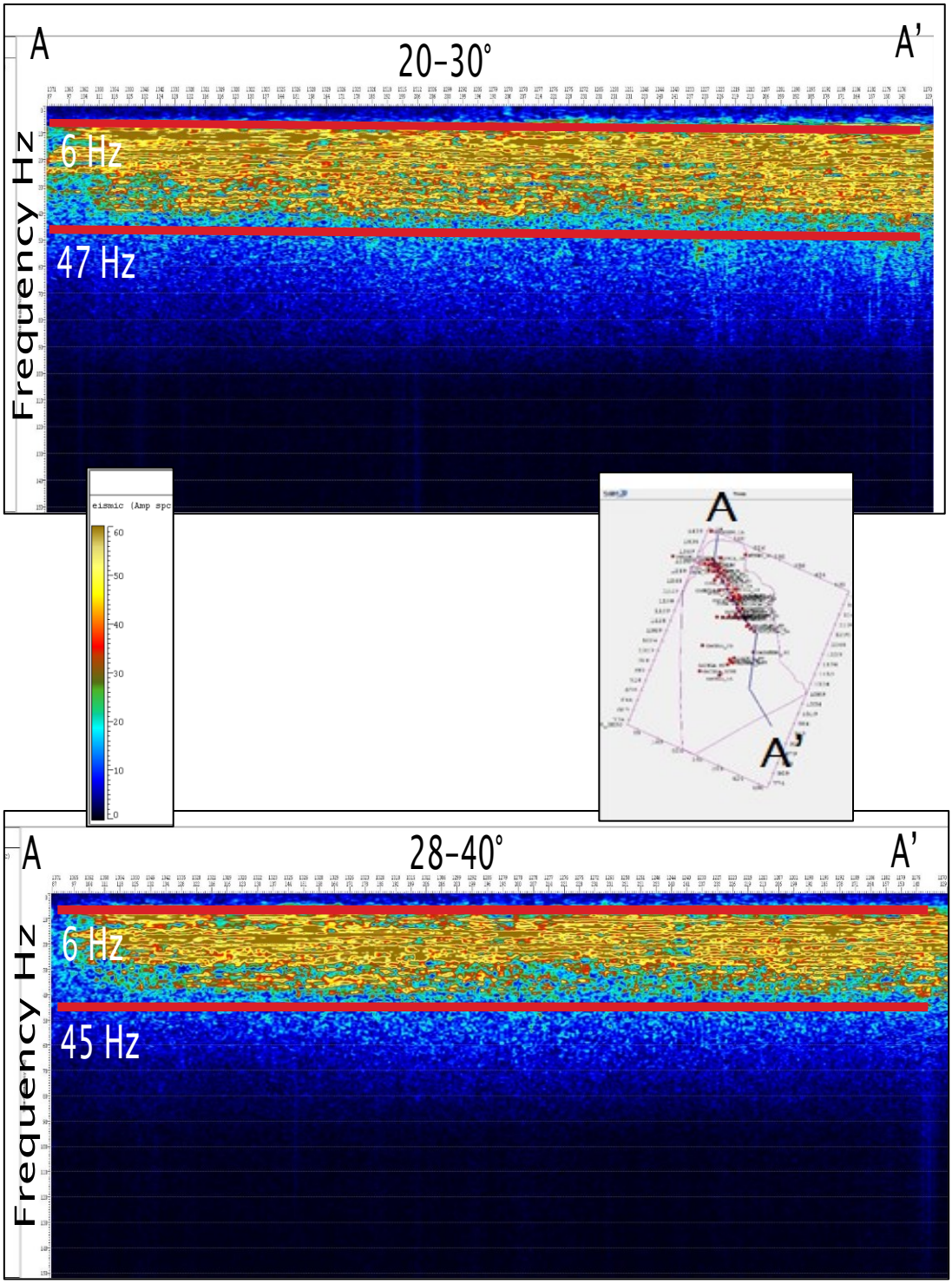

Figure 41. Continued

As a consequence of this difference in frequency content, it is expected that a lateral and vertical variation of the wavelet exists. Figure 41 shows a tentative low and high frequency limits of the spectrum for each angle-gather stacks; these limits will be used then in the merging with low frequency model created by the interpolation from well log data.

In the same zones where the frequency content is reduced, a change in phase become more severe around 1900 ms. Three horizons were interpreted in the full stack volume using the well C-21 to tie to seismic since it has a check shot. Horizons will be used as a trend guide for the interpolation of the low frequency model from well logs. Figure 42 shows the cross section of the seismic data for the full stacked volume and for the four angle gather stacks. The cyan horizon is interpreted as the top of the A limestone, the green horizon represents the MNSH formation and the purple one is LNSH formation. The change in phase causes that the LNSH interpreted horizons must shift rapidly from a pick in the south area of seismic volume to a trough in the northern.

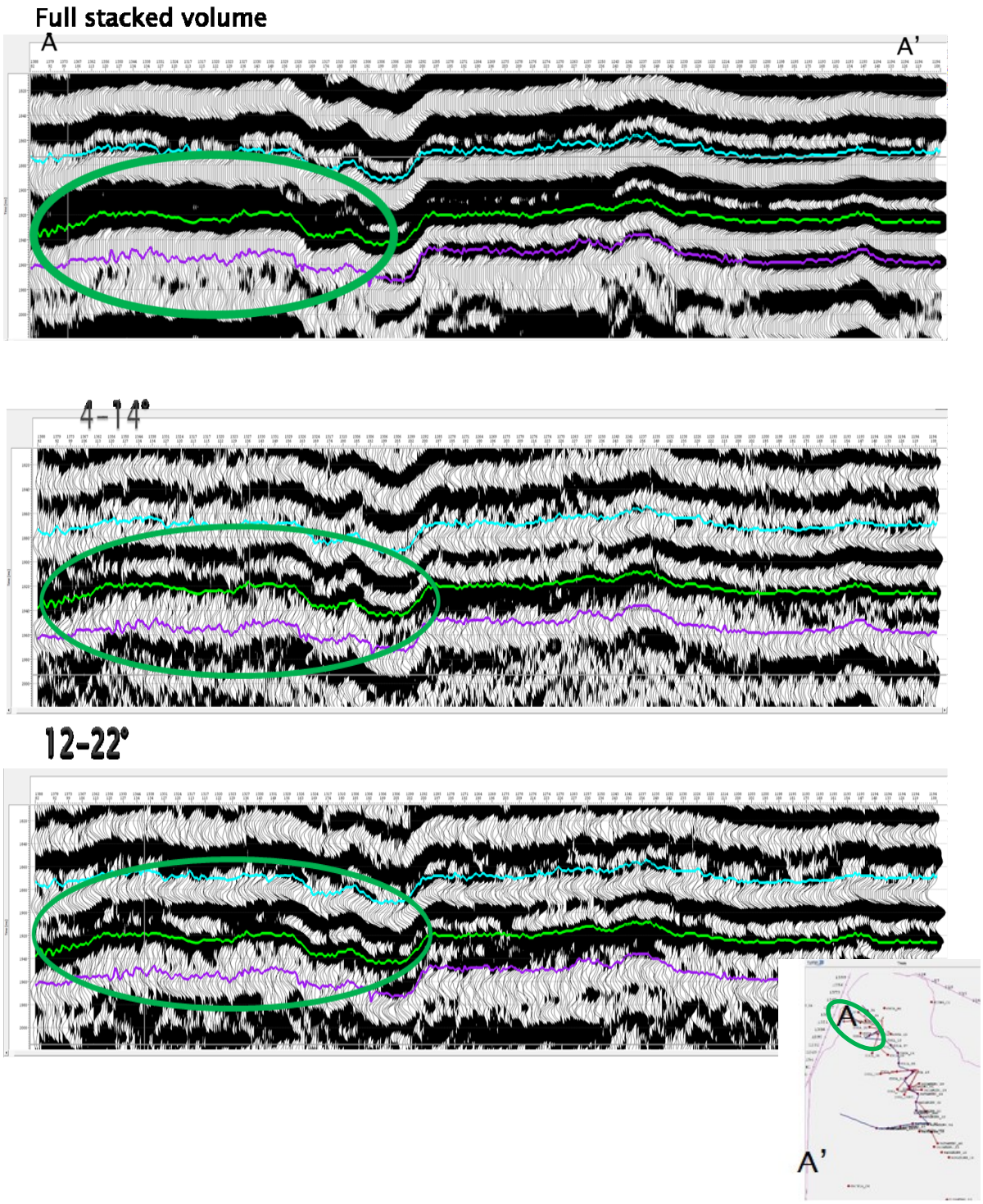

Figure 42. Phase change and horizon interpretations

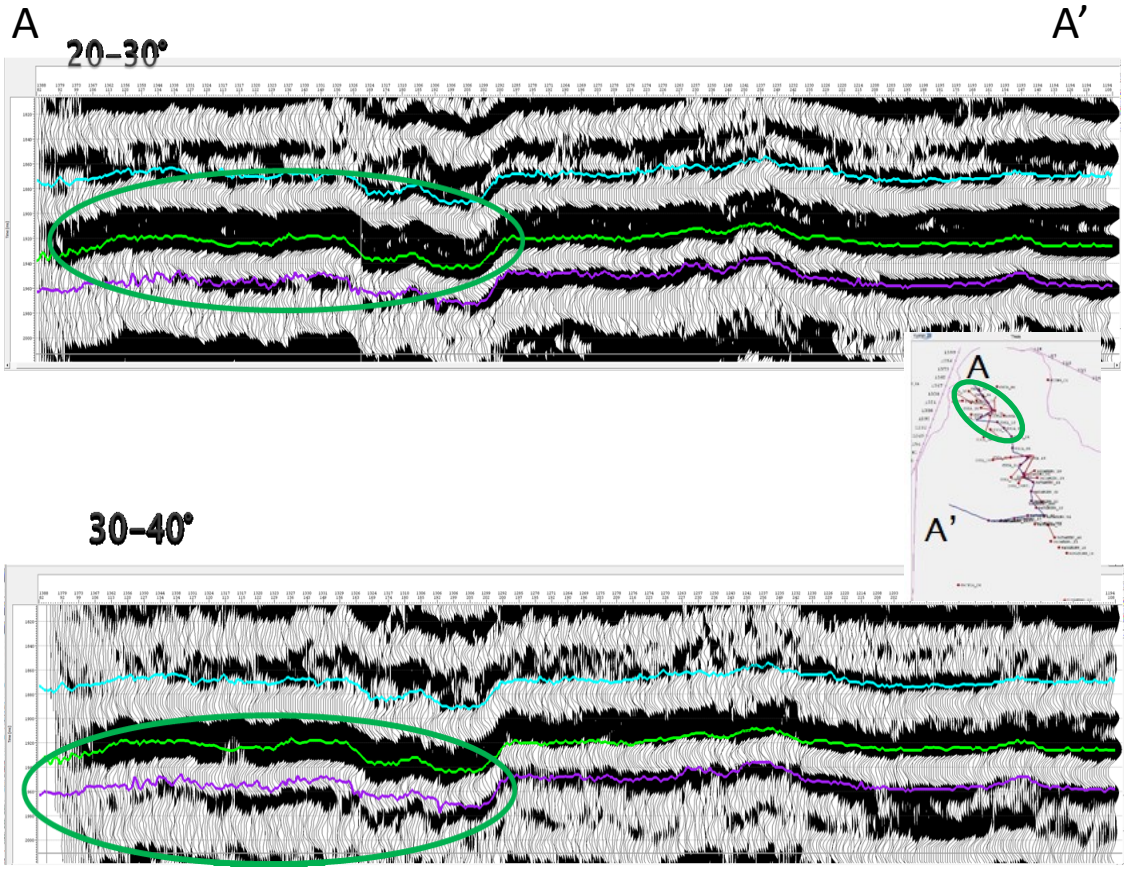

Figure 42. Continued

Analysis of the number of angle stacks needed for the inversion

It is necessary to find the optimum number of angle stacks to be used in the inversion. The reflectivity behavior with respect to the incident angle was tested for the four angle gather stacks. The AVO effect produced by the interfaces between A Limestone and U sandstone and the interface between U sandstone and MNSH was

analyzed. The main concern is to define if the use of the 30-40 º will improve the results or not.

Figure 43 and 44 are the reflectivity variation vs. the incident angle for two wells located at the south and the north of the oilfield respectively. Full Zoeppritz equations are applied for compressional reflection coefficient and to the converted compressional wave. These two wells are located in two different zones. At the north, where the tidal bars from Main U pinches out, well C-30 is used, and well P-15 is used at the south in the zones of tidal bars presence.

Between 25-35º tidal bars in the south of the oilfield produce the highest change in converted wave reflectivity interface between A limestone and U sandstone as it is shown in figure 43. Compressional wave reflectivity from well P-15 do not show a big change at far angle stacks in the A limestone-U sandstone interface. However, at 35º the variability of P+P- and S+S- is higher than at 25º. For the interface between U sandstone and MNSH, the change in P+P- reflectivity is higher at 35º than 25º, but the variation of P+S- is not significant between these two angles.

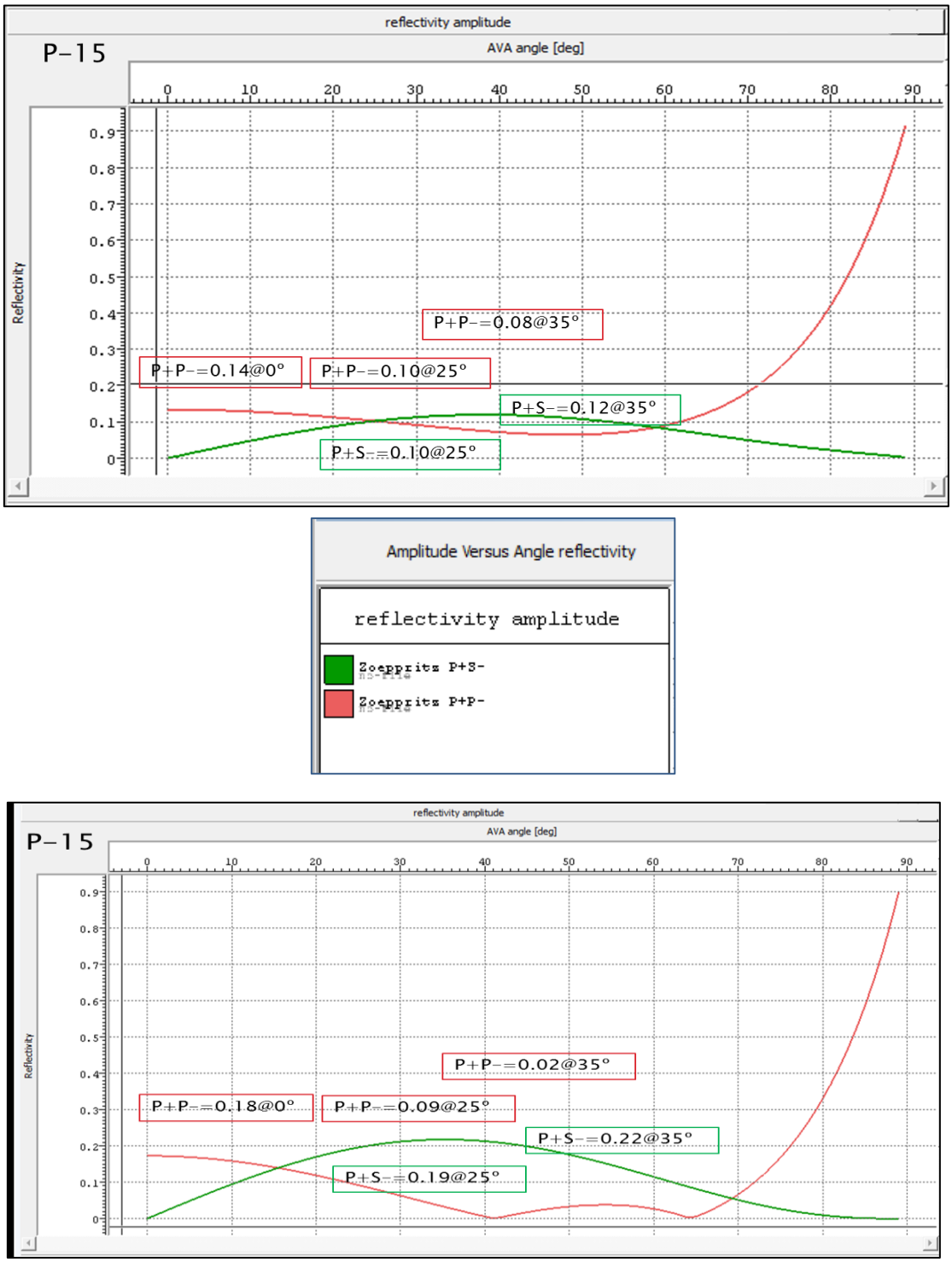

Figure 43. Reflectivity vs.. incident angle from well P-15. A limestone-U sandstone interface (Upper plot). U sandstone-MNSH interface (lower part).

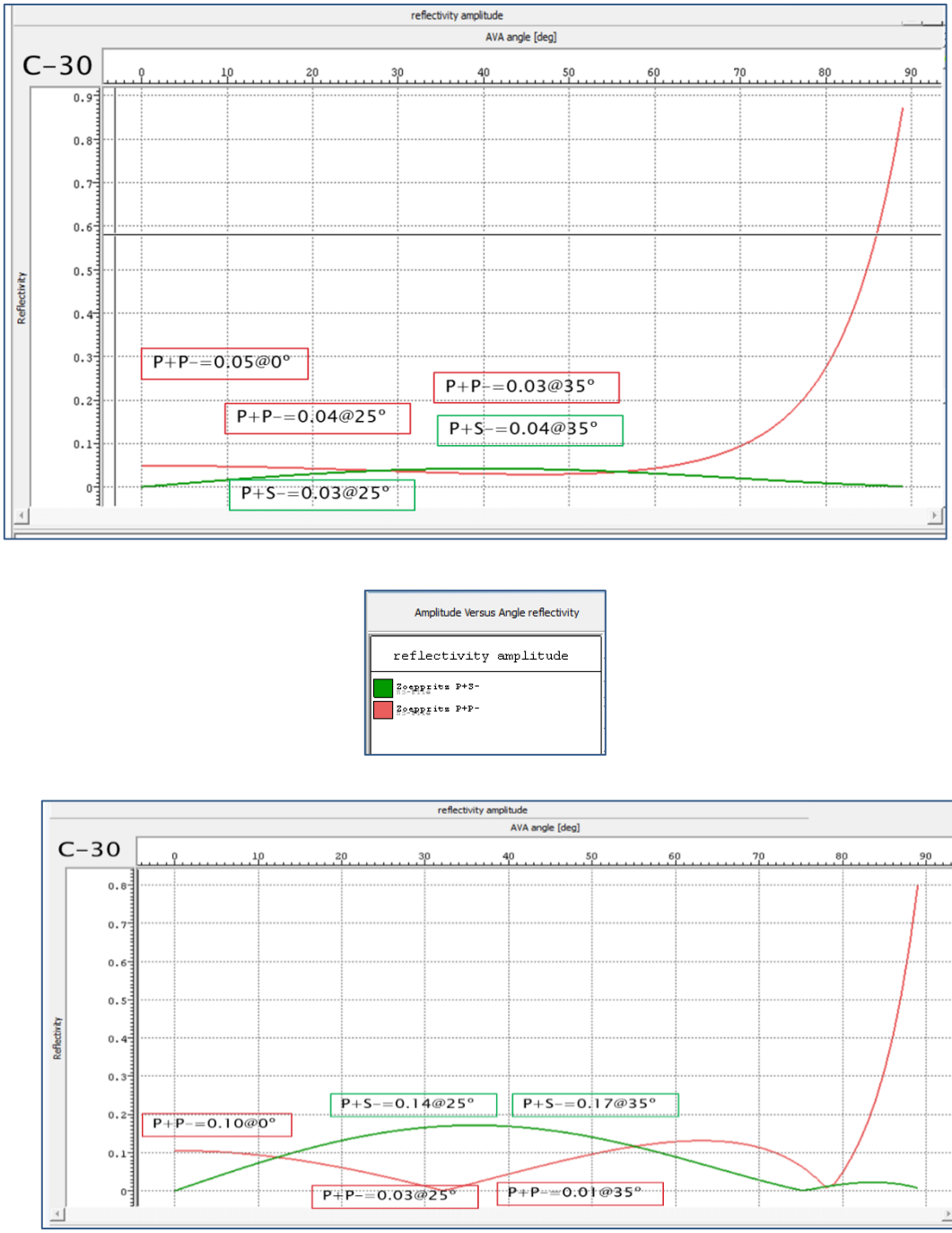

Figure 44. Reflectivity vs.. incident angle from well C-30. A limestone-U sandstone interface (Upper plot). U sandstone-MNSH interface (Lower part).

Figure 44 shows the reflectivity variation vs. incident angle for the interface between A Limestone and U sandstone for well C-30 located in the zone where main tidal bar of Main U pinches out. Neither P+P- reflectivity nor P+S- show a high variation at far offsets. Interface between U sandstone and MNSH presents moderate variation in P+P- and P+S- reflectivity from 25º to 35º.

From all the observations made above, it can be inferred that some advantage in the differentiation of U sand from A limestone and MNSH can be obtained by the use of the 30-40º angle gather stack; however, inversion results will be tested with three and four angle gather stacks. Because the problems of phase variability and reduction in frequency, it is difficult to determine if there is an advantage or disadvantage for using the fourth stack. Third stack shows misalignment and a strong variation in phase in different zones; hence, forth stack could help to add some information missed in third angle gather stack.

Well- seismic tie and wavelet estimation

This is the one of the key steps for the inversion process since the accuracy of the wavelet estimation is directly proportional to the accuracy of the Inversion results. The estimation of the wavelet was done for the four stacks using the wells, C-30, C-31, C-33, C-21, P-14 and P-15. Lateral variation of frequency content and phase causes that different wavelets were extracted at different zones. The followed workflow is summarized in figure 45.

First, statistical wavelet estimation from seismic data is performed. Due to the lateral variation of seismic characteristics, the estimation must be done in the surrounded area of all used wells. Then, the model drive wavelet estimation methodoogy was applied for all wells. After the first estimation of the wavelet, quality control is applied. If the estimated wavelet does not meet the quality control parameters, vertical alignment, stretched and squeeze is performed in order to improve the well-seismic tie. Besides, wavelet parameters such as, wavelet length and maximum frequency are redefined in order to improve the quality control parameters.

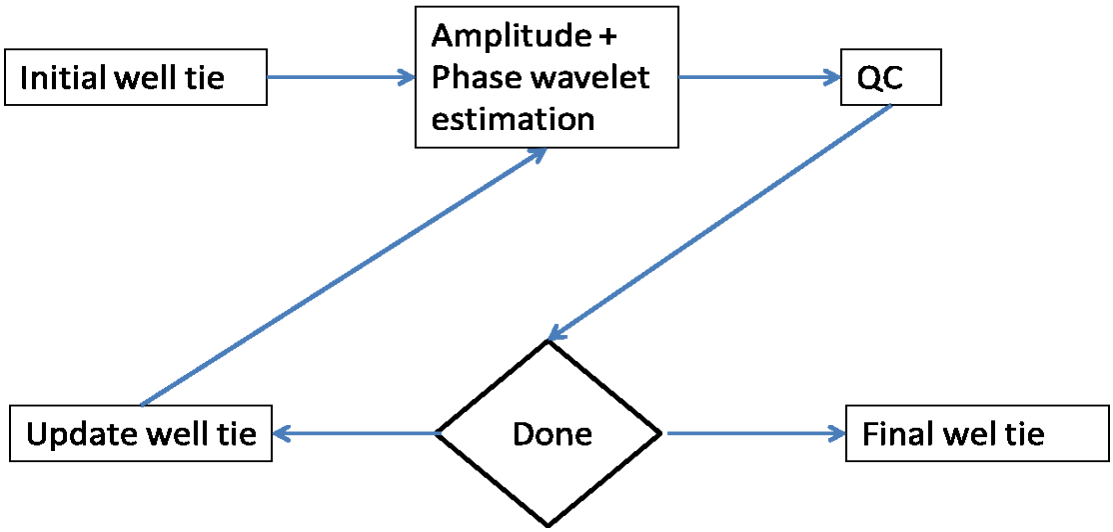

Figure 45. Work flow for the model driven wavelet estimation.

The main quality control parameters used to test the accuracy of the extracted wavelet are described below.

- Synthetics – seismic correlation that depends directly from the alignment of peaks and troughs.
- Correlation the P-Impedance value from wells to the P impedance inverted from the traces around the well
- The matching of amplitude spectrum of the seismic with amplitude spectrum of the wavelet
- The matching of amplitude spectrum of the inverted reflectivity with the amplitude spectrum of the well log reflectivity data at the seismic bandwidth

Figure 46 and 47 show the wavelet estimation of the wells C-30 and P-14 for the four angle stacks. In the second track from right to left, it is plotted the T-D relationship (green), the slowness drift that is the difference between the ratio of TD to sonic log (red) and the slowness curve (black). The slowness curve and the T-D relationship keep the same scale. The ratio of T-D to sonic log must be around 1. In the first track from the right to the left, the P-Impedance well log (blue) is plotted and T-D relationship (black). In the amplitude spectrum plot at the left lower part of figure, the red color line represents the seismic spectrum, the magenta color line is the final extracted wavelet spectrum, the green line is the well log reflectivity spectrum, the blue line is the inverted reflectivity spectrum and the cyan line is the residual between the well log reflectivity and the inverted reflectivity. The plot at the right side of the amplitude spectrum is the comparison between the amplitude spectrum of the seismic data (green) and the

extracted wavelet one (red) and finally, at the left lower part of the plot is the estimated wavelet and its phase.

After performing the wavelet extraction, it is concluded that lateral and vertical variation of the wavelet is an important imprint from the seismic acquisition. Wavelets at south part of the zone have lower average length than the wavelets in the north part. Besides, change in phase is evident between the north and south areas with a zone of transition. All of these facts confirm the lower frequency content of the north part and consequently its lower resolution. Figure 48 is the T-D relations for the 6 wells refined after the wavelet extraction. Consistency of this T-D relations was achieved.

Wavelets present similar characteristics according to the proximity of the analyzed wells. Wavelets from wells P-14 and P-15 that are located at the south of the oilfield, present similar characteristics for the four angle gather stacks. C-31, C-33 and C-21 locate at the north of the studied zone show similar characteristics among them. Well C-30 presents a big difference with respect to the other wells. Since well C-30 does not have a caliper measurement log, it cannot be concluded that the problem is caused only by bad well log measurements or because of some problems in the seismic data. Figure 49 shows the estimated wavelets for all wells and for the four angle gather stacks.

Based on this observations and conclusions, interpolation wavelet volume was created using all the wavelets except that one from well C-30.

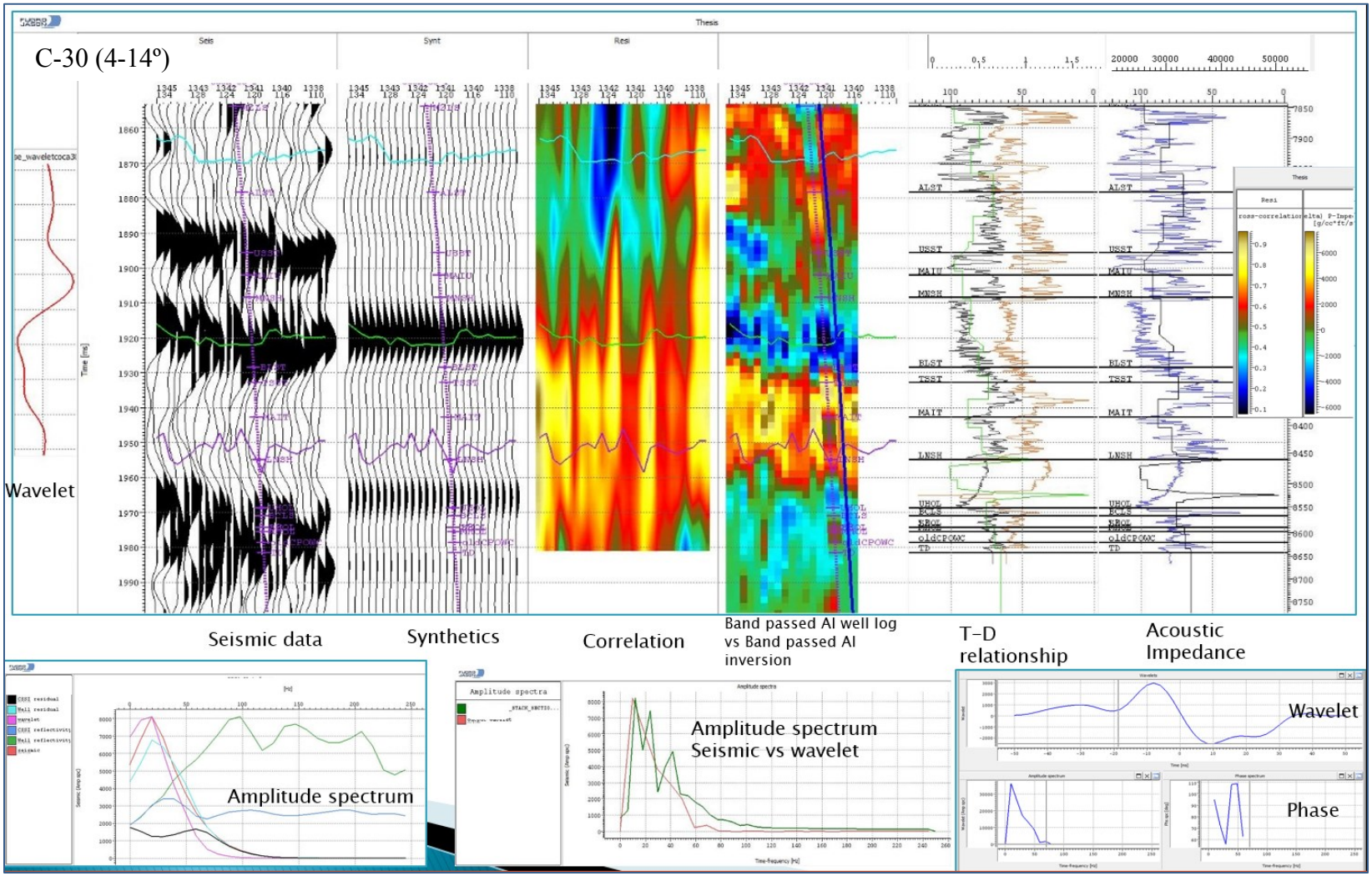

Figure 46. Well C-30. Wavelet extraction (see explanations in the text)

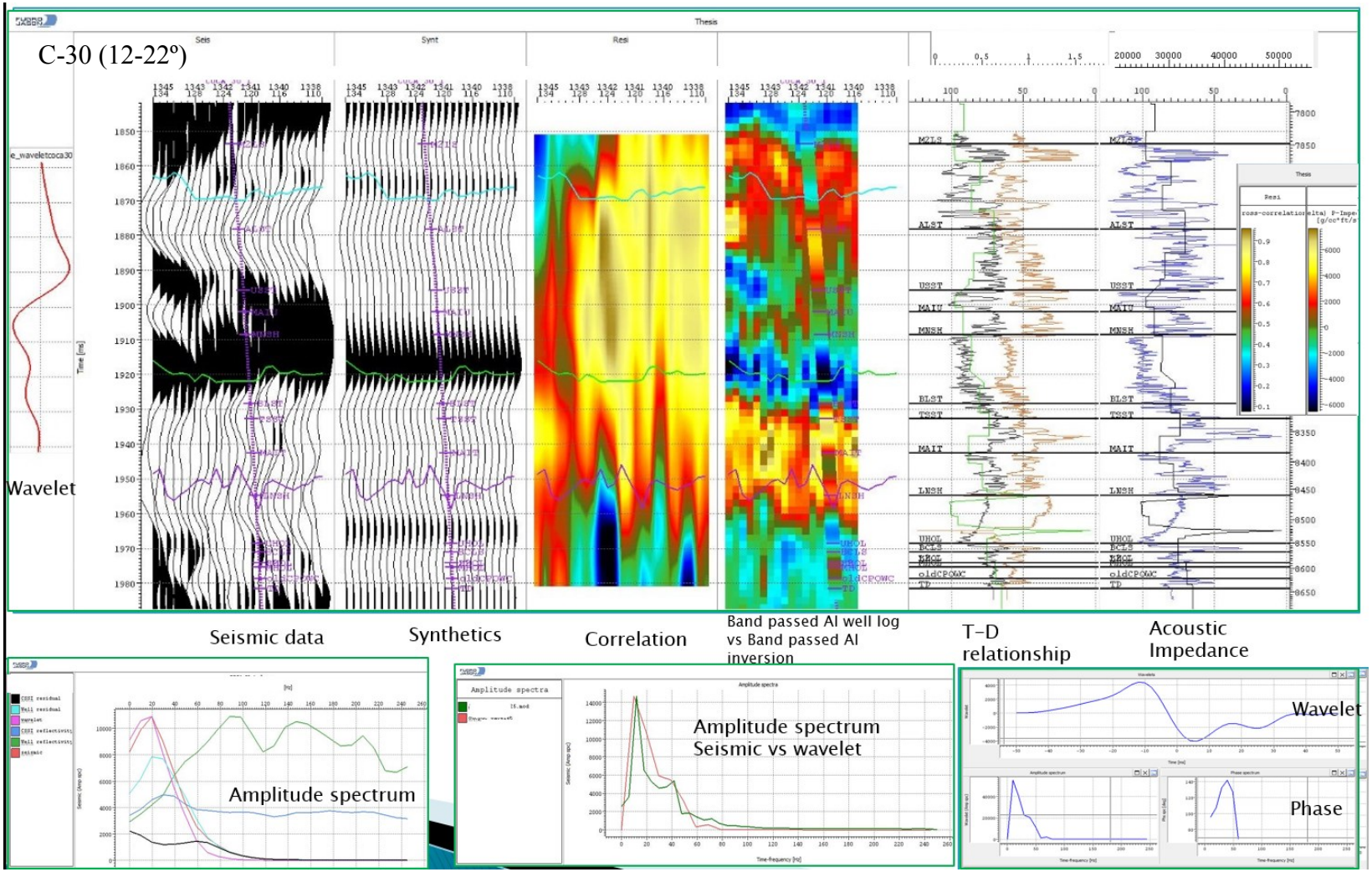

Figure 46. Continued

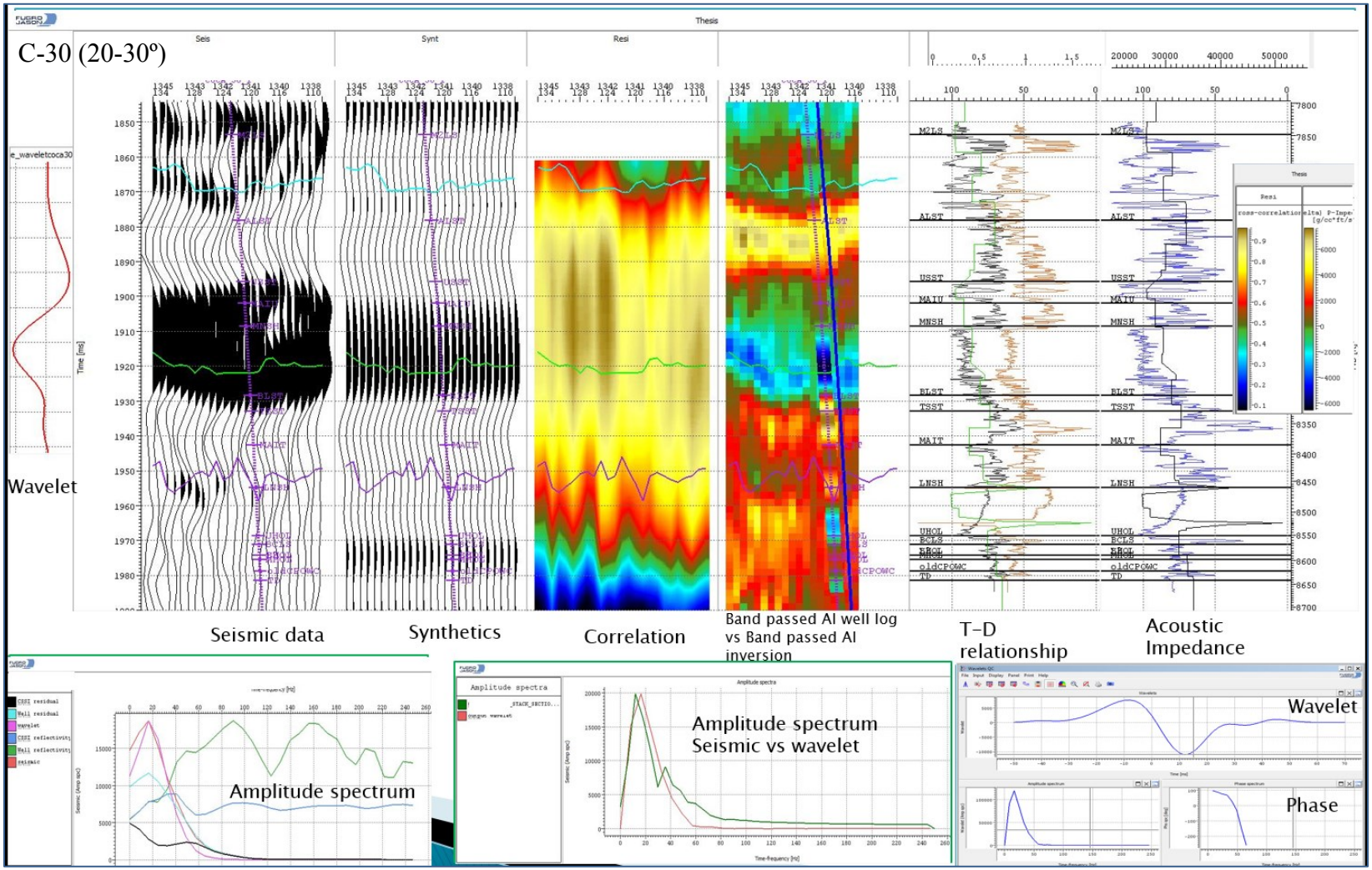

Figure 46. Continued

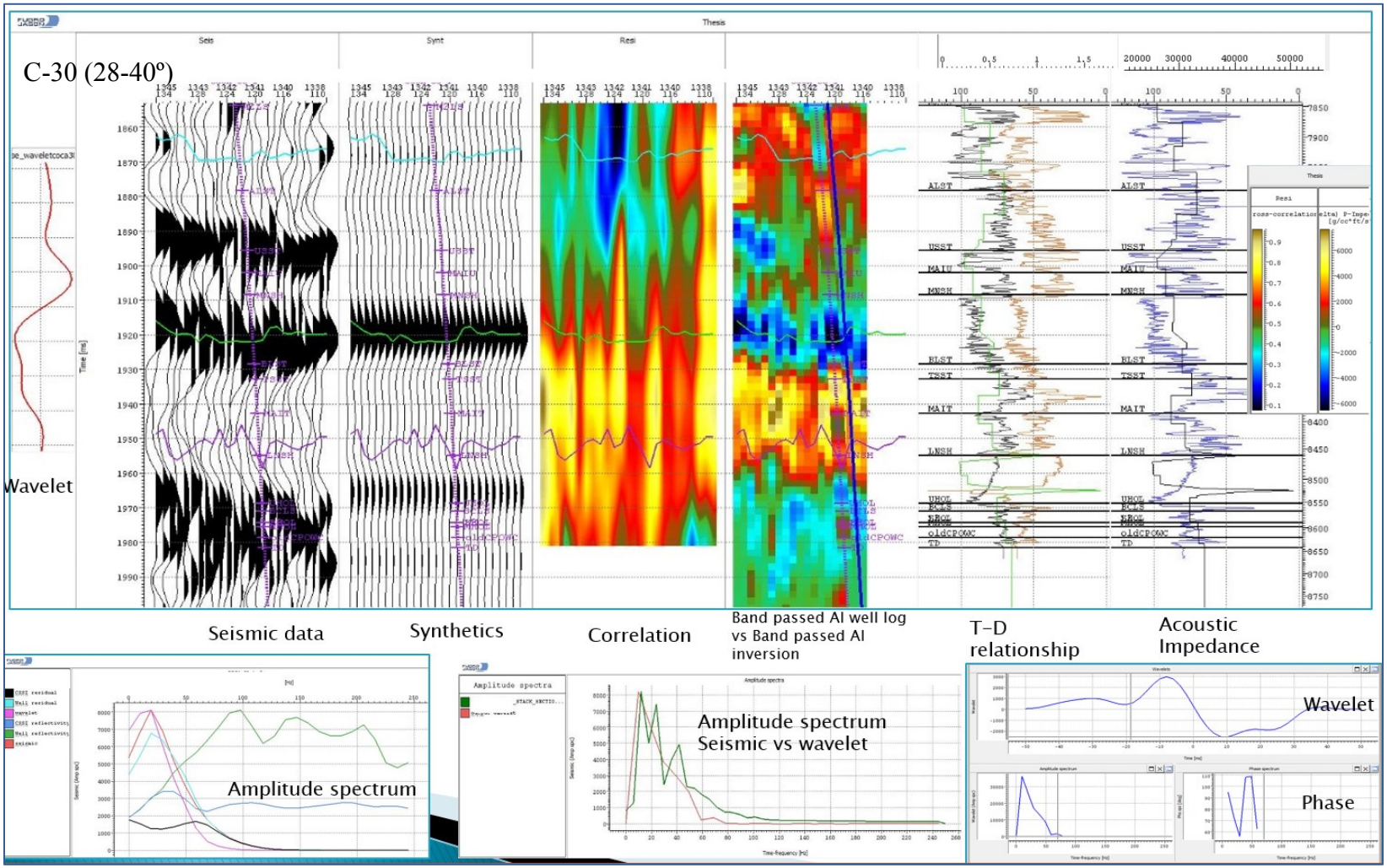

Figure 46. Continued

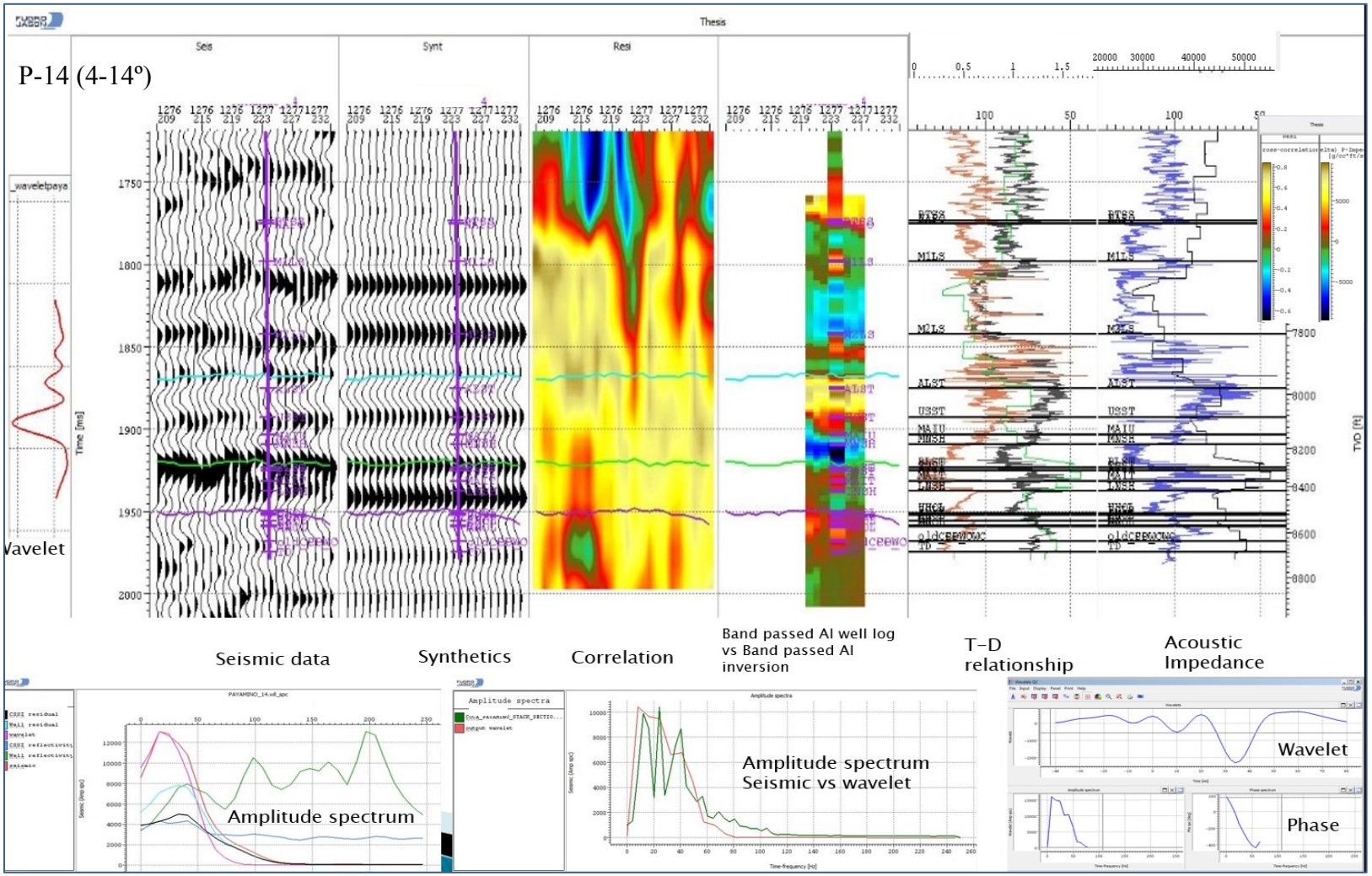

Figure 47. Well P-14. Wavelet extraction (see explanations in the text)

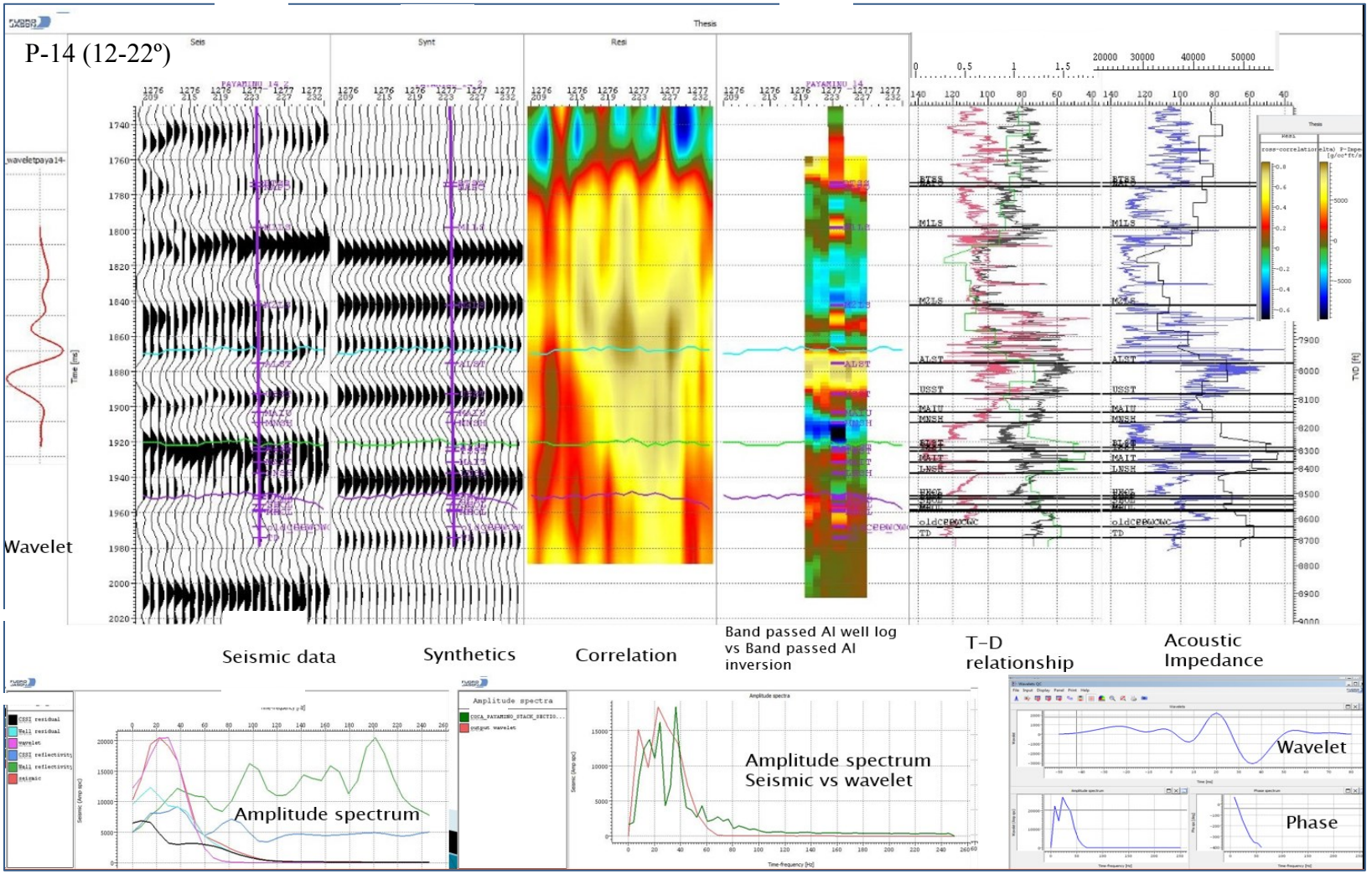

Figure 47. Continued

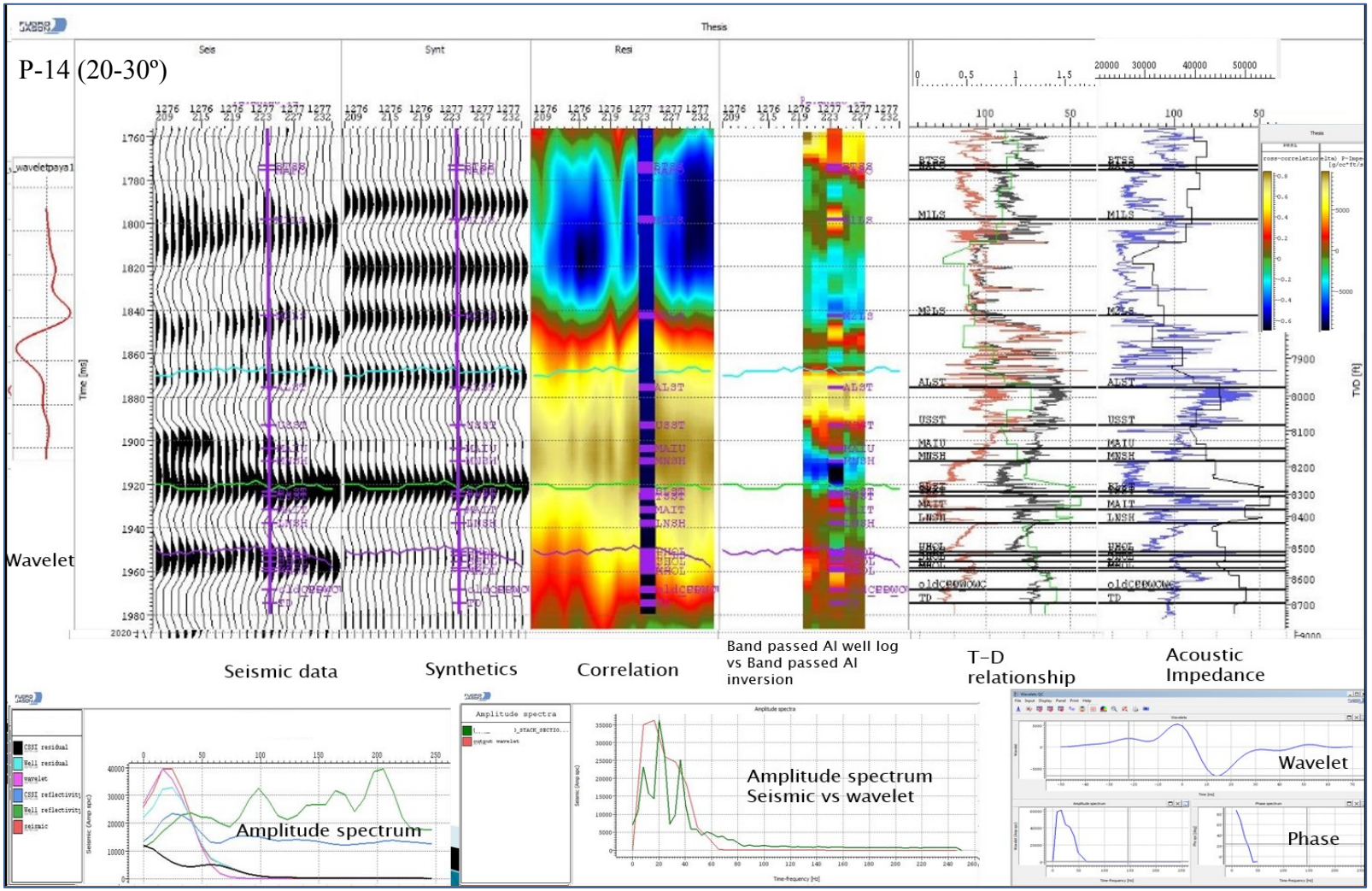

Figure 47. Continued

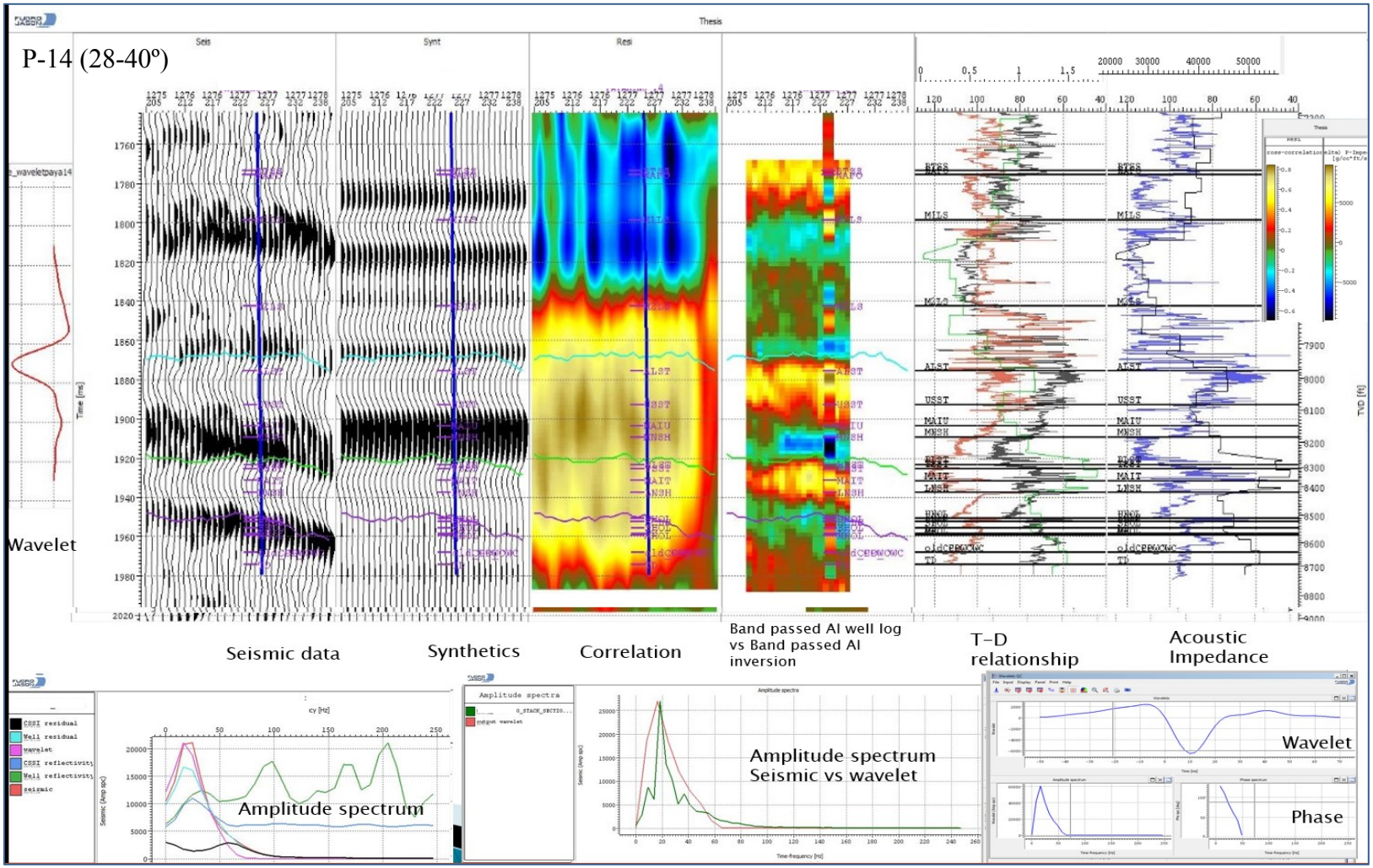

Figure 47. Continued

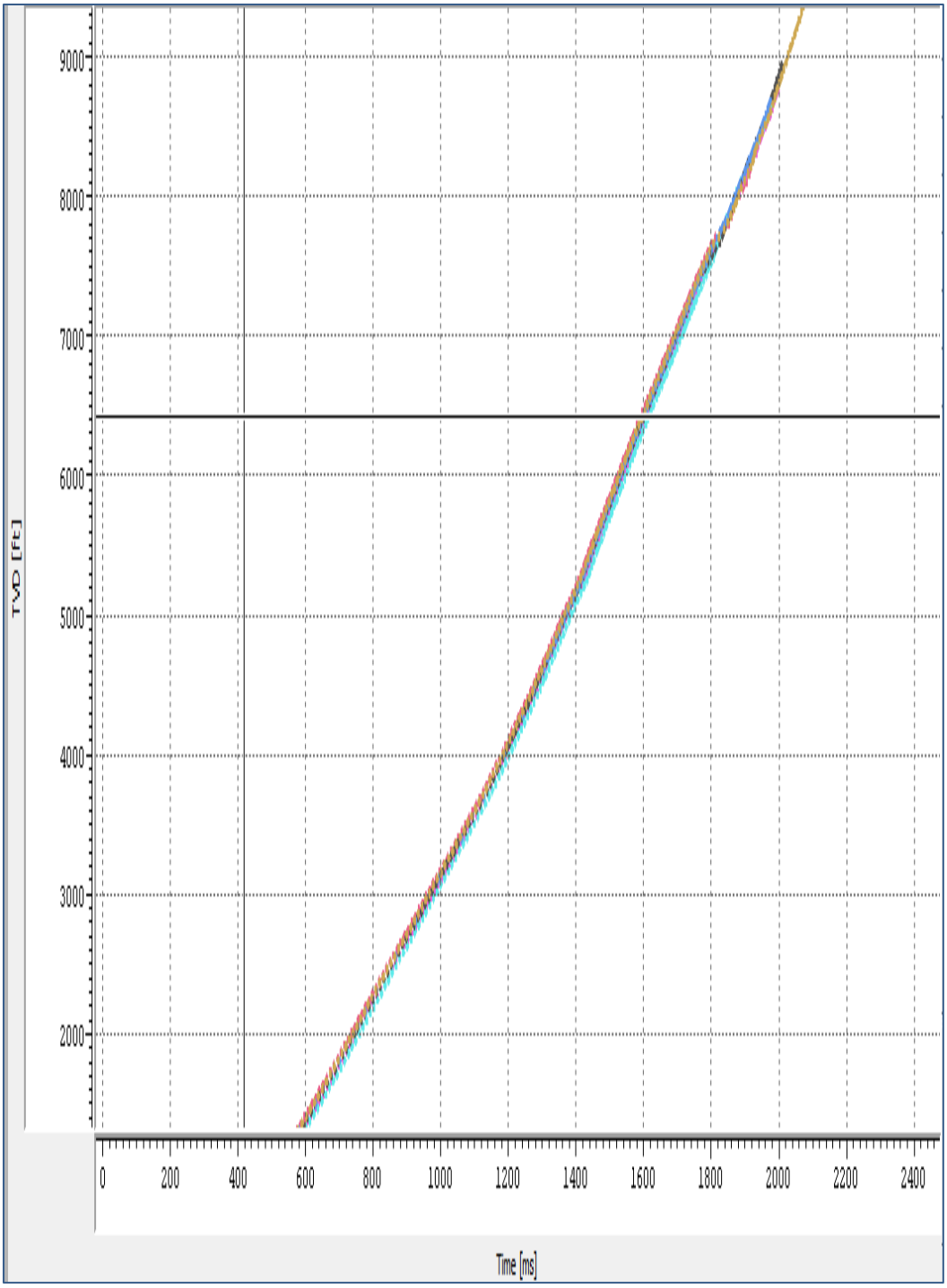

Figure 48. T-D relations after wavelet extraction for the wells C-30, C-31, C-33, C-21, P-14 and P-15

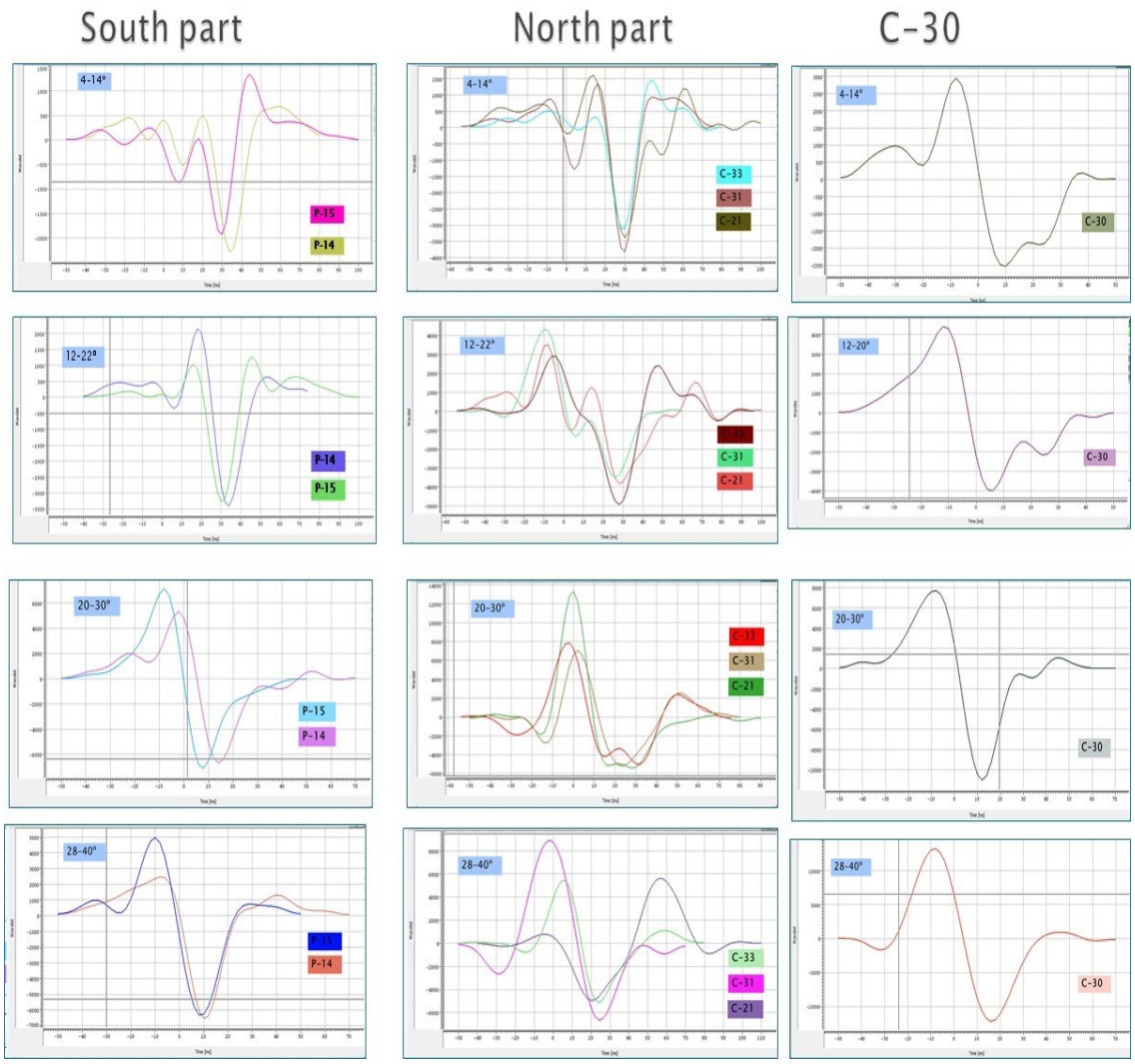

Figure 49. Extracted wavelets from the wells C-30, C-31, C-33, C-21, P-14 and P-15

Since the simultaneous inversion is a Spike-Sparse Inversion, the final results have the same frequency band width as the extracted wavelet. It means that the final outcome from inversion loses the low frequency component. In order to obtain quantitative accurate results, this gap in frequency must be filled with the low frequency from well log interpolated model. Also, the spatial trend of the model will be used to

constraint the inversion. The importance of the low frequency is directly related with the quantitative interpretation of the seismic results. Porosity and frame flexibility factor inversion relie on the quantification of the inversion results. Adding the low frequency to the band passed inversion results, it is possible to recover the real values of P-impedance, S-Impedance and density. For each of the elastic parameters obtained by inversion it is necessary to merge with a low frequency model of each parameter.

Quality control of seismic inversion results

For each of the misfit function described in equation 16, a set of parameters are tested in order to optimize the inversion process through the minimization of the objective function. The best results were obtained using the four angle gather stacks. With each update of the elastic parameters, the objective function is evaluated until the minimum is reached. All the constraints for the misfit functions are based on the well log data and the previous knowledge of geology. These constraints help to reduce the number of possible models that minimize objective function.

After the inversion, the analysis of the cross correlation between synthetics and seismic data is performed. The values of cross correlation decrease in abrupt way in the third angle gather stack. It can be concluded that the third angle gather stack presents some noise influence. The zone that presents low cross correlation need to be analyzed in order to understand if the problem is localized at a specific depth or it is spread in the whole vertical interval. Also, this can explain the reason why the use of four angle stacks gave better results than the use of three angle stacks. The reduction in the accuracy of the

S-Impedance results due to the problems in the 20-30º angle stack, could be compensated by the information contained by the 28-40 º angle stack.

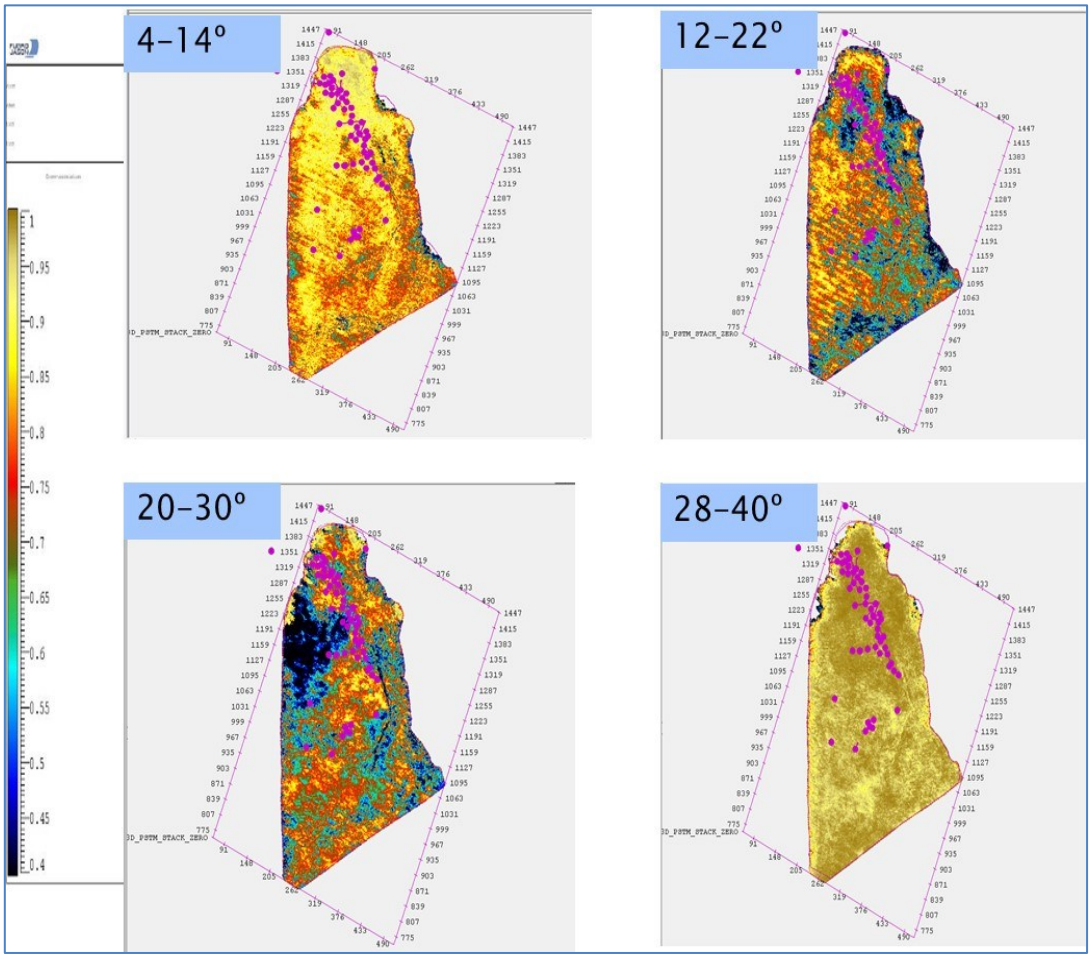

Figure 50. Analysis of the inversion results. Cross-correlation of the seismic-synthetics for the four angle gathers stacks

Figure 51 shows the residuals from synthetics and seismic data in the four angle-gather stacks. The most affected volume is the third one and the residuals are spread in

the whole vertical section confirming that the problem can be related with some processing problem, probably NMO velocity picking.

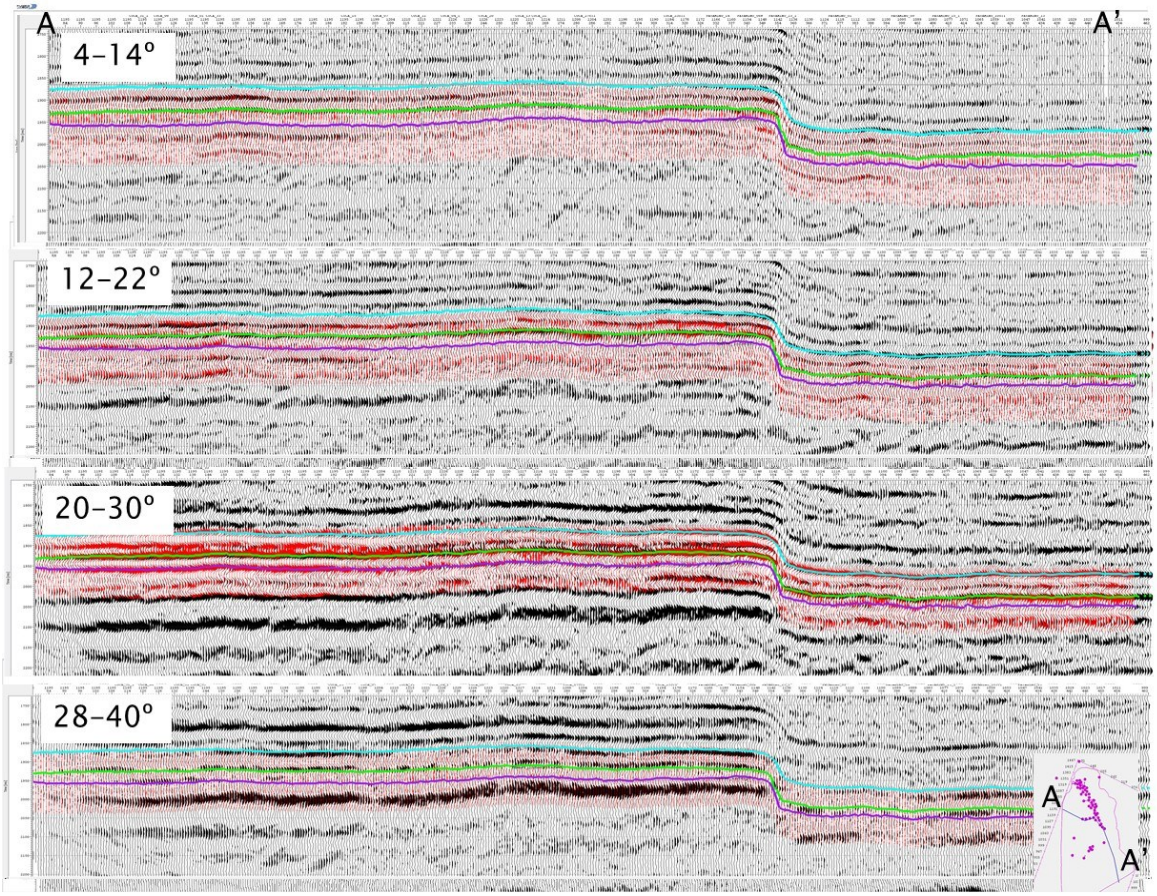

Figure 51. Analysis of the inversion results. Residuals of the seismic-synthetics for the four angle-gathers stacks

Figure 52 is a cross plot of the P-impedance from well logs filtered to seismic frequency vs. pseudo logs extracted from the P-Impedance volume at the well location. The upper plot shows the wells used in the inversion and the lower plot shows all wells

that have P-Impedance log curve. Based on these cross plots, it is concluded that P-Impedance predictability is robust. Both cross plots present a correlation around 80% that prove that the results are very consistent. Figure 53 is a cross section of the P-Impedance plotted with the wells C-30, C-31, C-33, C21, P-15 and P-14. Wells are plotted with colored spectrum and filtered to the seismic frequency (0-50 Hz). U sandstone location is marked in the figure. There is a sharp P-Impedance contrast between A limestone and U sandstone. This sharp contrast is useful to pick a new horizon at the top of U sandstone (black horizon) that allowed delineating the structure of the target reservoir. As it was expected, there is a weak P-Impedance contrast between the U sandstone and the MNSH; therefore, the application of P-impedance-S-Impedance combination and the derived elastic parameters is mandatory to separate these two formations. Figure 54 is showing two cross sections from the P-Impedance volume in two different directions with many wells that were not used in the inversion process. Volume and logs matches in the studied section; however, above the A Limestone a mismatching is evident. After the wavelet extraction, lateral and vertical variation of the wavelet was confirmed; hence, the zones above the A limestone seem to respond to other wavelet. Also, from the only two obtained calipers logs, it is concluded that M1 and M2 chalk and muddy limestone are very fissile and washouts are very common there.

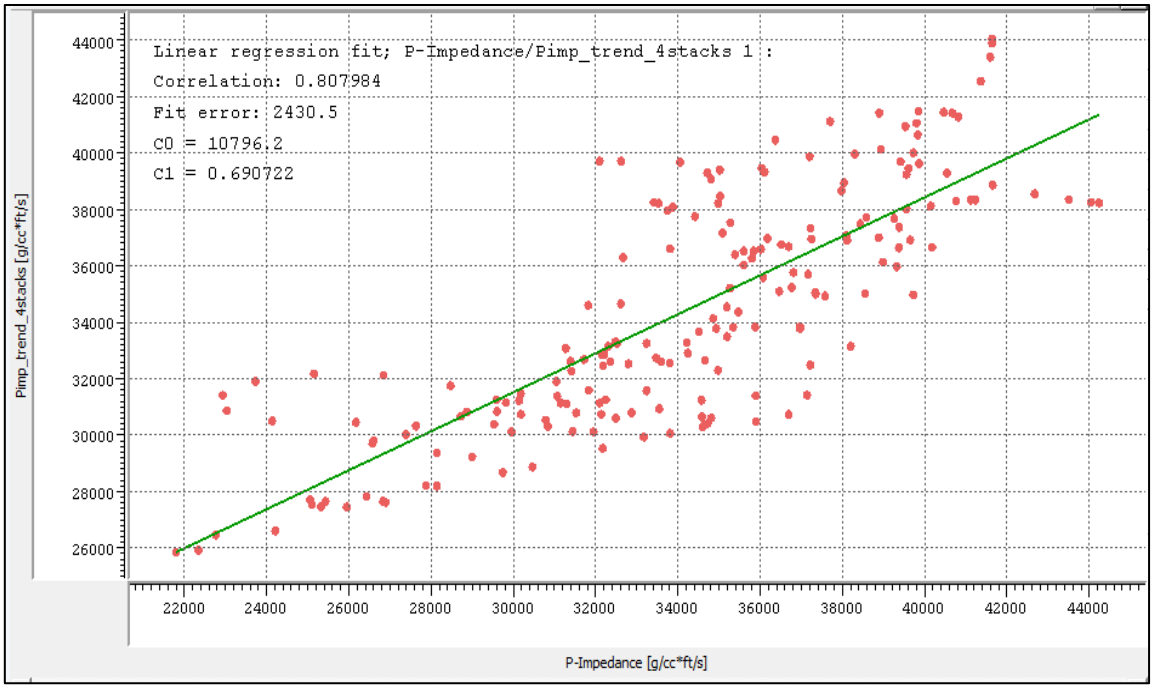

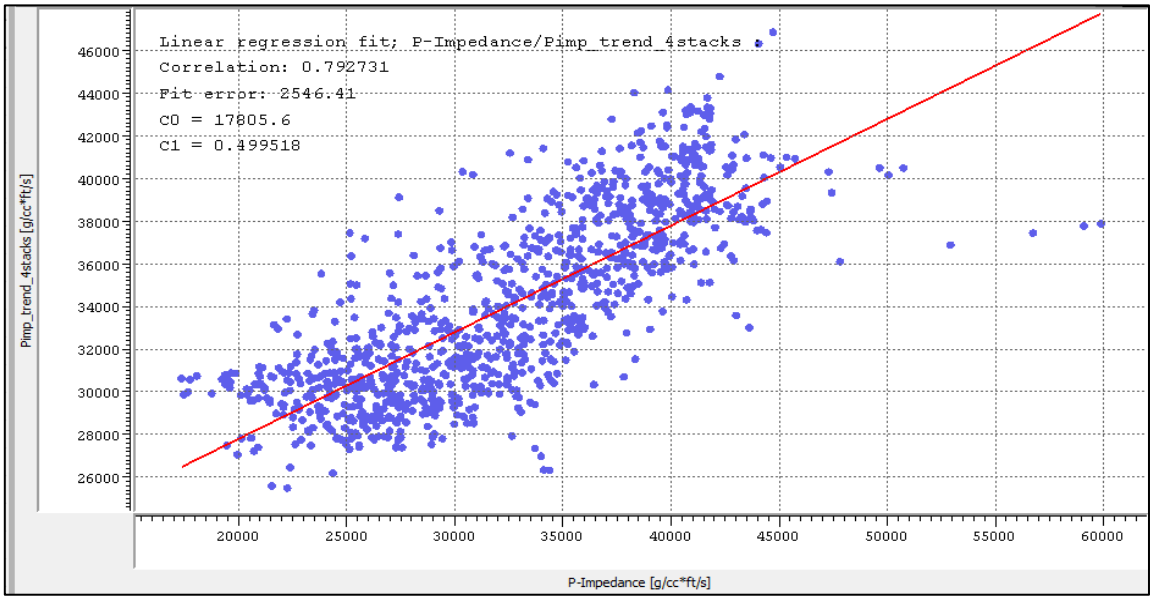

Figure 52. Cross plot of P-Impedance well logs filtered to seismic frequency vs. Pseudo logs extracted from P-Impedance volume. Wells used in inversion (upper plot) and wells do not used in the Inversion (lower plot)

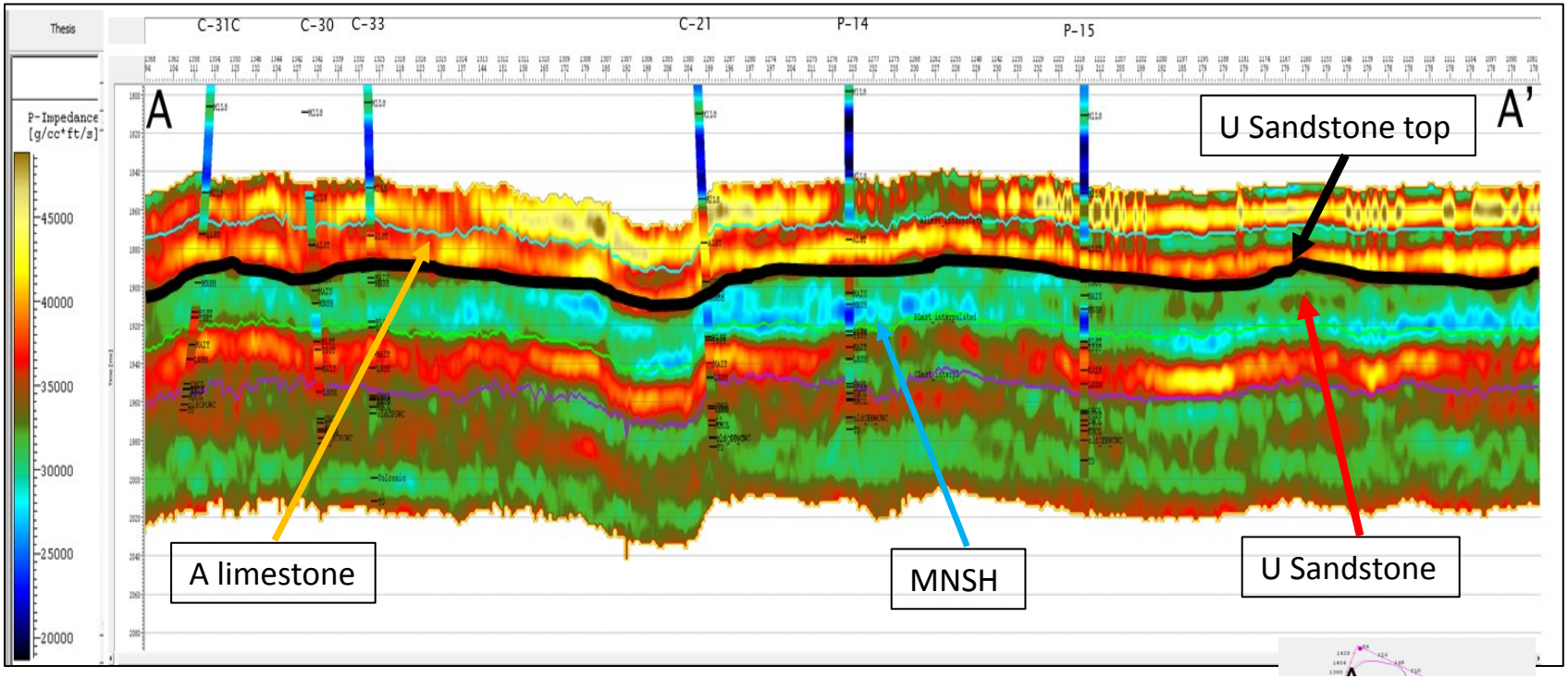

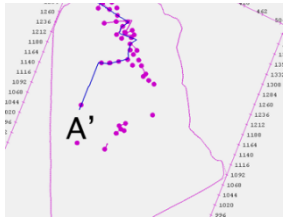

Figure 53. P- Impedance volume and filtered well logs at 0-50 Hz (logs used in the inversion)

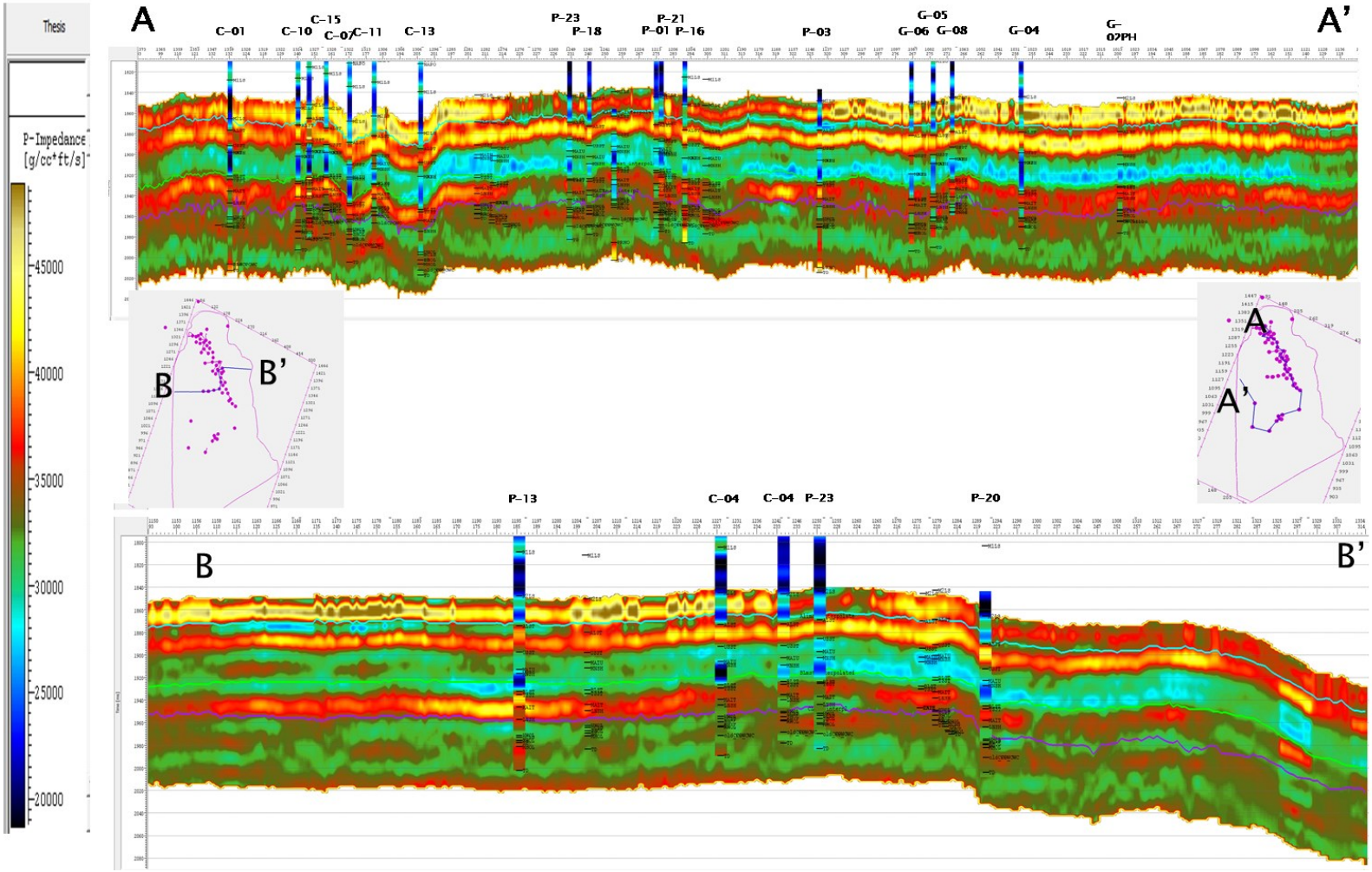

Figure 54. P-Impedance volume and filtered well logs at 0-50 Hz (logs not used in the inversion)

Pseudo logs are also extracted from the S-Impedance volume and then compared with the real S-Impedance well logs that are filtered to seismic frequency in Figure 55. Figure 56 is a cross section of the S-Impedance volume in which is possible to see that at the south of the region, the contrast in S impedance from U sandstone is stronger than in the north. It could be inferred that this S-Impedance contrast is related to the tidal bars of Main U which is the most prolific unit.

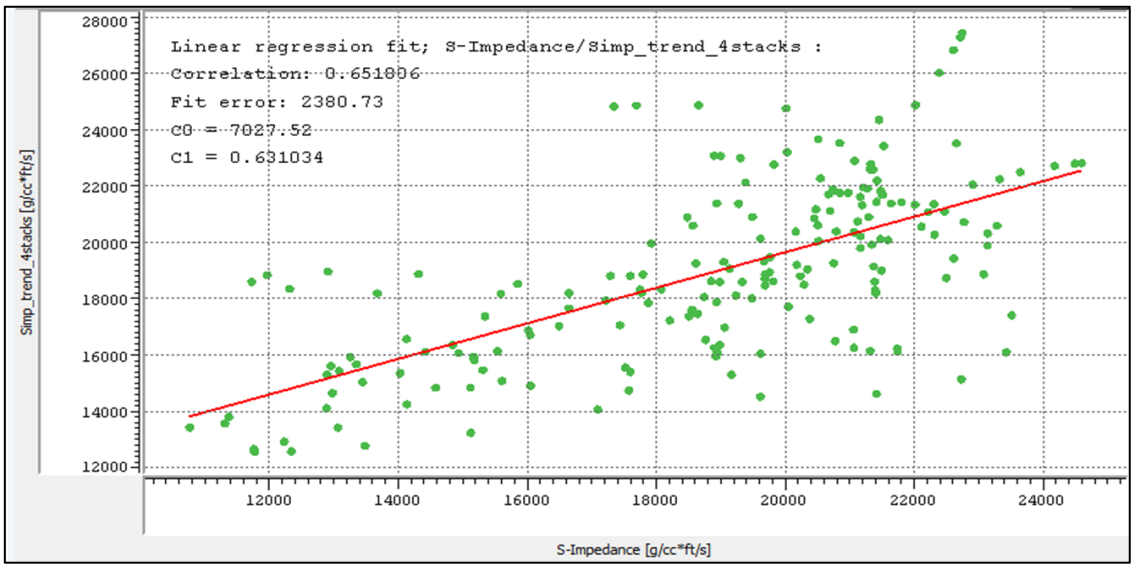

Figure 55. Pseudo logs extracted from S-Impedance volume and filtered well logs at 0-50 Hz (logs used in the inversion)

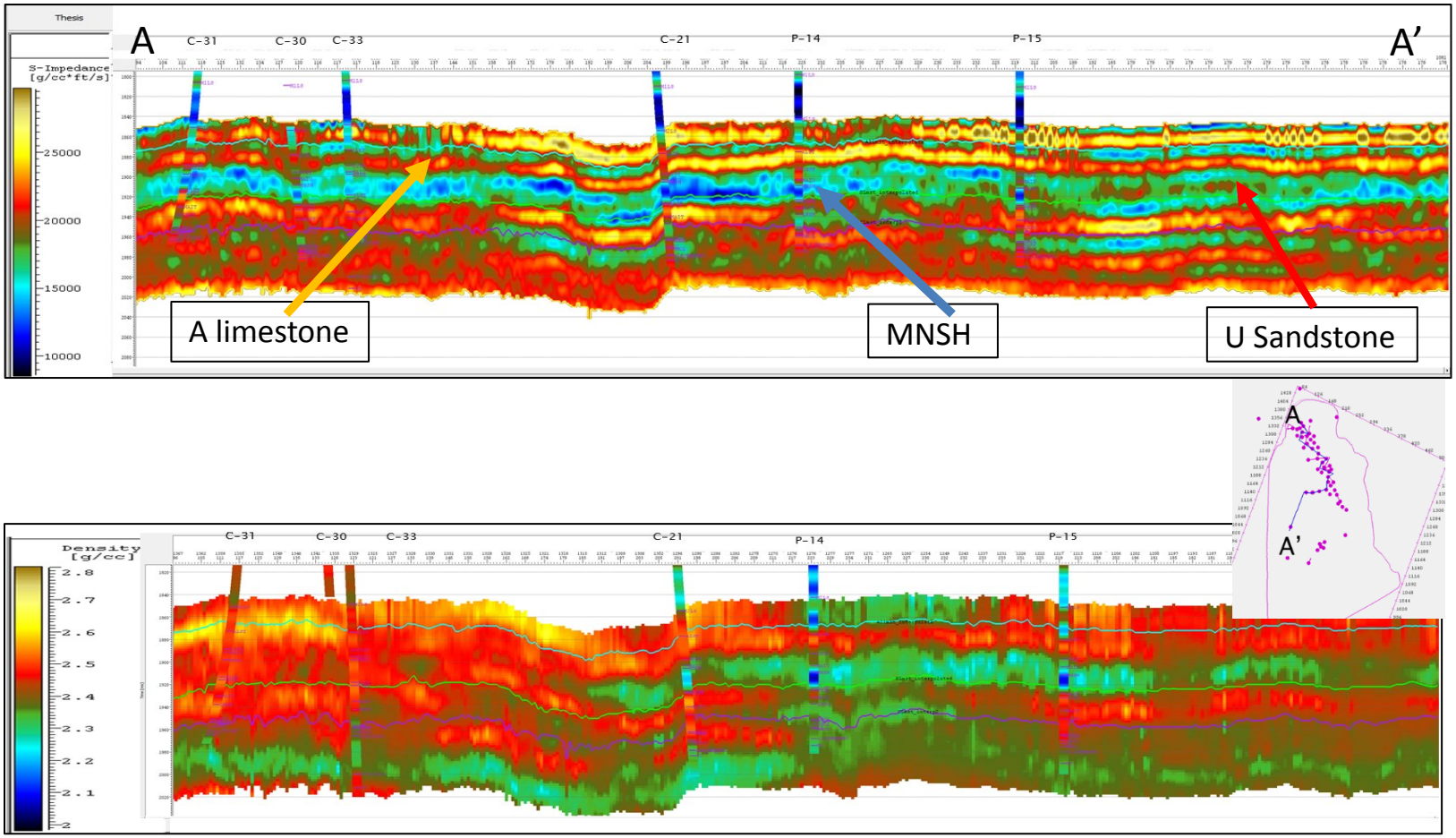

Figure 56. S-Impedance and density volume vs. filtered well logs at 0-50 Hz (logs used in the inversion)

Density inversion was constrained by the application of Gardner, 1974' relation. Density depends in certain way to the change of P-Impedance but also honors the other misfit functions, such as seismic-synthetic correlations, reflectivity contrast, and the trend constraint from the well log interpolation model. Pseudo logs extracted from the density volume vs. the real density logs from wells used in the inversion are shown in Figure 57. The Figure 58 shows the same cross plot from figure 57 with wells that were not used in the inversion; from these two plots, it can be concluded that fair predictability for density has been achieved. However, the scattering points in the cross plot belongs to the north part of the studied zone in figure 58.

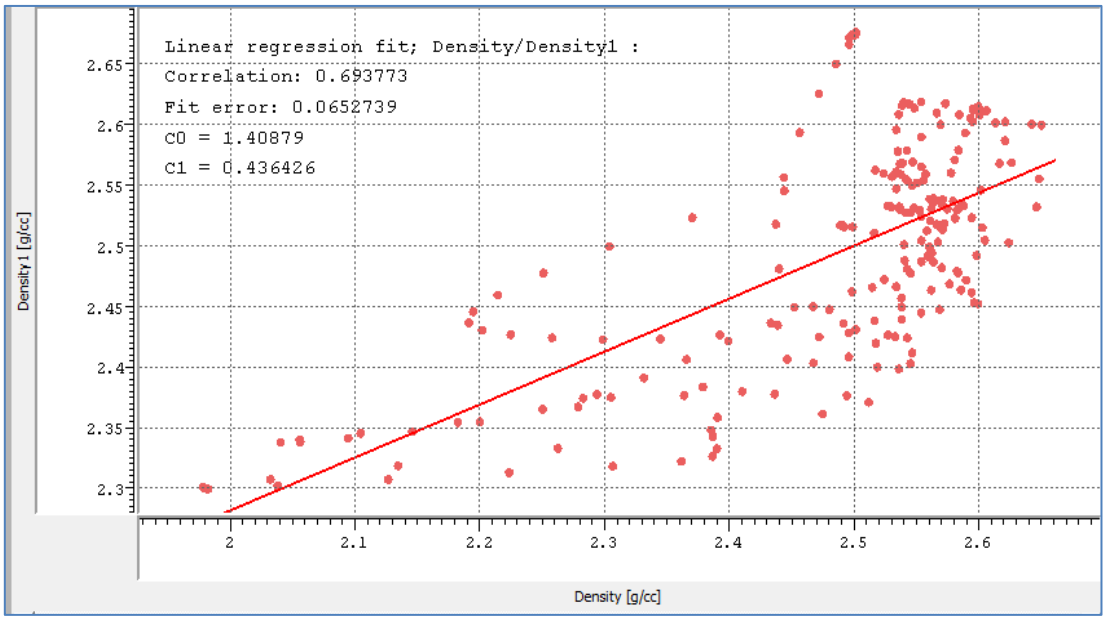

Figure 57. Pseudo logs extracted from density volume and filtered well logs at 0-50 Hz (logs used in the Inversion)

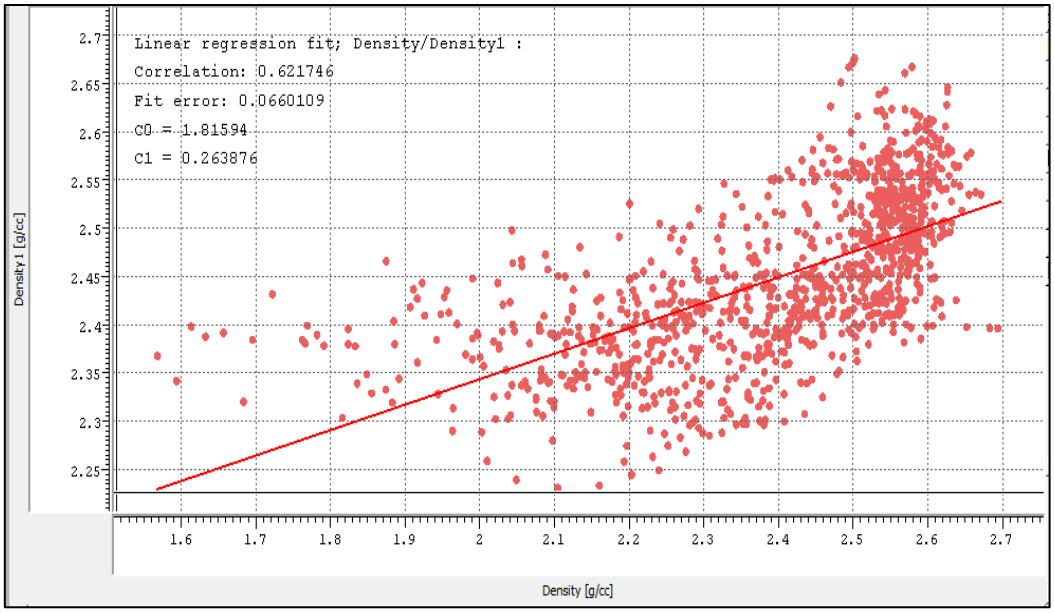

Figure 58. Pseudo logs extracted from density volume and filtered well logs at 0-50 Hz (logs not used in the Inversion)

5. INTEGRATION OF ROCK PHYSICS MODEL TO SEISMIC INVERSION FOR U RESERVOIR

Application of the rock physics model to inversion results

The sharp contrast displayed between the A limestone and the U sandstone allows to pick a new horizon, but there is not strong contrast between U sandstone and MNSH. For this reason it is needed that the combination of P-Impedance and S-Impedance must be used to depict the U sandstone from MNSH. Figure 59 is the plot of S-Impedance vs. P-Impedance from pseudo log extracted from the inversion results at the well track direction with reservoir discriminator (Vcl < 0.4, ϕ>0.08) in z axis. The red color represents reservoir facies. Reservoir discriminator log was filtered to the seismic frequency. From this plot it can be concluded that the reservoir facies are grouped in a specific zone of the graph that is marked by the black polygon. On the other hand, not only reservoir facies can be depicted using this polygon restriction since some of non-reservoir facies with similar P-Impedance and S-Impedance values show an overlap onto reservoir facies. This step is important since our objective is to use Sun, 2000' model to depicted quality of the facies and get porosity in sandstone unit. From the rock physics analysis, it was concluded that most reliable results of the application of Sun, 2000's model will be obtained in sandstones intervals because of the assumption of constant *c* ratio and because the mineralogical composition is known and it is fairly constant in sandstones. In shales the constant *c* ratio assumption is not accurate and this assumption could introduce some errors that can produce a misinterpretation. For all the

reasons exposed above; first, it is mandatory to depict reservoir facies from non-reservoir facies.

According to rock physics, analysis at well logs frequencies the discrimination of reservoir and non-reservoir facies must not have had any problem as shown in figure 37. However, previous indicated problems in seismic acquisition and processing, that affect the resolution of seismic data, produced similar elastic response of some shaly and shale intervals.

Figure 60 shows pseudo logs extracted from S-Impedance and P-Impedance volumes of some wells. The whitened zones are the highlighted zones that correspond to the points enclosed in the polygon in Figure 59. USST is the top of U sandstone and MNSH is the top of the overlaid shale. Figure 60 shows that in well locations the differentiation of U sandstone is good at the zone of P and G wells but at the zone of C wells the differentiation is only fair. The cross section of P-Impedance volume restricted to the extracted facies from the polygon and flattened to A limestone top is shown in Figure 61. This figure shows that gamma ray and resistivity logs from wells that do not have sonic log curve. This curves match in an acceptable way with the extracted volume. In this figure, zones of interest show low gamma ray values and moderate resistivity. Gamma ray curve is black and resistivity is red. As it was expected, the overlap of reservoir and non-reservoir facies points in the cross plot from Figure 60 produces that some shale zones will be included in the restricted P-Impedance volume.

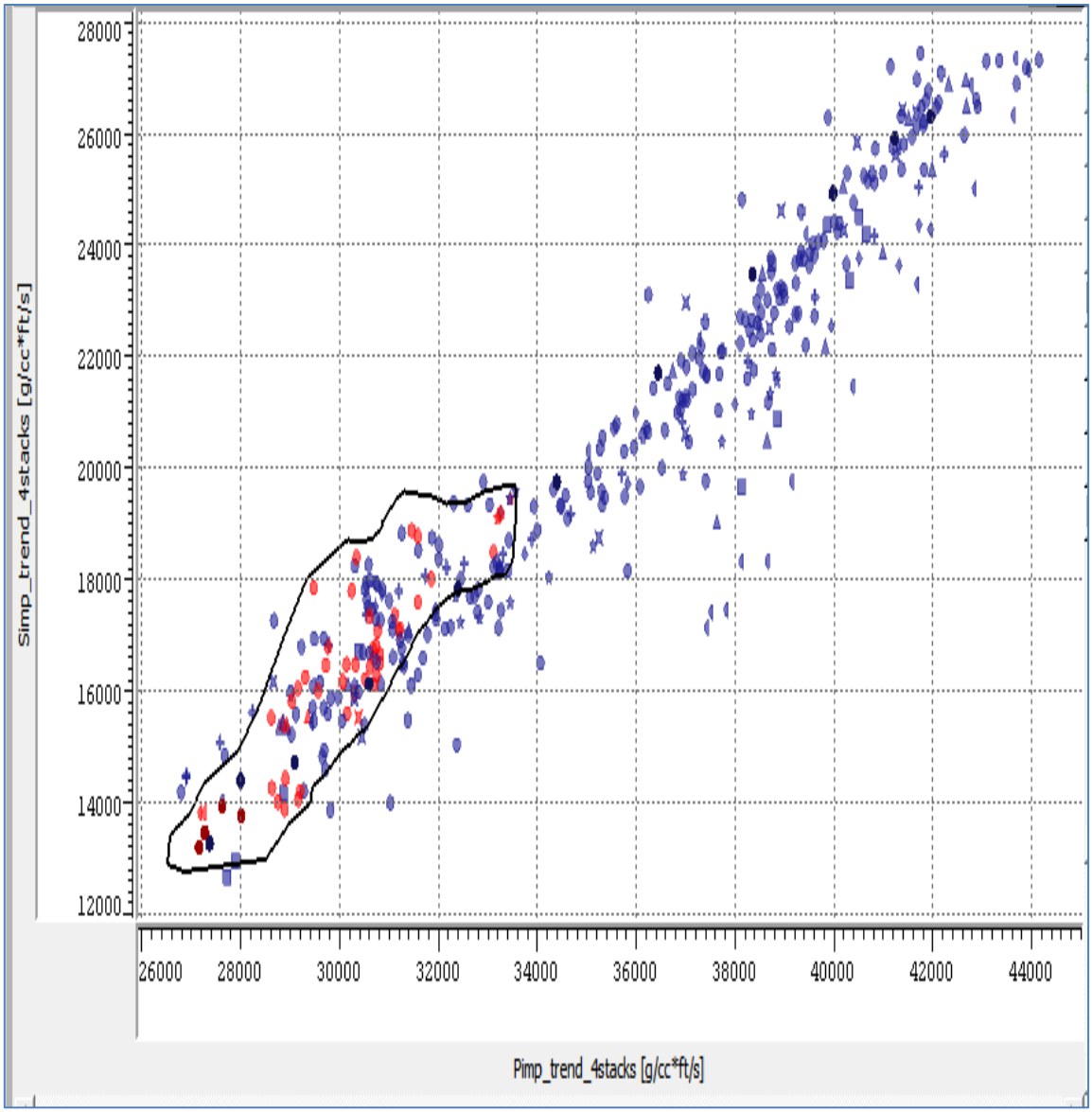

Figure 59. Pseudo logs extracted from P-Impedance volume and S-Impedance volumes for the A limestone, U sandstone and MNSH. Reservoir discriminator is in z axis (Red=reservoir facies and blue-non-reservoir facies)

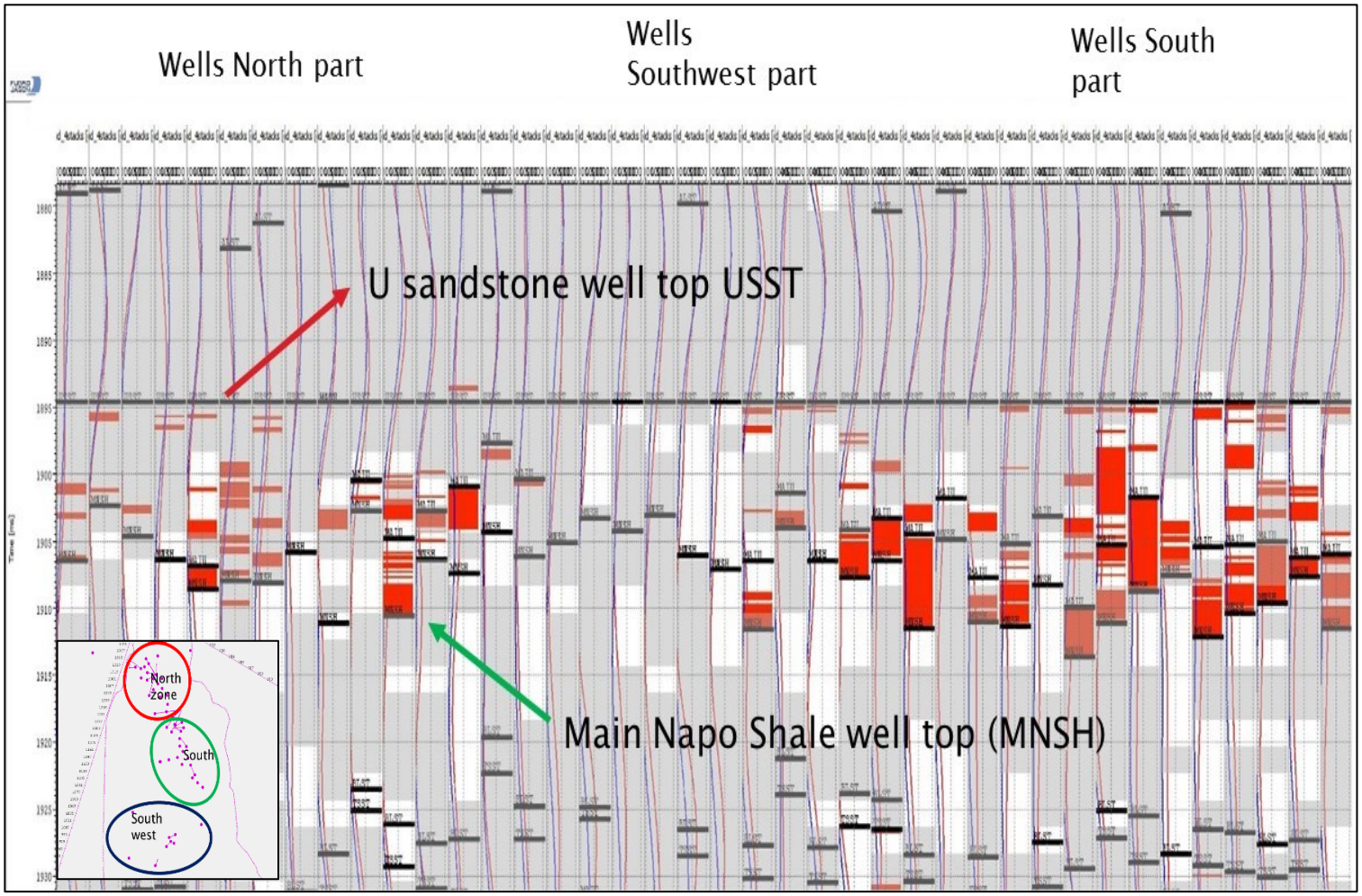

Figure 60. Highlighted zones extracted from the polygon in figure 59 with P-Impedance and S-Impedance pseudo logs for the A limestone, U sandstone and MNSH. Reservoir discriminator as a blocky zone.

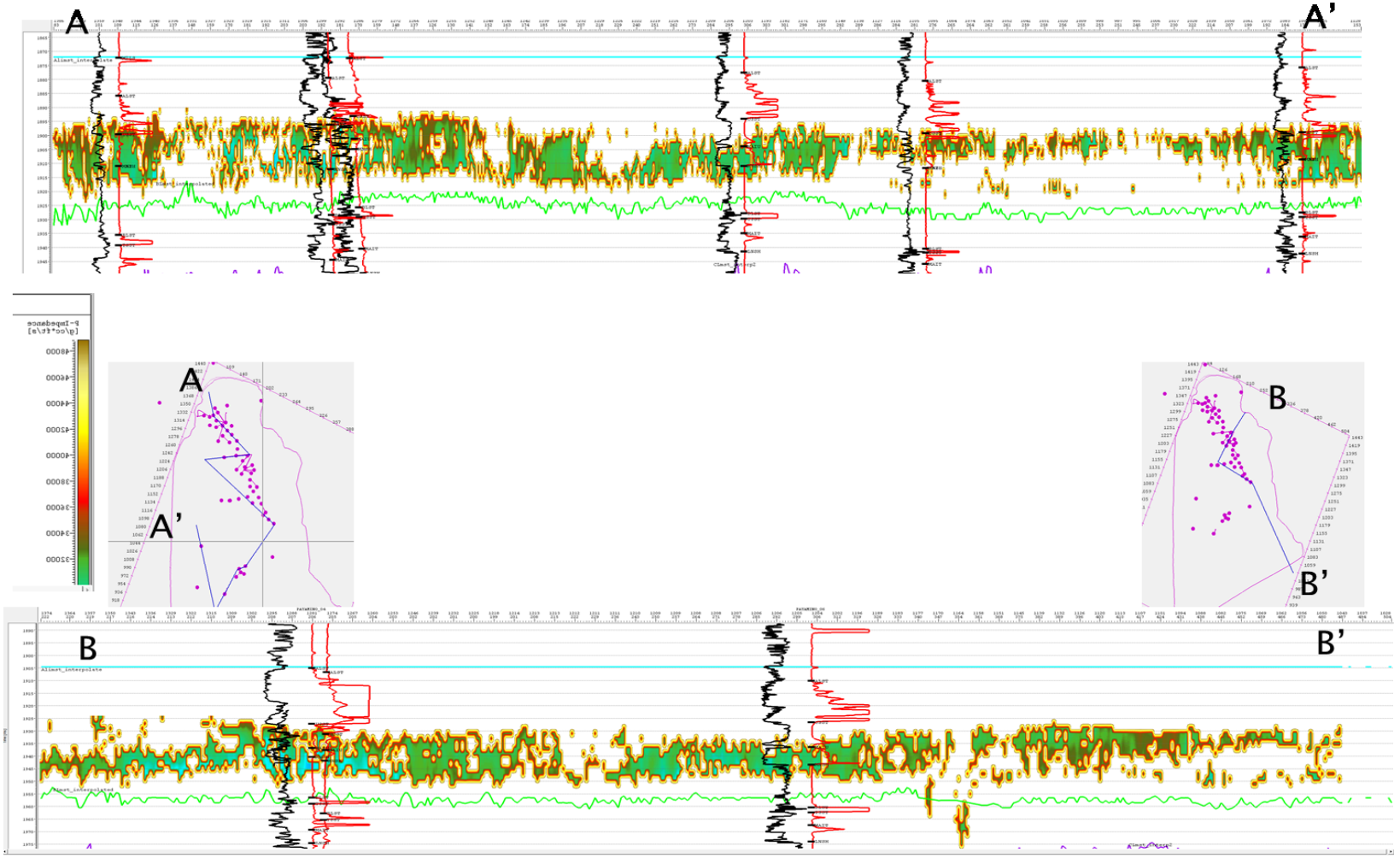

Figure 61. Cross section of the P-Impedance volume result from reservoir facies extraction by polygon in figure 59

Now, that the reservoir facies were depicted with certain accuracy, the next step is to characterize the facies and obtain a porosity volume through the application of Sun, 2000' model.

First able, a rearrangement of the equations must be done by replacement of equations 43, 44, 45 and 13 in equation 42 and considering *c* ratio as a constant. Porosity can be obtained by the equation 48:

$$\phi=\frac{\left(1-\sqrt[c]{\frac{\mu}{\mu_s}}\right)*\left[\left(\frac{kf}{ks}\right)*\left(\frac{Ks-k}{ks-kf}\right)\right]}{\left(1-\sqrt[c]{\frac{\mu}{\mu_s}}\right)-\left[1-\left(\frac{kf}{ks}\right)*\left(\frac{Ks-k}{ks-kf}\right)\right]} \quad (48)$$

and γ_k comes from the equation 49

$$\frac{\mathrm{Ln}(\frac{\mu}{\mu_s})}{c*\mathrm{Ln}(1-\phi)}=\gamma k \quad (49)$$

where K and μ are the bulk and shear modulus derived from the inversion results using the equations 50 and 51

$$\mu=\lambda\left(\frac{1-2\sigma}{2\sigma}\right) \quad (50)$$

$$k=\lambda\frac{2}{3}\left(\frac{1+\sigma}{1-2\sigma}\right) \quad (51)$$

where λ is the lambda coefficient and σ is the poisson ratio. λ is derived from the λ-ρ parameters that comes directly from the P-Impedance and S-Impedance volumes:

$$\lambda = \frac{I_p^2 - 2I_s^2}{\rho} \quad (52)$$

$$\sigma = \frac{\left(\frac{Ip}{Is}\right)^2 - 2}{2\left(\frac{Ip}{Is}\right)^2 - 2} \quad (53)$$

K_s, μ_s and Kf volumes are created by the interpolation of the previous logs obtained from the rock physics analysis based on the considerations that U sandstone presents a homogenous mineralogical composition. Then, frame flexibility factor γ_k is calculated using the equation 49. Since the resolution of seismic data is lower than the well logs, the facies extracted from the polygon in figure 59 comprises the facies from Upper and Main U. It is not possible to discriminate between these two units; therefore a new average c ratio for this two intervals is calculated and it is equal to 1.17. This value comprises the *c* ratio values of all the facies in U sandstone since the final volume also contains shaly facies that were depicted by the overlapping points in the cross plot of Figure 59.

In order to test the accuracy of the results, porosity pseudo logs were extracted from the porosity volume and compared with porosity logs calculated by the petro physical approach for all wells, (Figure 62). Although, there is some scattering points, the correlation is good and around 60 %. Values from log porosity are little higher than the values from inversion. Figure 63 shows two cross section of the porosity volume with the porosity logs filtered to the seismic frequency.

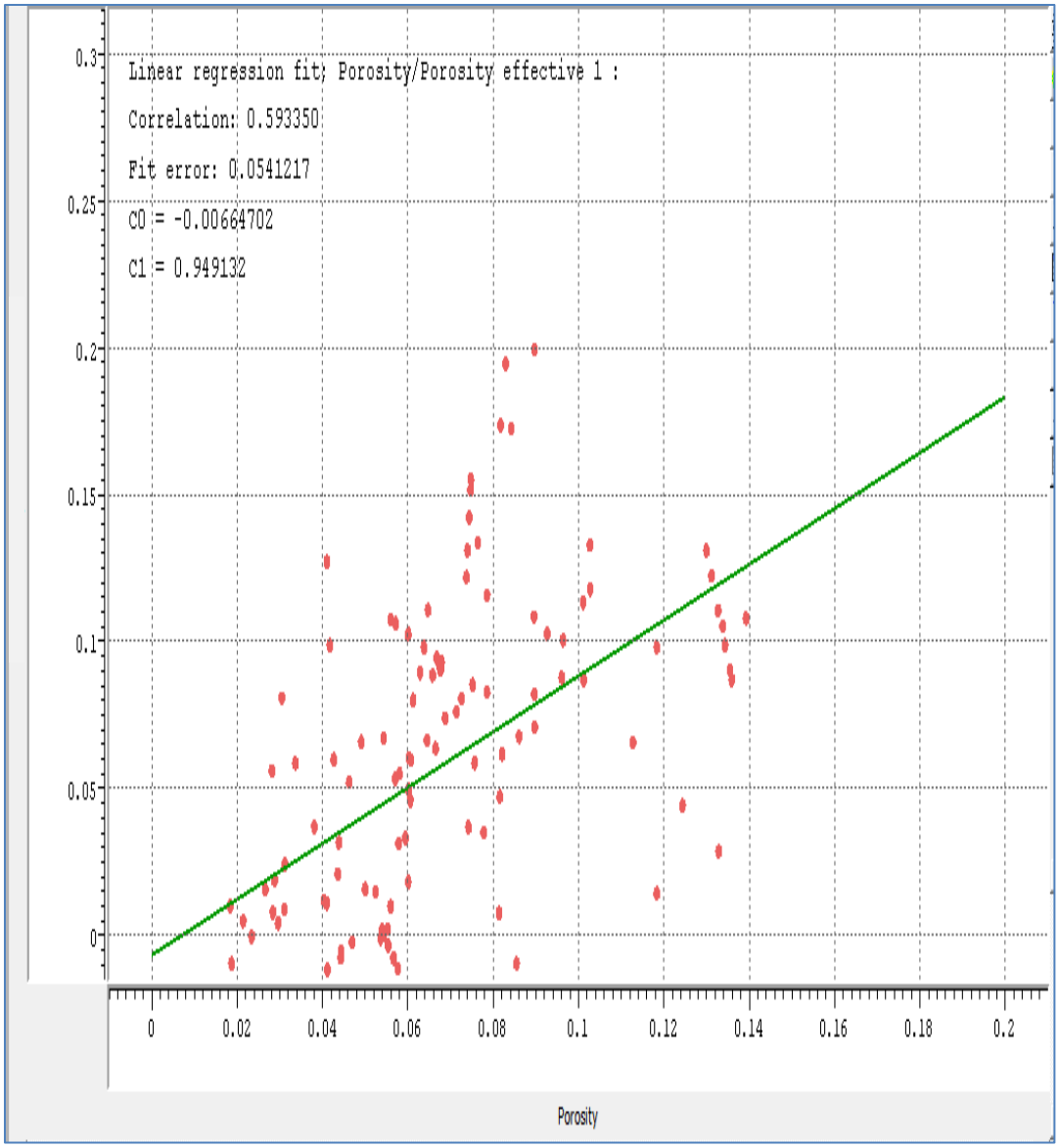

Figure 62. .Pseudo logs extracted from Porosity volume vs. porosity logs calculated by petro physical approach for U sandstone.

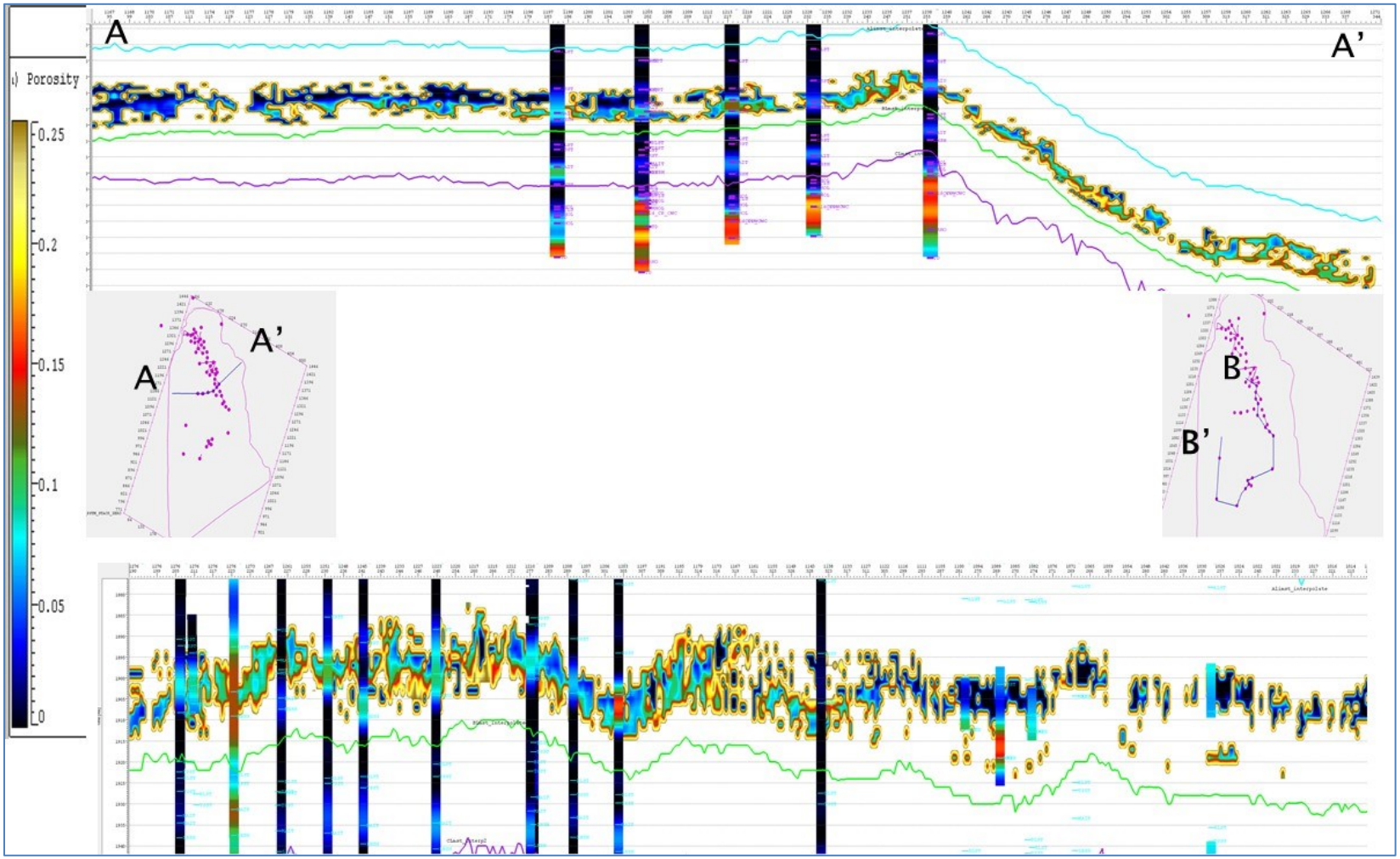

Figure 63. Cross section of the porosity volume

Analysis of the inverted compressional frame flexibility factor (γ_k) and porosity

Besides porosity volume, frame flexibility factor was obtained after inversion. As it was stated before, in the rock physics model, frame flexibility factor (γ_k) is useful to characterize facies in U sandstone. First, we need to establish which values of γ_k represent each class of facies. The cross plot of porosity vs. P-Impedance with γ_k in the z axis is created and shown in Figure 64. This cross plot shows a strong similarity to the cross plot from Figure 39.

The discriminator of Vcl <0.6 is set and it make possible to visualize that most of the shale facies (Type I) are located in the zone with porosity value of 0 or less than 0 and with γ_k values less than 2, especially negative values. Values of γ_k between 2 and 8 represent Type II facies. These facies show high porosity values and low P-Impedance values. Type III facies present a low value of P-Impendence and low porosity with γ_k values between 8 and 12. And, Type IV facies presents very low porosity from 0-5 % and low P-Impedance values with a γ_k higher than 12. Type IV facies cannot be considered as a reservoir facies due to the low porosity. To confirm this criterion, the same cross plot of Figure 64 with the reservoir discriminator in z axis is plotted in Figure 65. As it was expected, most of the reservoir facies are located in the zone of Type II and Type III facies.

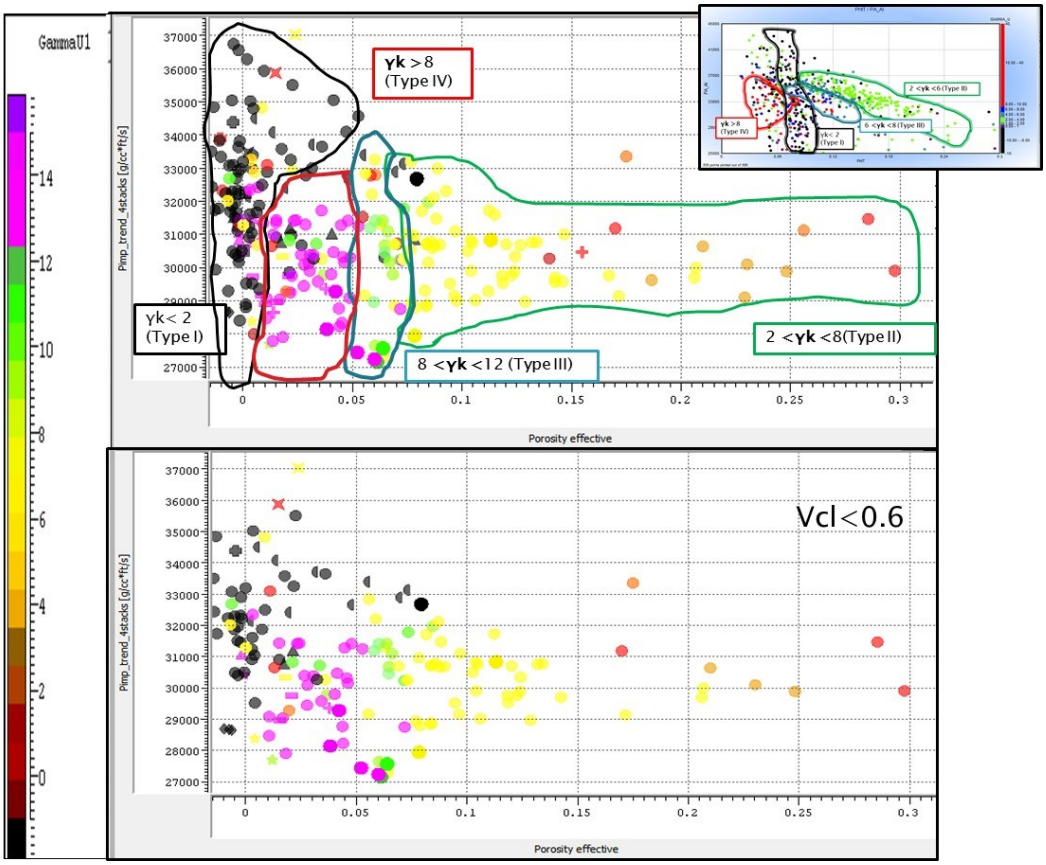

Figure 64. Cross plot of P-Impedance vs. inverted porosity with γk in z axis for U sandstone. Lower plot is the same as the upper plot with the cut off for Vcl lower than 0.6.

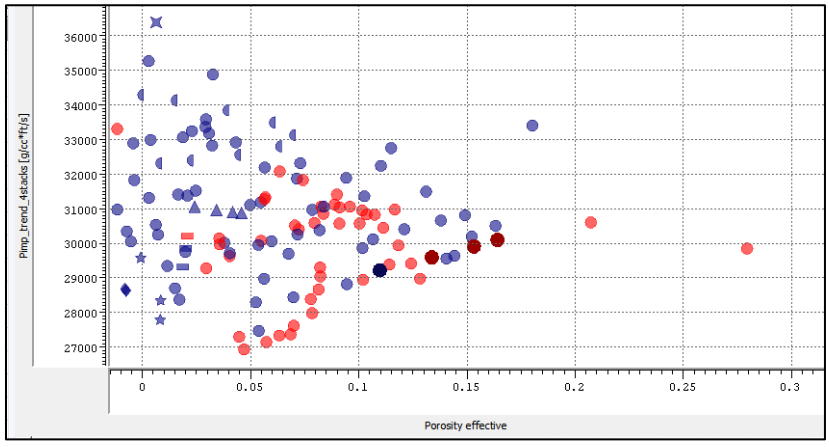

Figure 65. Cross plot of P-Impedance vs. inverted Porosity with reservoir discriminator in z axis for U sandstone. Red points are reservoir facies.

The porosity and γ_k volumes obtained by inversion will be divided in 10 different time slices parallel to the U top sandstone horizon. Figure 66 shows the time slice 2, 4, 6 and 9 from the porosity volume and figure 67 shows the same time slices from γ_k factor volume. The time slices 2 can be interpreted as part of the Upper U sandstone and the time slice 9 as part of Main U sandstone according to the depth of each interval. The areal distribution of the facies and porosity shows that most prolific facies are located a at the center of the oilfield; however, there are some spread zones of good quality associated with tidal bars and shore face bars facies that are located at the south east and south west of the oilfield.

Figure 68 shows a comparison between the time slice 7 from γ_k volume and the sedimentological interpretation using cores made by Vallejo et al., 2013. The areal distribution of facies between these two approaches shows a strong correlation inside the red polygon area that is the analyzed area in the sedimentologcal interpretation. Type II and III facies from inversion can be defined as tidal bars and channels that Vallejo et al., 2013 states were deposited in a SE-NW direction. Type III has lower porosity and finer grain size than Type II, but it can still be considered as reservoir facies with less quality as shown in Figure 64. Type IV facies are sandstones with very fine grain size with some inclusions that can be compared with sand flat facies from sedimentological approach. Finally, Type I facies are the shale facies that match with the estuarine mud flat facies.

Vallejo et al, 2013 states that in Upper U sandstone, the most prolific facies were deposited as shoreface bars at restricted areas with East-West direction.

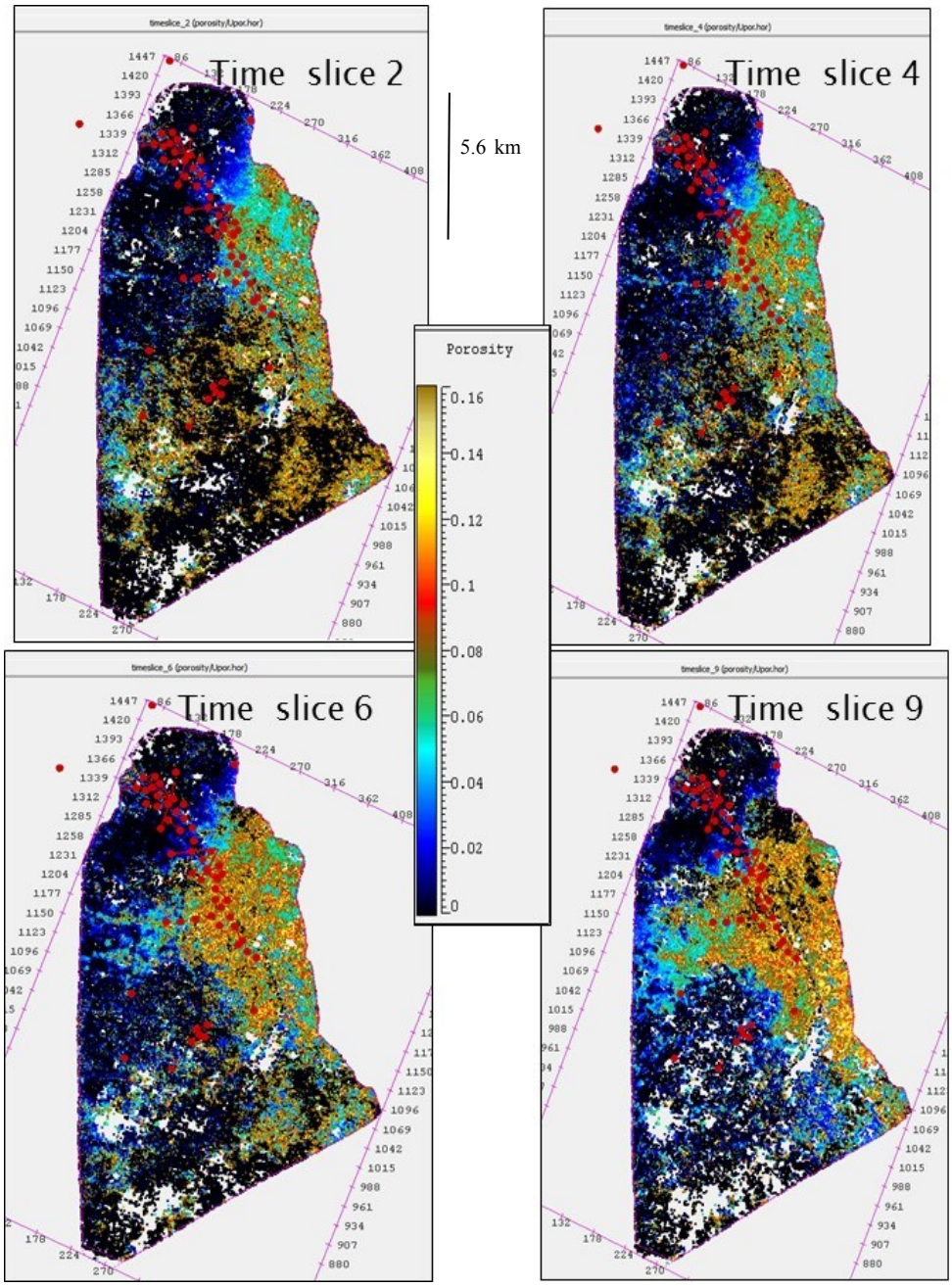

Figure 66. Time slices extracted form porosity volume. The slices 2 and 4 can be inferred as part of the Upper U and the 6 and 9 as part of the Main U sandstone.

.

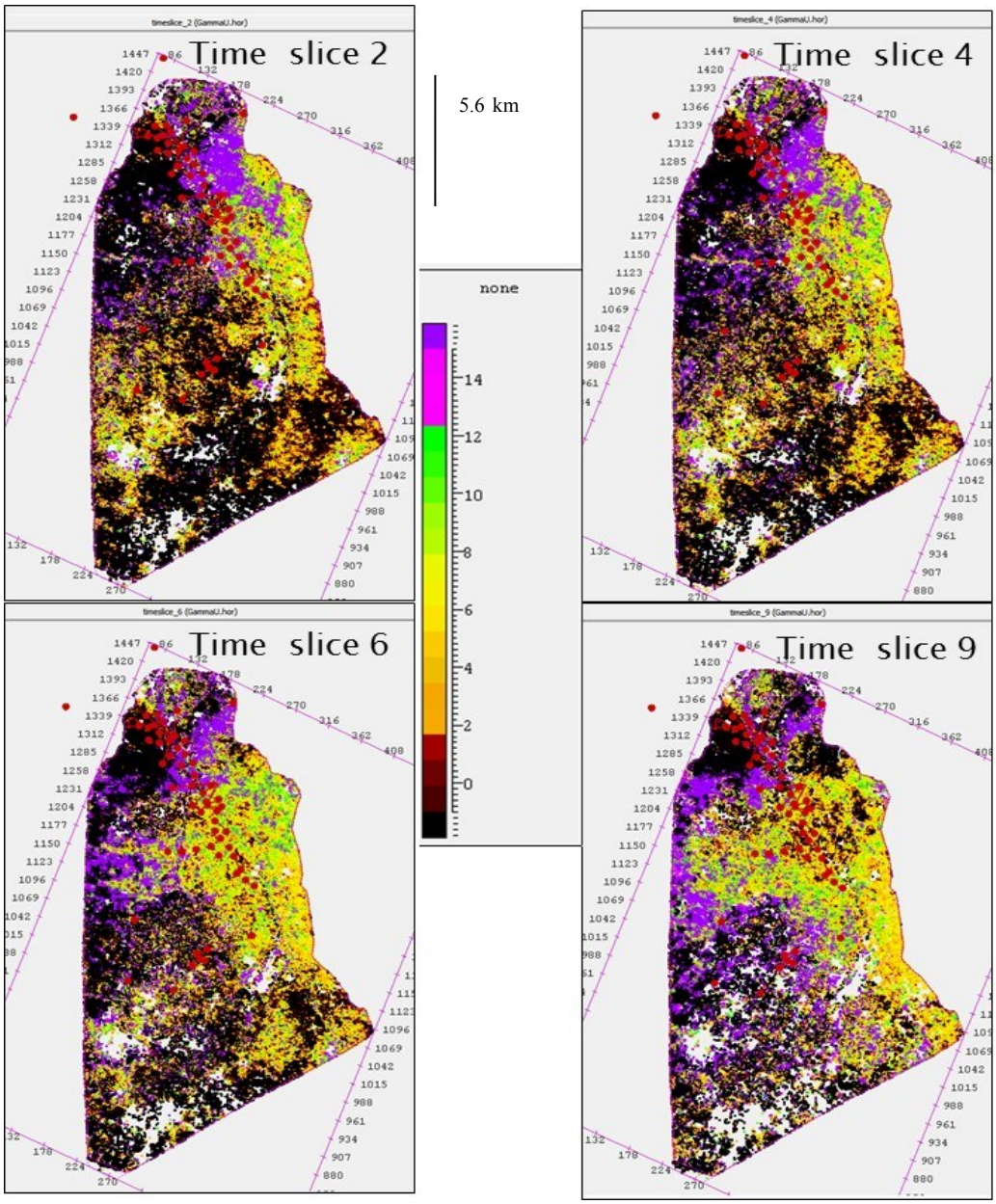

Figure 67. Time slices extracted from γk volume. The slices 2 and 4 can be inferred as part of the Upper U and the 6 and 9 as part of the Main U sandstone. γk values represent facies types. See the text for explanation.

The Figure 69 shows a comparison between the sedimentological interpretations of the Upper U by Vallejo et al., 2013 and the time slice 2 from γ_k inverted volume at

Upper U depth. From this graph we could conclude that predefined Type II and Type III facies are related with shore face bars. Type III shows a lower porosity than Type II facies based on the rock physics analysis. However, Type III can be considered as part of the facies with reservoir qualities. Besides, Type IV facies can be compared with the glauconitic sandstone from the sedimentological interpretation. As it was found by the rock physics analysis, the Type IV facies comprise sandstone with many inclusions not only glauconite but also some mud drapes and slightly calcite cement. Therefore; Type IV facies have strong marine influence. Type I facies are represent by shale facies.

Upper U sandstone correlation with sedimentological interpreted facies is not as good as Main U because Upper U sandstones intervals are thinner than minimum resolvable thickness of the seismic in some parts. Therefore, most of the P-Impedance and S-Impedance values obtained by seismic inversion are affected by resolution and probably are averaged values of thinner beds.

Productive facies can be distinguished using the cross plot of inverted γ_k vs. porosity with pay cut off in the z axis. (Vcl <0.4, ϕ>0.08 and sw<0.45). Figure 70 shows the cross plot for well log values and for pseudo logs extracted from the inversion results. The resolution of the pseudo logs is the same as seismic data consequently lower than the real well logs resolution. However, in both graphs the reservoir facies are grouped in a specific zone. In well logs the porosity of facies seems to be higher than inverted porosity.

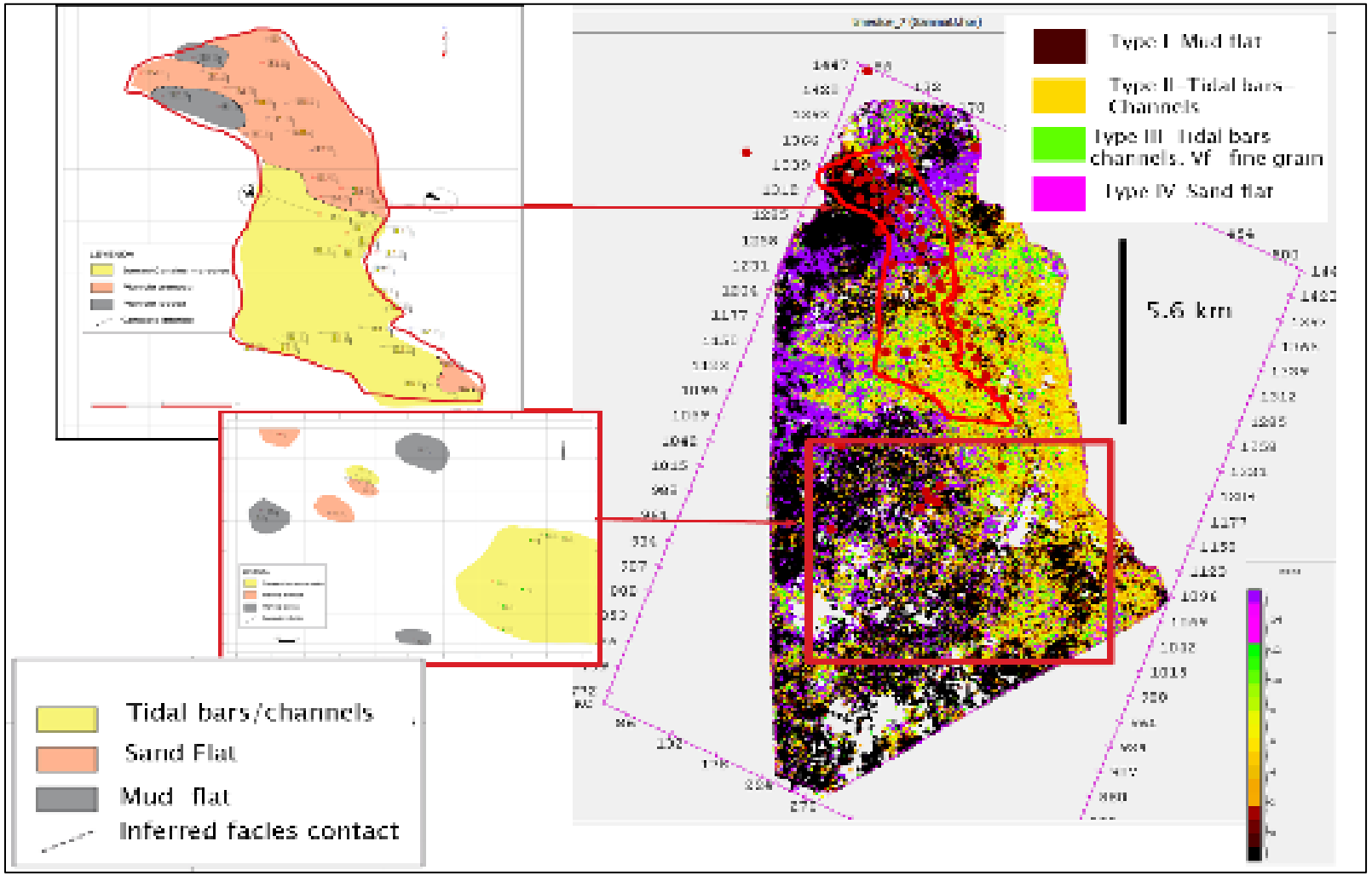

Figure 68. Time slice 7 extracted from γk volume for Main U sandstone showing inverted facies and the sedimentological interpretation by Vallejo et al, 2013

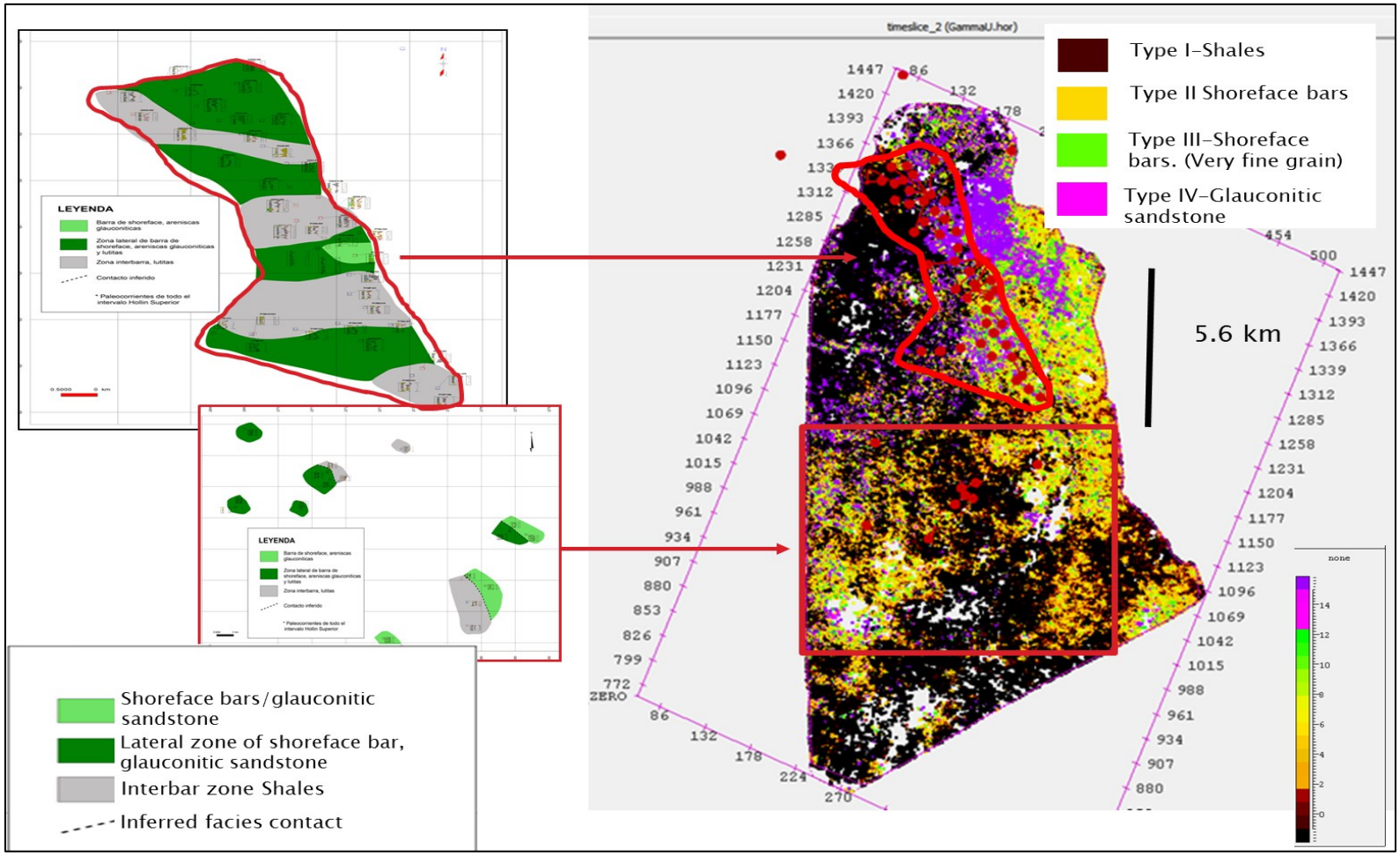

Figure 69. Time slice 3 extracted from γk volume for Upper U sandstone showing inverted facies and the sedimentological interpretation by Vallejo et al, 2013

A new porosity and γk volume restricted exclusively to the interval with values of γk from 3 to 13 and porosity values higher than 7 % is created by the polygon discrimination in Figure 70. Finally, figure 71 shows two time slices extracted from the new porosity and γk volume for netpay facies.

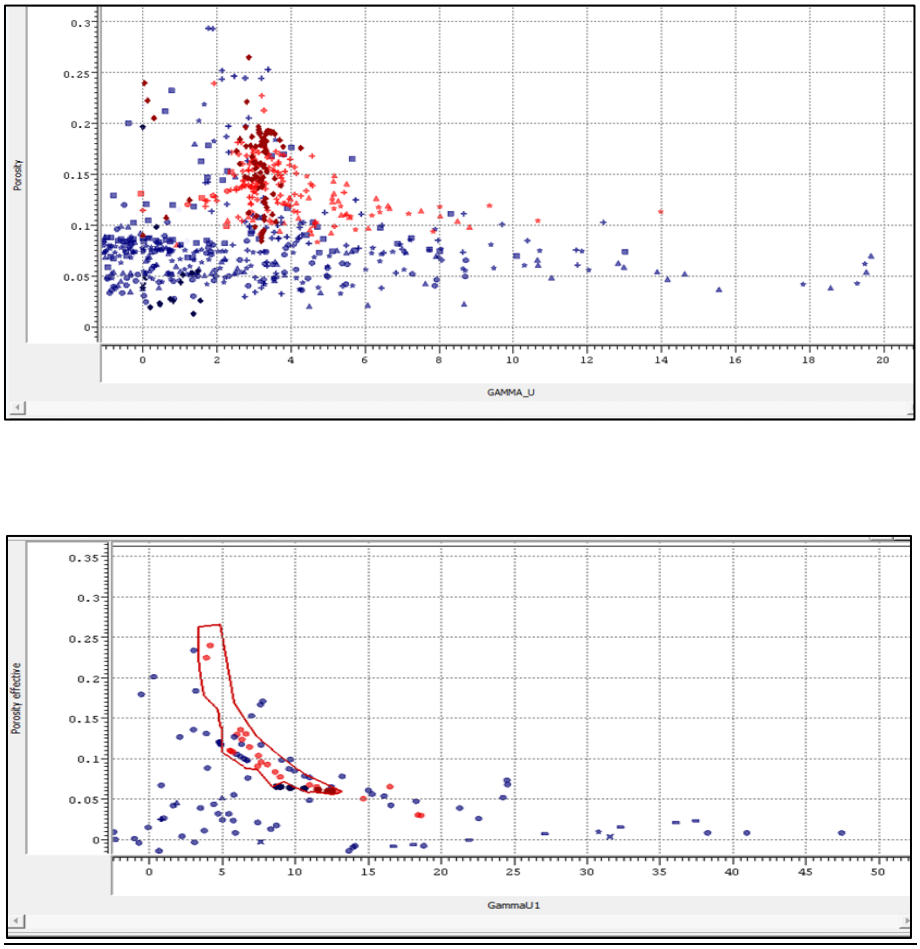

Figure 70. Cross plot of Inverted Porosity vs. γk with pay discriminator in z axis for U sandstone. Red points are net pay facies.

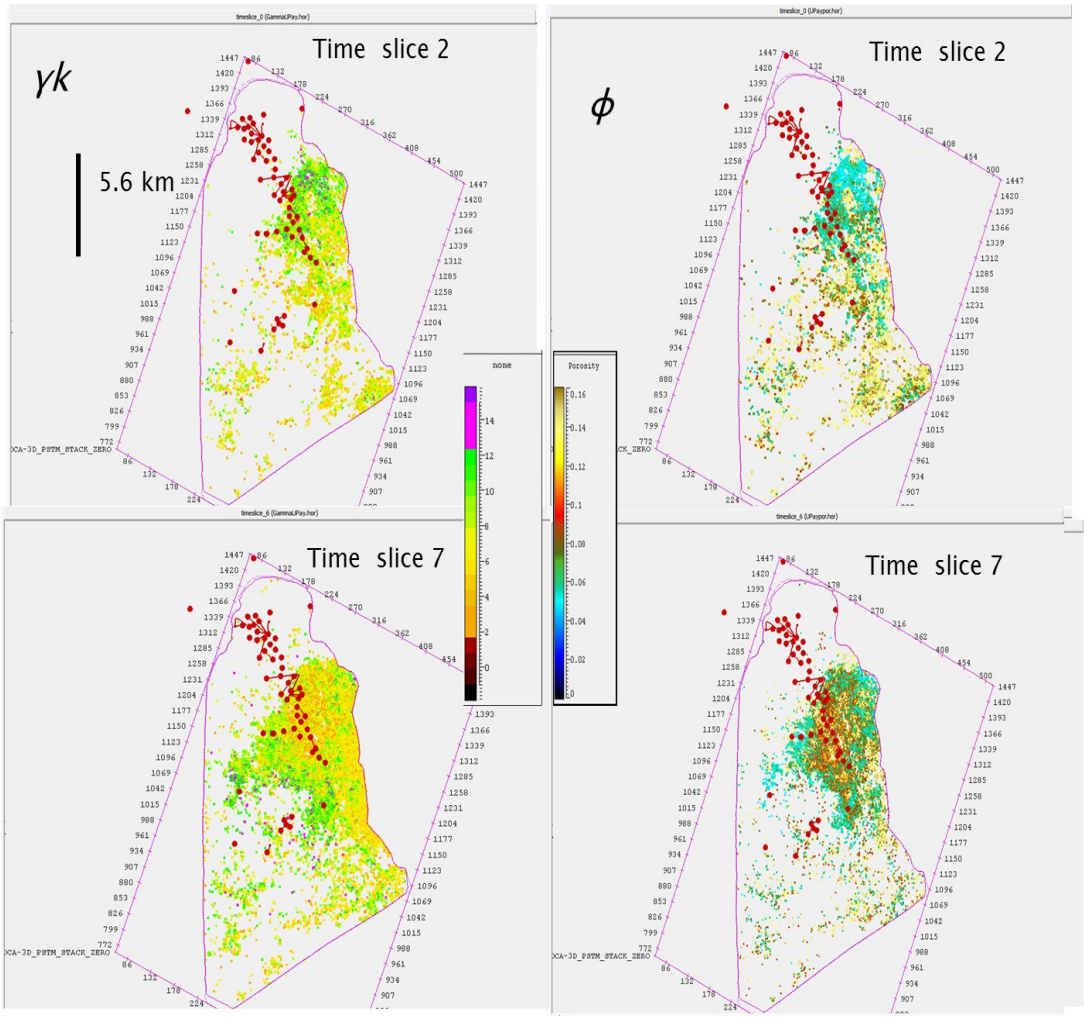

Figure 71. Time slices extracted from γk and ϕ net pay volume. The slices 4 and 7 can be inferred as part of the Upper U and Main U sandstone respectively. γk values represent facies types. See the text for explanation.

In order to set new prospective zones it is necessary to use all the available information that includes the structural and thickness maps. U top horizon determines the structural shape of the U sandstone. The area of study is crossed by a reverse fault that divides part of the oilfield in two blocks. In the south the N-S trend fault created structural trap that affect all the Cretaceous reservoirs (Figure 72). On the other hand, in

the north this fault does not cause any displacement of the blocks as it was considered before the 3D seismic data was acquired. Three wells are proposed based on the structure, thickness of the sandstone and facies classification. Without facies classification it can be possible to propose zones where structure is high, the thickness is fair but the quality of the facies is poor. In the same figure a well tie cross section with the proposed wells W-1, W-2 and W-3 is created. This cross-section is showing the inverted porosity which is high to fair in the chosen zones for the new wells. Other zones present good prospectively based on the confidence that facies and inverted porosity promote

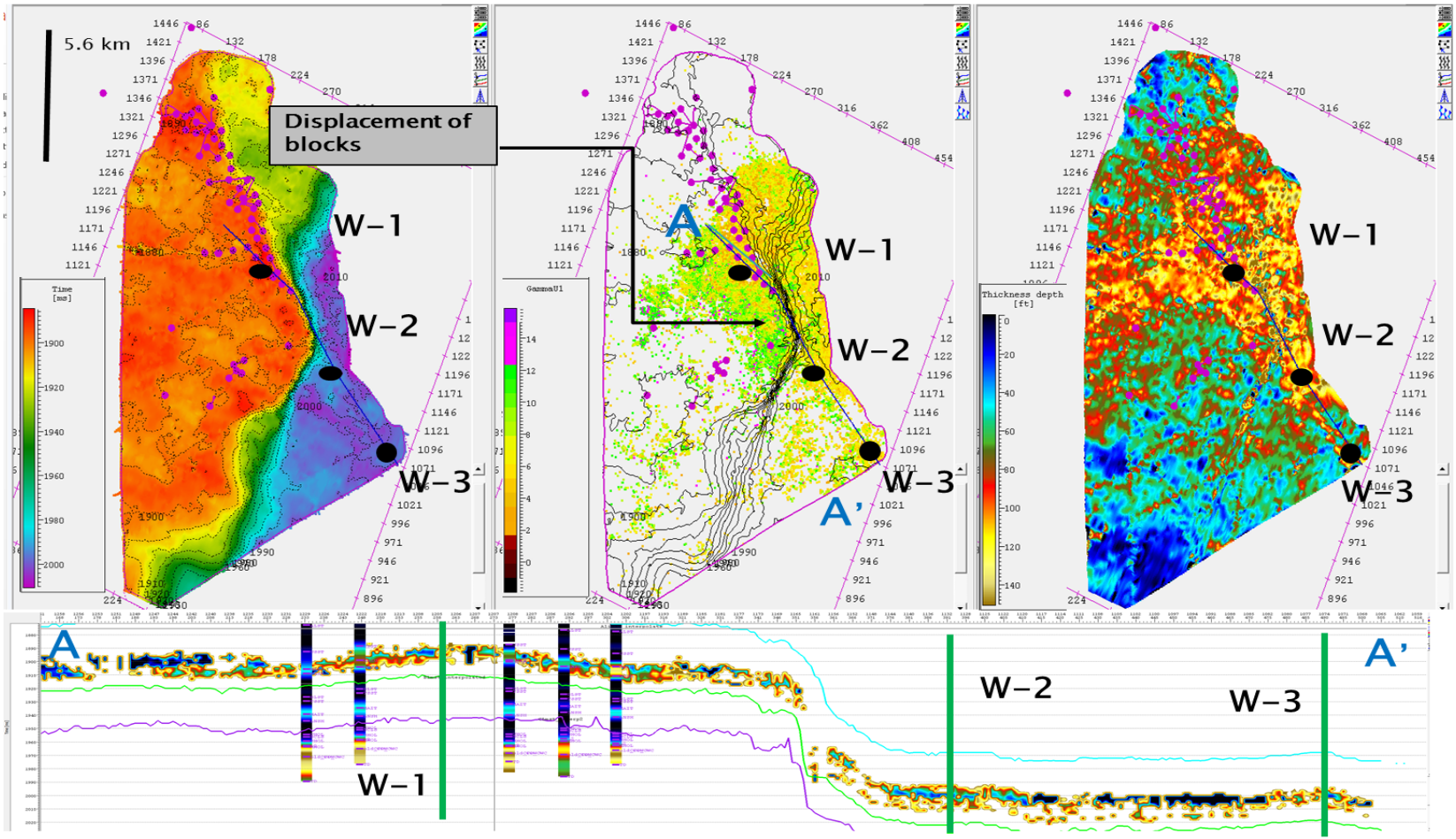

Figure 72. From left to right: Structural map at the top of U sandstone, γk time slices showing tidal bars and tidal shoreface facies with structural contours and thickness map of U sandstone. In the lower part, a cross section with inverted porosity and new prospective zones

6. CONCLUSIONS

Rock physics analysis has proved to be a powerful tool to classified facies for Hollin and U sandstones since it helps to understand similar seismic response of different facies. Without the rock physics analysis a misinterpretation of the seismic response can be performed and increment of the exploration risk will be increased.

Sun 2000' model has been developed in order to understand the influence of different factors in the seismic response taking into account that one of the most influential parameters is the pore structure. This is intimately related to the depositional process and diagenesis in sedimentary rocks. In Hollin and U sandstone pore structure has been proved to be related to grain size and sorting and inclusions. Presence of mud drapes and calcite cement affects in a severe way the seismic response in Upper Hollin. Glauconite presence affects the seismic response of Upper U sandstone.

The compressional and shear frame flexibility factor were extracted from the available S-sonic and P-sonic well logs. Then, the ratio (*c* ratio) of compressional and shear frame flexibility factors was calculated. For clean sandstones with content of clay less than 40% the *c* ratio is constant confirming the homogeneity in the pore structure. Facies with a content of clay higher that 40% show strong variation in the values of *c* ratio. Clay cut off value of 40% is important to determine the change in seismic response from clean sandstones and shaly facies. In Main Hollin and Main U sandstones, transformation of feldspar in kaolinite is the main diagenetical process that affects the

pore structure and pore connectivity while in Upper Hollin and in Upper U it is the glauconite presence.

The mineralogical composition of solid frame of the rocks was divided in quartz and non-quartz minerals. Non-quartz mineral comprises kaolinite and K-feldspar for Main Hollin and for Main U sandstones, and it comprises glauconite, kaolinite and K-feldspar for Upper U and Upper Hollin sandstones. For Main Hollin and Main U, the solid frame values of K and μ for the non-quartz facies were the average of K-feldspar and kaolinite values. This assumption is acceptable since the closed value between these parameters for K-feldspar and kaolinite. For Upper U, the values for K_{clay} and μ_{clay} for non-quartz mineral fraction were taken directly from the measurement of the well log in the highest clay content zones. Other minerals like pyrite are present in an average percentage of 2 % especially in zone with a strong marine depositional environment influence. Besides, other minerals that are in low and non-continuous concentrations have not been taken into account to develop the mineralogical fraction used in the rock physics analysis. The average between Voigt, 1910 and Reuss,1929' bounds were used for the calculus of bulk and shear modulus of the solid frame with all of the assumptions mentioned before.

In Hollin sandstone, facies with γ_k values between 2 and 6 are most the prolific facies with a low content of clay, medium to coarse grain size , moderately to well sorted sandstone. This facies can be correlated with the fluvial channel facies defined by Vallejo, et al., 2013. In order to distinguish facies in Hollin sandstone in a successful manner, the use of γ_k and porosity is mandatory as it is shown in Figure 25.

For U reservoir γ_k values allow to classify the facies in four types. Type I presents values of γ_k lower than 2. Shale and very shaly sandstone with a very fine grain size are enclosed in this interval. Type II, which values of γ_k are between 2 and 6, are the most prolific facies with a fine to medium grain size and well sorted with no inclusions. These values can be considered representative of the productive facies for Main U sandstone. Type II is characterized by facies with a γ_k value between 6 and 8. They have a fine to very fine grain size and well sorting. Sandstones with very fine to fine grain size with mud drapes and in some cases and slighly carbonate cement are the facies represented by values of γ_k higher than 8, (Type IV). Based on this approach, it is possible to create a facies discriminator from well logs that can be used not only for inversion but also for geo modelling and posterior reservoir simulation.

Analysis of seismic data shows that there are some acquisition problems. Prominent variation of phase and reduction of frequency are common in some parts of the survey. This fact causes that different wavelets were extracted from different zones during the well-seismic tie and wavelet extraction.

In order to determine the optimum number of stacks to be used in the inversion, AVO analyses using reflectivity extracted from well logs was performed with the Zeoprittz equations for the different angle ranges From this analysis, it was concluded that a moderate advantage is achieved in the characterization of the reflectivity using four angle-gather stack; however, the quality of the 20-30 ° angle-gather stack is not as good as the quality of the 4-14 and 12-22 ° angle gathers stacks. Adding the 30-40 °

angle gather stack to the inversion gives the best results in the characterization of S – Impedance.

In Main Hollin sandstone, facies are more homogeneous and the productivity of this reservoir is related to the location of the water oil contact and high structures. After rock physics analysis, it was concluded that variation in fluid do not cause any different seismic response in Hollin sandstone. On the other hand, U sandstone presents a strong areal variability of the facies and, also, its productivity is more related to the localization of the good quality facies. Based on these considerations, and also in the fact that quality of the seismic data is deteriorated with depth, the seismic inversion was performed for U sandstone only since the results was more transcendent.

Inversion of porosity and γ_k is performed using Sun 2000' model assuming that U sandstone has a constant *c* ratio. Results from the application of Sun 2000' model to the seismic inversion product show a strong consistency after applying quality control methodology. Pseudo logs extracted from inverted porosity are highly correlated with the porosity logs obtained from petro physical analysis. Also, the γ_k values obtained represent facies in similar way as it was determined by the rock physics analysis using well logs. Type I facies are represented by zones that shows values of γ_k lower than 2. Type II facies are related with values of γ_k between 2 and 8. Type III facies present values of γ_k between 8 and 12.

The areal extension of the different facies correlates with the sedimentological interpretation performed by Vallejo, et al., 2013 based on core description. Type I facies are related with mud flat facies in Main U and to shales in Upper U, Type II facies

correspond to fine to medium grain size sandstone deposited as tidal bars for Main U sandstone and shore face bars in Upper U sandstone. Type III facies also can be correlated with tidal bars and shoreface bars in Main U and Upper U sandstones respectively. Most of the good quality reservoir facies are enclosed in Type II and Type III. Finally, Type IV facies have the same characteristics as the sand flat facies defined by Vallejo, et al., 2013 for Main U sandstone and low porosity and low permeability glauconitic sandstone for Upper U sandstone.

Facies distribution from the presented methodology highly improves the definition of prospective zones. Three new wells are proposed based on the structure, sand thickness and facies distribution. W-1 is located in zone of proved reserves; W-2 and W-3 are located in a zone of possible reserves. Based on the achieved results, new prospective zones can be visualized at the east flank of the fault because good quality facies are extended to that zone and also because the main fault does not produce any displacement of the blocks at the north of the oilfield. This structural continuity can allow free fluid migration.

It can be concluded that with this methodology, reservoir characterization and exploration of relatively new zones will have a higher success. However, to apply this workflow, it is crucial the acquisition of geological and petro physical data such as conventional cores analysis, thin sections, Spectral Gamma Ray logs , Dipolar sonic logs, and VSPs.

REFERENCES

Adesokan, H and F. Sun., 2010, Rock-physics-based estimation of critical volume of shale and its effect on seismic and petrophysical properties: a North-Sea example, SEG Denver annual meeting.

Aki, K. and P.G. Richards, 1980, Quantitative seismology: Theory and method: W. H. Freeman and Co.

Alvarado, G. and M. Santos, 1989, Consideraciones petrográficas de la formación Hollin. Unpublished report for CEPE.

American Petroleum Institute, 1998, Recommended practices for core analysis, exploration and production department: API Publishing Services.

Avseth, P., T. Mukerji, G. Mavko, 2013, Quantitative seismic interpretation, applying rock physics tools to reduce interpretation risk: Cambridge University Press

Baby, P., M. Rivadeneira and R. Barragan, 2004. La Cuenca Oriente: geología y petróleo, (Oriente Basin: geology and petroleum). lFEA- Institut de Recherche pour le Développement (lRD) and Petroecuador.

Bardon, C., and B. Pied,1969. Formation water saturation in shaly sands: Society of Professional Well Log Analysts10th Annual Logging Symposium Transactions: Paper Z,19 pp.

Barragan, R ., F. Christophoul, H. White, P. Baby and M. Rivadeneira, et al., 2004, Estratigrafía secuencial del Cretácico de la Cuenca Oriente del Ecuador in La Cuenca Oriente: geología y petroleo,(Oriente Basin: geology and petroleum): lFEA-Institut de Recherche pour le Développement (lRD) and Petroecuador, 45-68

Biot, M.A., 1956, Theory of propagation of elastic waves in a fluid saturated porous solid. Parts I and II. Low frequency range and II. Higher-frequency range. J. Acoust. Soc. Am., **28**, 168–191.

Christophoul, F., 1999, Discrimination des influences tectoniques et eustatiques dans les bassins liés a des zones de convergence: exemples du bassin subandin d'Equateur: Doctor of Philosophy theses, Université Toulouse IlI. Paul Sabatier.

Clavier, C., G. Coates and , J. Dumanoir, 1977, The theoretical and experimental bases for the Dual Water model for the interpretation of shaly Sands, paper SPE 6859 presented at the 1977 SPE Annual Technical Conference and Exhibition, Denver.

Dalrymple, R. W., B. A. Zaitlin, and R. Boyd, 1992. Estuarine facies models: conceptual basis and stratigraphic implications: Journal of Sedimentary Petrology, **62** : 1130–1146.

Dashwood, M., and , I. Abbots, 1990. Aspects of the petroleum geology of the Oriente Basin, Ecuador: Classic Petroleum Provinces, Geological Society Special Publication, **50**, 89-117.

Diaz, E., M. Prasa, M.A. Gutierrez, J. Dvorki, G. Mavko,2002, Effect of glauconite on the elastic properties, porosity, and permeability of the reservoirs rocks: AAPG Annual Meeting 2002 AAPG Search and Discovery Article#90007

Gardner, G.H.F, L.W. Gardner and A. R. Gregory, 1974, Formation velocity and density: the diagnostic basics for stratigraphic traps: Geophysics , **39**, 770-780

Gassmann, F., 1951, Elasticity of porous media. Vierteljahrsschrder Naturforschenden Gesselschaft, **96**: 1-23.

Geertsma, J. and D.C. Smit, 1961,Some aspects of elastic wave propagation in fluid-saturated porous solids: Geophysics, **26**, 169–181.

Halliburton, 2013, Pore throat size distribution / X-ray diffraction for mineralogy: Unpublished report for PETROAMAZONAS EP

Jaillard, E., 1997, Síntesis estratigráfica y sedimentológica del Cretáceo y Paleógeno de la Cuenca Oriental del Ecuador Petroproduccion-Orstom.

Jones, M., 1993, Mineral analysis by x-ray fraction diffraction (XRD) for Upper Hollin: Unpublished Report from Core Laboratories to Oryx Energy.

Massaferro, J.L., G.P. Eberli, G. Baechle, R. Weger and Y.E. Sun, 2004, Effects of pore types on velocity and permeability in carbonate rocks. Applications of Sun model to core-log-seismic inversion: Final game changer report, Shell International Exploration and Production.

Mavko, G., T. Mukerji, and J. Dvorkin, 2003, Rock physics handbook. Cambridge University Press.

Minear, J. W., 1982, Clay models and acoustic velocities: Presented at the SPE Annual. Technical Conference and Exhibition, Society of Petroleum Engineers of AIME.

Oldenburg, D.W., T. Scheuer, and S.Levy, 1983, Recovery of the acoustic impedance from reflection seismograms: Geophysics, **48**, 1318-38.

Petroproduccion, 1994, Estudio geológico núcleo central de corona zona arenisca U del pozo P-15, Arenisca U: Unpublished report, Centro de Investigaciones Geológicas-Quito

Poupon, A., and J, Levaux, 1971, Evaluation of water saturation in shaly formations: Society of Professional Well Log Analysts 12th Annual Logging Symposium Transactions.

Raymer, L.L., E.R.,Hunt, and J.S. Gardner,1980, An improved sonic transit time-to-porosity transform: Trans. Soc. Prof. Well Log Analysts, 21st Annual Logging Symposium.

Reuss, A., 1929, Berechung der fliessgrenze vonmischkristallen. Z. Angew: Math. Mech, **9**, 55-58

Romeuf, N., L. Aguirre, P. Soler, G. Feraud, E. Jaillard, and G.Ruffet 1995, Middle Jurassic volcanism in the northern and central Andes: Revista Geológica de Chile, Vol. **22**(2): 245-259.

Romeuf, N., P. Munch, , P. Soler, E. Jaillard, R, Pik. and L.Aguirre, 1997, Mise en évidence de 2 lignées magmatiques dans le volcanisme du Jurassique inférieur de la zone Subandine Equatorienne: Compte Rendus 1'Académie des Sciences, Paris, **324**(36): 1-368.

Russel, BH,. 1988, Introduction to seismic inversion methods: SEG Course Notes No 2

Vallejo, C. and J.Gaibor, 2013, Modelo sedimentologico y estratigrafico del bloque 7: Halliburton.

Sun, Y.F., 1994, On the foundations of the dynamical theory of fractured porous media and the gravity variations caused by dilatancies: Columbia Univ., Ph.D. dissertation.

Sun, Y.F., and D. Goldberg, 1997, Effects of aspect ratio changes on wave velocities in fractured rocks: SEG Expanded Abstract*,* **67**, 925-928.

Sun, Y. F., 2000, Core-log-seismic integration in hemipelagic marine sediments on the eastern flank of the Juan De Fuca Ridge: ODP Scientific Results, **168**, 21-35.

Sun, Y.E, J.L. Massaferro, G. Eberli, and Y.C.Teng, 2002, Quantifying the effects of pore structure and fluid saturation on acoustic wave velocity in carbonates, in Shang, E.-C., Li, Qihu, and T.F. Gao, Eds., Theoretical and Computational Acoustics 2001: World Scientific Publishing Co., 335-347.

Sun, Y.F., 2004, Seismic signatures of rock pore structure: Applied Geophysics, **1**, 42-49.

Voigt, W., 1910, Lehrbuch der kristallphysik: Teubner: Leipzig.

White, H. J, 1993, Core description C-9: Unpublished report for Oryx Energy.

Wyllie, M. R. J., , A.R. Gregory, and L.W.Gardner, 1956. Elastic wave velocities in heterogeneous and porous media: Geophysics, **21**(1), 41–70.

Xu, S. and , R.E. White, 1995, A new velocity model for clay–sand mixtures: Geophys. Prospect, **43**, 91–118.

Zoeppritz, K., 1919, Erdbebenwellen VIIIB: On the reflection and propagation of seismic waves: Go¨ttinger Nachr, **I**, 66–84.